

ANTIPARTICLE TO PARTICLE RATIOS IN AU+AU AND CU+CU  
COLLISIONS AT THE RELATIVISTIC HEAVY ION COLLIDER

BY

VASUNDHARA R CHETLURU  
Masters in Physics  
University of Hyderabad, 2002

THESIS

Submitted in partial fulfillment of the requirements  
for the degree of Doctor of Philosophy in Physics  
in the Graduate College of the  
University of Illinois at Chicago, 2008

Chicago, Illinois

Copyright by  
Vasundhara R Chetluru  
2008

To the void

and thoughts that color the void

To the space and time

their mysterious relationship of likeness and unlikeness

## ACKNOWLEDGMENTS

## PREFACE

## TABLE OF CONTENTS

<u>CHAPTER</u>	<u>PAGE</u>
<b>1 SUMMARY . . . . .</b>	<b>1</b>
<b>2 INTRODUCTION . . . . .</b>	<b>2</b>
<b>3 THE PHOBOS EXPERIMENT . . . . .</b>	<b>16</b>
3.1 Relativistic Heavy Ion Collider . . . . .	16
3.2 PHOBOS Experimental Setup . . . . .	22
3.2.1 Silicon spectrometer . . . . .	26
3.3 Data acquisition . . . . .	28
3.4 Hardware trigger setup . . . . .	30
3.5 Online and off-line calibration of the signals . . . . .	37
3.6 Vertex reconstruction . . . . .	37
3.7 Centrality and Event Selection . . . . .	44
<b>4 OVERVIEW OF THE ANALYSIS . . . . .</b>	<b>47</b>
<b>5 DATA QUALITY STUDIES . . . . .</b>	<b>58</b>
5.1 Beam-orbit Studies . . . . .	59
5.2 Run average data quality studies . . . . .	69
<b>6 PARTICLE IDENTIFICATION AND RAW RATIOS . . . . .</b>	<b>88</b>
6.1 Particle Identification . . . . .	88
6.2 Raw ratios . . . . .	101
<b>7 CORRECTIONS . . . . .</b>	<b>112</b>
7.1 Absorption correction . . . . .	113
7.2 Secondary correction . . . . .	118
7.3 Feed-down correction . . . . .	119
<b>8 SYSTEMATIC STUDIES . . . . .</b>	<b>127</b>
<b>9 RESULTS AND INTERPRETATION . . . . .</b>	<b>137</b>
9.1 Results . . . . .	137
9.2 Interpretation . . . . .	146
9.2.1 Observation . . . . .	146
9.2.2 Discussion . . . . .	154
9.3 Conclusion . . . . .	157

## TABLE OF CONTENTS (Continued)

<u>CHAPTER</u>	<u>PAGE</u>
APPENDICES . . . . .	159
10 PHOBOS COLLABORATION . . . . .	160
11 DEFINITIONS . . . . .	161
12 DATA TAGS . . . . .	162
12.1 Centrality selection . . . . .	162
13 PARTICLE IDENTIFICATION AND RAW RATIOS - ADDI- TIONAL PLOTS . . . . .	164
14 SYSTEMATIC ERROR STUDY - ADDITIONAL PLOTS . . .	184
CITED LITERATURE . . . . .	185
VITA . . . . .	188

## LIST OF TABLES

<u>TABLE</u>		<u>PAGE</u>
I	Following table gives the summary of different collision species and collision energy as a function of year. . . . .	20
II	Following table gives the summary of all the data recorded on to the tape in millions of events units for different collision species and collision center of mass energy. . . . .	29
III	Cu+Cu 200 GeV trigger bits . . . . .	35
IV	Cu+Cu 200 GeV trigger bits . . . . .	36
V	RECONSTRUCTED VERTEX RESOLUTION . . . . .	43
VI	CENTRALITY CROSS-SECTION AND PARTICIPANTS . . . . .	45
VII	Given in the table is the summary of the beam-orbit study. Each sub-table corresponds to a combination of different energy and species. Each row in the sub-table corresponds to different beam-orbit region represented by the name and the run-range in the first column. Each entry corresponds to the mean $\pm$ rms of beam-orbit for that given run-range. Beam-orbit values for x and y and different polarities are given in different columns. . . . .	68
VIII	Comparison of average momentum . . . . .	80
IX	DEVIANT RUN SUMMARY TABLE . . . . .	86
X	Total number of events in different polarities used to obtain the final ratios. . . . .	103
XI	HYPERON SUMMARY TABLE . . . . .	122
XII	SUMMARY OF SYSTEMATIC STUDIES . . . . .	130
XIII	SUMMARY OF TRACK FIT PROBABILITY . . . . .	133
XIV	RATIOS VS $P_T$ . . . . .	143



## LIST OF TABLES (Continued)

<u>TABLE</u>		<u>PAGE</u>
XV	CU+CU 200 GEV AND 62.4 GEV RATIOS AS A FUNCTION OF CENTRALITY . . . . .	144
XVI	AU+AU 200 GEV AND 62.4 GEV RATIOS AS A FUNCTION OF CENTRALITY . . . . .	145
XVII	SUMMARY OF FITS TO THE RATIOS AS FUNCTION OF CENTRALITY . . . . .	146
XVIII	SUMMARY OF MEASURED CHEMICAL POTENTIAL . . . . .	156

## LIST OF FIGURES

<u>FIGURE</u>		<u>PAGE</u>
1	Summary of strong coupling constant measurement from various experiments. . . . .	4
2	Schematic view of the QCD phase diagram. . . . .	6
3	Pseudorapidity distribution in PHOBOS . . . . .	8
4	Pseudorapidity distribution in PHOBOS . . . . .	10
5	Elliptic flow in PHOBOS as a function of centrality . . . . .	11
6	Schematic diagram of the Relativistic Heavy Ion Collider. . . . .	18
7	PHOBOS detector with its sub-systems. . . . .	24
8	PHOBOS detector with its sub-systems. . . . .	25
9	. . . . .	33
10	Cu+Cu 200 GeV L1 trigger efficiency as function of sum of the signals in both the paddles. . . . .	34
11	The vertex algorithm using the vertex detector for a typical DATA event. The top histogram is the Probability Histogram, which is used to determine the search range in the Position Histogram (the smaller histogram). The peak in the Position Histogram corresponds to the found vertex, the arrow indicates the typical peak-search range in the Position Histogram.	38
12	Examples of hits from primary particles leaving signals in one (left) or three (right) active elements of the silicon detector and the ranges of possible vertex positions, $\delta z$ , defined by simple geometrical calculations.	42
13	The error of the reconstructed vertex position, $\sigma(Z_{oct} - Z_v)$ , as a function of the number of charged primary particles registered in the octagon, $N_{oct}$ , for Au+Au and Cu+Cu collisions at $\sqrt{s_{NN}} = 200$ GeV. . . . .	43
14	. . . . .	50

## LIST OF FIGURES (Continued)

<b><u>FIGURE</u></b>	<b><u>PAGE</u></b>
15 . . . . .	50
16 . . . . .	52
17 Flow diagram . . . . .	57
18 Beam-orbit $\langle x \rangle$ and $\langle y \rangle$ as a function of run number for Cu+Cu 200 GeV data. The three highlighted regions A, B and C represent steady beam-orbit regions. . . . .	60
19 Detailed study of beam-orbit distribution for region - A (as shown in Figure 18) for 200 GeV Cu+Cu data. Right Panel is the $\langle x \rangle$ distri- bution for different polarities. Left Panel is the $\langle y \rangle$ distribution for different polarities. . . . .	61
20 Beam-orbit $\langle x \rangle$ and $\langle y \rangle$ as a function of run number for Cu+Cu 62 GeV data. The highlighted region A is the only steady beam-orbit region for this data set. . . . .	62
21 Detailed study of beam-orbit distribution for region - A (as shown in Figure 20). Right Panel is the $\langle x \rangle$ distribution for different polarities for Cu+Cu 62.4 GeV data. Left Panel is the $\langle y \rangle$ distribution for different polarities. . . . .	63
22 Beam-orbit $\langle x \rangle$ and $\langle y \rangle$ as a function of run number for Au+Au 200 GeV data. The three highlighted regions A, B and C represent steady beam-orbit regions. . . . .	64
23 Detailed study of beam-orbit distribution for region - B (as shown in Figure 22). Right Panel is the $\langle x \rangle$ distribution for different polarities for Au+Au 200 GeV data. Left Panel is the $\langle y \rangle$ distribution for different polarities. . . . .	65
24 Beam-orbit $\langle x \rangle$ and $\langle y \rangle$ as a function of run number for Au+Au 62 GeV data. The three highlighted regions A is the only steady beam-orbit region for this data set. . . . .	66
25 Detailed study of beam-orbit distribution for region - A (as shown in Figure 24) for Au+Au 62.4 GeV data. Right Panel is the $\langle x \rangle$ distri- bution for different polarities. Left Panel is the $\langle y \rangle$ distribution for different polarities. . . . .	67

## LIST OF FIGURES (Continued)

<b><u>FIGURE</u></b>		<b><u>PAGE</u></b>
26	Avg # of tracks as function of beam-orbit Y in Au+Au 200 GeV . . . .	73
27	Avg # of tracks in Cu+Cu 200 GeV . . . . .	73
28	Avg # of tracks in Cu+Cu 62 GeV . . . . .	74
29	Avg # of tracks in Au+Au 200 GeV . . . . .	74
30	Average number of tracks per event in Au+Au 62.4 GeV data. Blue corresponds to arm -1 and orange corresponds to arm -2. . . . .	75
31	Average track momentum per event in Cu+Cu 200 GeV data. Blue corresponds to arm -1 and orange corresponds to arm -2. . . . .	77
32	Average track momentum per event in Cu+Cu 62.4 GeV data. Blue corresponds to arm -1 and orange corresponds to arm -2. . . . .	78
33	Average track momentum per event in Au+Au 200 GeV data. Blue corresponds to arm -1 and orange corresponds to arm -2. . . . .	79
34	Average track momentum per event in Au+Au 62.4 GeV data. Blue corresponds to arm -1 and orange corresponds to arm -2. . . . .	79
35	Average track distance of closest approach per event in Cu+Cu 200 GeV data. Blue corresponds to arm -1 and orange corresponds to arm -2. .	82
36	Average track distance of closest approach per event in Cu+Cu 62.4 GeV data. Blue corresponds to arm -1 and orange corresponds to arm -2. . . . .	82
37	Average track distance of closest approach per event in Au+Au 200 GeV data. Blue corresponds to arm -1 and orange corresponds to arm -2. .	83
38	Average track distance of closest approach per event in Au+Au 62.4 GeV data. Blue corresponds to arm -1 and orange corresponds to arm -2. . . . .	83
39	Average track distance of closest approach per event in Cu+Cu 200 GeV data. . . . .	84
40	Average track distance of closest approach per event in Cu+Cu 62.4 GeV data. . . . .	85

## LIST OF FIGURES (Continued)

<u>FIGURE</u>		<u>PAGE</u>
41	Average track distance of closest approach per event in Au+Au 200 GeV data. . . . .	85
42	Average track distance of closest approach per event in Au+Au 62.4 GeV data. . . . .	85
43	. . . . .	89
44	. . . . .	91
45	. . . . .	92
46	Ratio of the data and theoretical Bethe-Bloch function is given. The different panels correspond to different Bethe-Bloch predictions for different particle assumed mass as given by the name of the particle on left-hand top corner of each plot. . . . .	94
47	The mean value of the band around unity from Figure 46 , for each particle independently, is plotted in round marker as a function of transverse momentum . A sixth order polynomial fit function is presented in a line.	95
48	Ratio of the data and the product of the theoretical Bethe-Bloch function with correction function is given. The different panels correspond to different Bethe-Bloch predictions for different particle assumed mass as given by the name of the particle on left-hand top corner of each plot. .	95
49	. . . . .	96
50	Particle identification bands obtained using method-I. . . . .	96
51	. . . . .	99
52	. . . . .	99
53	. . . . .	100
54	Raw ratios for Cu+Cu 200 GeV data determined using method-II plotted as a function of centrality bin. . . . .	104
55	Raw ratios for Cu+Cu 62.4 GeV data determined using method-II plotted as a function of centrality bin. . . . .	105

## LIST OF FIGURES (Continued)

<b><u>FIGURE</u></b>		<b><u>PAGE</u></b>
56	Raw ratios for Au+Au 200 GeV data determined using method-II plotted as a function of centrality bin. . . . .	106
57	Raw ratios for Au+Au 62.4 GeV data determined using method-II plotted as a function of centrality bin. . . . .	107
58	Raw ratios for Cu+Cu 200 GeV data determined using method-II plotted as a function of centrality bin. . . . .	108
59	Raw ratios for Cu+Cu 200 GeV data determined using method-II plotted as a function of centrality bin. . . . .	109
60	Raw ratios for Au+Au 200 GeV data determined using method-II plotted as a function of centrality bin. . . . .	110
61	Raw ratios for Au+Au 200 GeV data determined using method-II plotted as a function of centrality bin. . . . .	111
62	Absorption correction to the ratio for protons as a function of transverse momentum for all four combinations of arms and bending directions represented by different panels. In each panel, triangular marker represents the correction obtained using the FLUKA hadronic interactions package and squares represent the GHEISHA hadronic interactions package. . .	114
63	The absorption correction to the ratio as a function of transverse momentum for all the three identified particles corresponding different panels. In each panel, different markers represent different combinations of arms and bending directions. . . . .	115
64	Secondary correction as function of transverse momentum obtained using Cu+Cu 200 GeV HIJING Monte-carlo data. Different panels represent different identified particles. . . . .	120
65	Ratio of acceptance of feed-down and primary protons(antiprotons) as a function of transverse momentum. . . . .	123
66	Ratio of acceptance of feed-down and primary protons(antiprotons) as a function of transverse momentum. . . . .	124

## LIST OF FIGURES (Continued)

<u>FIGURE</u>		<u>PAGE</u>
67	Study of the systematic variation of the DCA cut. Left panel, min-bias raw ratios in the bins of the DCA cut. Right panel, min-bias raw ratio as a function of applied cut. The data presented here is for pions in Cu Cu 200 GeV. . . . .	128
68	Min-bias raw ratio as a function of track fit probability variable for Cu+Cu 200 GeV data. The different panels correspond to different identified particles. . . . .	134
69	Systematic study for the different variable and final systematic error for proton ratios in Cu+Cu 200 GeV data. The study is presented in different arms and bending directions separately. . . . .	136
70	Antiparticle to particle ratios in (0-12% central) Cu+Cu collisions, as a function of the transverse momentum, for pions, kaons and protons. Open (closed) circles represent $\sqrt{s_{NN}} = 62.4$ GeV (200 GeV) data. The vertical error bars represent the ( $1\sigma$ ) statistical and the band represents systematic uncertainties. The horizontal error bars represent the bin size. . . . .	140
71	Antiparticle to particle ratios in (0-12% central) Au+Au collisions, as a function of the transverse momentum, for pions, kaons and protons. Open (closed) circles represent $\sqrt{s_{NN}} = 62.4$ GeV (200 GeV) data. The vertical error bars represent the ( $1\sigma$ ) statistical and the band represents systematic uncertainties. The horizontal error bars represent the bin size. . . . .	141
72	Antiparticle to particle ratios in Cu+Cu collisions, as a function of the number of participants, for pions, kaons and protons. The average transverse momenta of each result is $\langle p_T \rangle \approx 0.31, 0.36$ and $0.50$ GeV/c for pions, kaons and protons, respectively. Open (closed) circles represent $\sqrt{s_{NN}} = 62.4$ GeV (200 GeV) data. The vertical error bars represent the combined ( $1\sigma$ ) statistical and the band represents systematic uncertainties. The horizontal error bars represent uncertainty in determining the number of participants. . . . .	142
73	Antiparticle to particle ratios in Cu+Cu collisions, as a function of the number of collisions per participant pair, for pions, kaons and protons. Open (closed) circles represent $\sqrt{s_{NN}} = 62.4$ GeV (200 GeV) data. The vertical error bars represent the combined ( $1\sigma$ ) statistical and the band represents systematic uncertainties. . . . .	147
74	. . . . .	150

## LIST OF FIGURES (Continued)

<u>FIGURE</u>		<u>PAGE</u>
75	.....	151
76	Antiparticle to particle ratios for protons, kaons and pions in $\sqrt{s_{NN}} = 200$ GeV p+p and central Au+Au collisions from RHIC, compared to the result for central Cu+Cu collisions (bold). When available, errors are reported as statistical and systematic, respectively. Values rounded to the shown (reasonable) precision, where a zero value of the statistical uncertainty indicates the actual value is less than 0.004. The central bin for heavy ion data varies from 0-5% to 0-12%, depends on the specific experiment and data set. Lines between the columns connect the specific data points to their associated experiment. See text for more detailed discussion. ....	152
77	.....	165
78	.....	166
79	.....	167
80	.....	168
81	.....	169
82	.....	170
83	.....	171
84	.....	172
85	.....	173
86	.....	174
87	.....	175
88	.....	176
89	.....	177
90	.....	178
91	.....	179



LIST OF FIGURES (Continued)

<u>FIGURE</u>		<u>PAGE</u>
92	. . . . .	180
93	. . . . .	181
94	. . . . .	182
95	. . . . .	183
96	. . . . .	183

## LIST OF ABBREVIATIONS

AMS	American Mathematical Society
-----	-------------------------------

## SUMMARY

## CHAPTER 1

### SUMMARY

Antiparticle to particle ratios for identified protons, kaons and pions at  $\sqrt{s_{NN}} = 62.4$  and 200 GeV in Cu+Cu collisions are presented as a function of centrality and transverse momentum for the mid-rapidity region of  $0.2 < \eta < 1.4$ . For the  $\langle \bar{p} \rangle / \langle p \rangle$  ratio at  $\langle p_T \rangle \approx 0.51$  GeV/c, we observe an average value of  $0.51 \pm 0.01_{(\text{stat})} \pm 0.03_{(\text{syst})}$  and  $0.79 \pm 0.01_{(\text{stat})} \pm 0.05_{(\text{syst})}$  for the central collisions of 62.4 and 200 GeV Cu+Cu, respectively. The values for all three particle species measured at  $\sqrt{s_{NN}} = 200$  GeV are in agreement within systematic uncertainties with that seen in both heavier and lighter systems measured at the same RHIC energy. A comparison with Au+Au data, obtained using the same detector and similar analysis, is made. A systematic study indicates that the system size appears to play a weak role in determining the mid-rapidity chemical freeze-out properties affecting the antiparticle to particle ratios of the three most abundant particle species produced in these collisions.

## CHAPTER 2

### INTRODUCTION

The current (and future) heavy ion collision experiments (the Relativistic Heavy Ion Collider, the Large Hadron Collider) have a long history of motivation dating back to 1960's experiments which lead to the discovery of an abundance of new particles. Ne'eman and Gell-Mann proposed a classification of these particles based on strangeness and isospin, called the "eight fold way". This classification organized the mesons and baryons into octets. Later, the introduction of the quark with a flavor, fractional charge, spin half and baryon number boosted the predictive power of this theory. The deep inelastic scattering experiments of the electrons with the protons put forward the evidence that the electrons were being scattered by point like spin half fermions. The next challenge came with the  $\Delta^{++}(u \uparrow u \uparrow u \uparrow)$  (predicted by quark model) which violated the Pauli's exclusion principle.  $\Delta^{++}$  is symmetric under the exchange of its valance quarks, it has spin 3/2 and symmetric spatial wave function. A new property called the 'color' charge was introduced. Color has three values red, green and blue. They behave similar to the primary colors from mixing of water colors. Baryons are made of combination of all the three colors (anti-colors) and mesons are made of combinations color and anti-color, in both the cases the final particles are colorless. The  $\Delta^{++}$  in this theory would have  $\Delta^{++}(u_r \uparrow u_g \uparrow u_b \uparrow)$ , which does not violate the Pauli's exclusion principle. Initial attempts for isolating the quarks were unsuccessful.

With the introduction of the color charge, the theory of Quantum Chromo Dynamics (QCD) was introduced in early 1970's, with quarks and gluons as its degrees of freedom. Like the photons are the force carriers in quantum electrodynamics, gluons are the force carriers in QCD. Unlike the photons which do not carry electric charge, the gluons (SU(3) symmetry of the QCD Lagrangian) carry color charge. Evidence for the existence of gluons came from the three jet events in  $e^+e^-$  collisions at PETRA in 1979, where a produced  $q\bar{q}$  radiated a gluon emitting a shower of particles.

One of the main differences between Quantum Electrodynamics (QED) and QCD is in QED photons do not interact as they are charge-less. In QCD, as the gluon has a color charge they can interact with another gluon via exchange of a quark, another gluon, or direct interaction. This results in the anti-screening effect. Screening in QED decreases the effect of force field of a charged particle, if placed in a cloud of electron-positron pairs constantly being created and annihilated, on a distant distant charged particle due to polarization. A similar scenario in QCD produces quark anti-quark pairs and gluons which also carry the color charge which amplifies the effect of the color force at the distance. For a strong coupling constant ( $\alpha_s(Q^2)$ ) given by Equation 2.1,

$$\alpha_s(Q^2) = \frac{12\pi}{(33 - 2n_f) \ln(Q^2/\Lambda^2)} \quad (2.1)$$

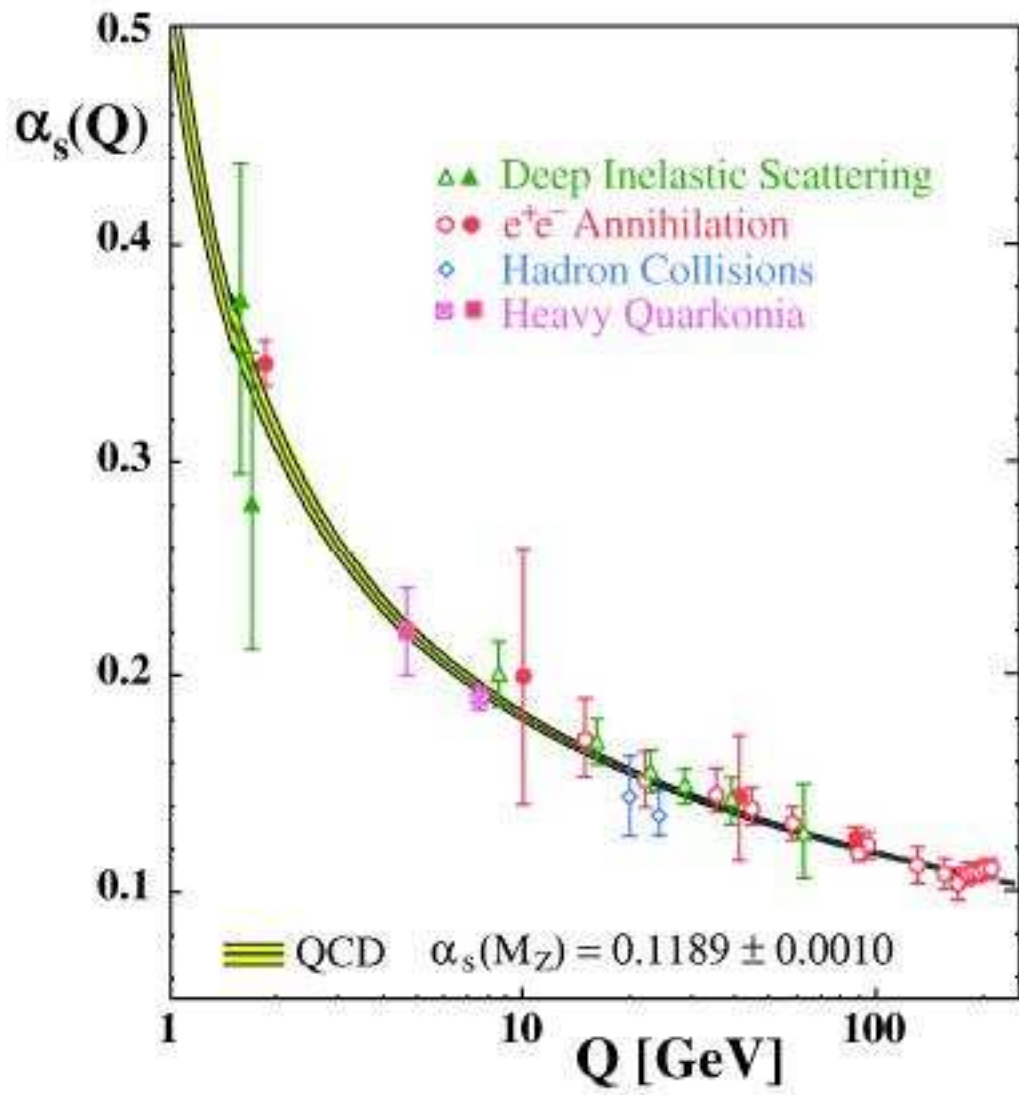


Figure 1. Summary of strong coupling constant measurement from various experiments.

$n_f$  is the number of flavors of quark,  $Q$  is the momentum transfer and  $\Lambda$  is the QCD scale factor. As shown in Figure 1, for large momentum transfers the coupling constant essentially tends to very small. The term used to describe this phenomenon is called the “asymptotic freedom”. For small momentum transfer the coupling tends to increase, which leads to the confinement of the particles. As a result of the asymptotic freedom, heating of the QCD vacuum should lead to deconfinement of the quarks and gluons. Heavy Ion Collision experiments are our attempt at trying to achieve this deconfinement and study the properties of this new phase consisting of quarks and gluon degrees of freedom.

Different phases of QCD matter are shown in Figure 2 as a function of temperature ( $T$ ) and baryo-chemical potential ( $\mu_B$ ) space. The  $\mu_B$  is related to the baryon chemical potential in stressed nuclear matter compared to the normal nuclear matter. The boundary line between the QGP and the hadron gas and its neighborhood is probed by the heavy ion collisions.

To produce heavy ion collisions and make measurement requires large scale effort and coordination, success of which is reflected through the results. A motivation which is scarcely mentioned is the “Curiosity” to expect the unexpected and understand the unknown.

### **What do we understand about collision evolution**

Heavy ions when accelerated to relativistic speeds are assumed to look like two “pancakes” colliding, due to Lorentz contraction, in the center of mass frame of reference. These pancakes collide with impact parameter (the distance between the center of the two colliding ions) ranging from zero (for head-on collisions or central collisions) to approximately twice the radius of the ions (peripheral collisions). The impact parameter, which gives a measure of the area of overlap



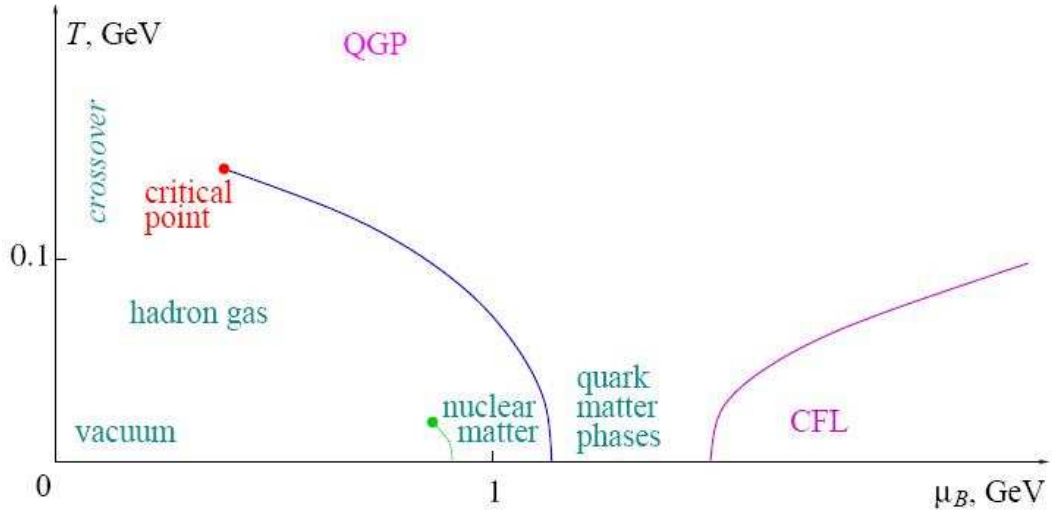


Figure 2. Schematic view of the QCD phase diagram.

between the colliding pancakes, is also popularly termed the centrality by the experimental physicists. The particles in the overlap region which take part in collisions are called the participants and the particles outside this overlap region that do not take part in hard scattering and are called the spectators (usually continue down the original path). Participants often collide with more than one nucleon, hence the total number of collisions does not scale linearly with total number of participants. An estimate of the centrality can be obtained either by measuring the total number of particle produced (centrality is directly proportional to final particle count) or by measuring the spectators (to which it is inversely proportional to).

One of the first measurements is the particle pseudorapidity density distributions. Figure 3 shows the charged particle pseudorapidity density distributions for Au+Au, Cu+Cu and d+Au

collisions from the PHOBOS experiment. An estimate of the initial energy density can be made from measurement of the bulk yields of the particles. From the Figure 3, the total particle yield as a function of colliding system and center of mass energy can be measured. For a given collision species and collision center of mass energy, the central collision produce significantly more particles than the peripheral collisions. The scaling of the number of particles produced is a combination of several factors including primarily the number of participants as well as the number of collisions. If the number of produced particles only scaled with the total number of collisions, then heavy ion collisions in general could be understand as an overlay of proton-proton events, which is not what is observed. What follows is a brief overview of the current understanding of several important features of heavy ion collisions at RHIC energies.

Collision evolution starts with a pre-equilibrium phase. A high energy density is attained during the initial collisions and a rescattering of the partons produced during the collision results in the thermal equilibrium of the system. At this point common thermodynamic properties can be used to describe the system. As the system expands, it cools and results in hadronization at transition temperatures. These formed hadrons undergo in-elastic scattering until the chemical freeze out temperature is attained. The relative yields of the primary hadrons do not change after this point. Eventually thermal freeze out sets in, there is no more elastic scattering and the transverse momentum distribution of the particles is established.

Measured charged particle momentum spectra is presented in [need reference]. As explained previously, if the heavy ion collisions simple are an overlay of binary proton-proton collisions, then by scaling the transverse momentum distributions in heavy ion with the number of binary

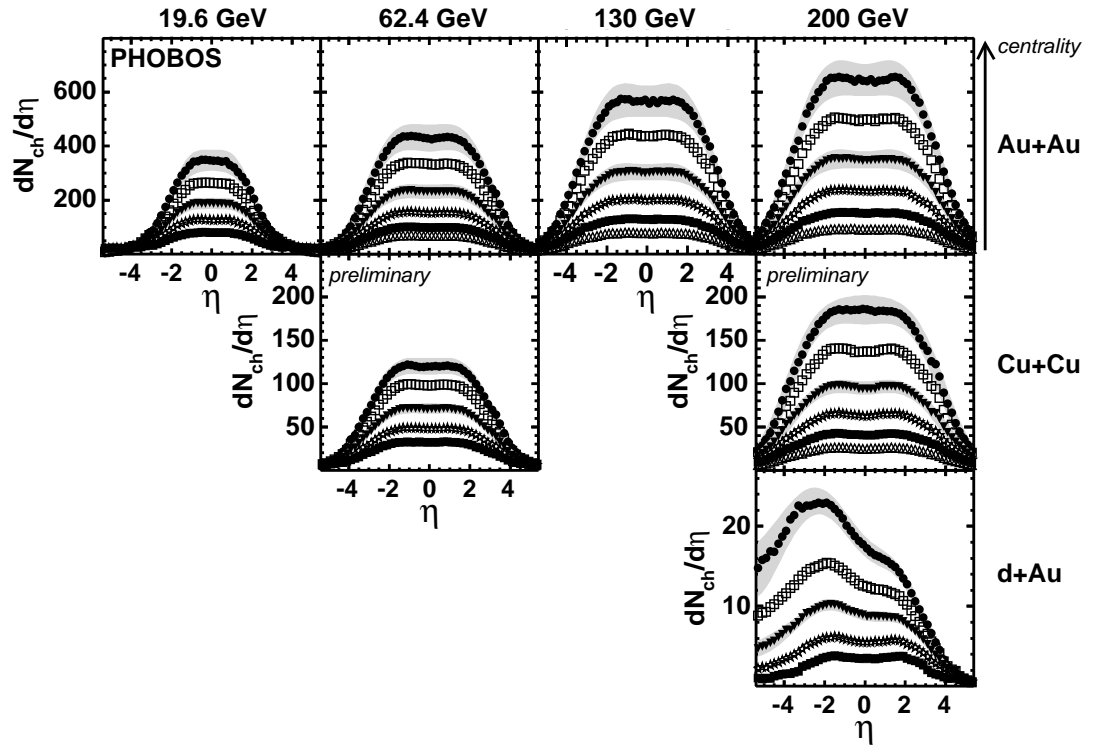


Figure 3. Charged hadron pseudorapidity distributions for different centralities for Au+Au collisions at  $\sqrt{s_{NN}} = 19.6, 62.4, 130$  and  $200$  GeV (top row from left to right), Cu+Cu at  $62.4$  and  $200$  GeV (middle row, preliminary) and d+Au at  $200$  GeV (bottom row)

collisions should produce a yield similar to that seen in proton-proton collisions. As shown in the Figure 4, the ratio ( $R_{AA}$ ) of the binary collision scaled transverse momentum yield of hadrons from the heavy ion collisions to that of proton-proton collisions at the same energy is not unity. There is strong suppression of hadrons at high transverse momentum is seen heavy ion data. This suppression is absent for photons which do not interact strongly. A significant final state interaction (which are not present in proton-proton collisions or proton-heavy ion collisions) of the high transverse momentum particles in the created dense partonic medium, is understood to be the explanation behind the observed suppression. These high momentum particles primarily emit radiate gluons and fragment in to lower transverse momentum hadrons, resulting in the redistribution of energy to lower transverse momentum particles.

The eccentricity of the initial overlap region depends on the centrality, and hence impact parameter, of the collision. The overlap region is significantly elongated (i.e. large eccentricity) for the peripheral collisions compared to the central collision. A study of the fourier transform of the  $\phi$  distribution of the particle spectra with respect to the impact parameter plane is performed, and the extracted  $\langle v_2 \rangle$  of the transformation measures the second component of the anisotropy of the distribution, called simply elliptic flow. Measurement shows a significant  $\langle v_2 \rangle$  signal that correlates strongly with the eccentricity, thus indicating early thermalization as well as the likely validity of the hydrodynamical description of this stage of the data. This can be seen in Figure 5 that shows flow as function of centrality and thus the eccentricity of the overlap region.

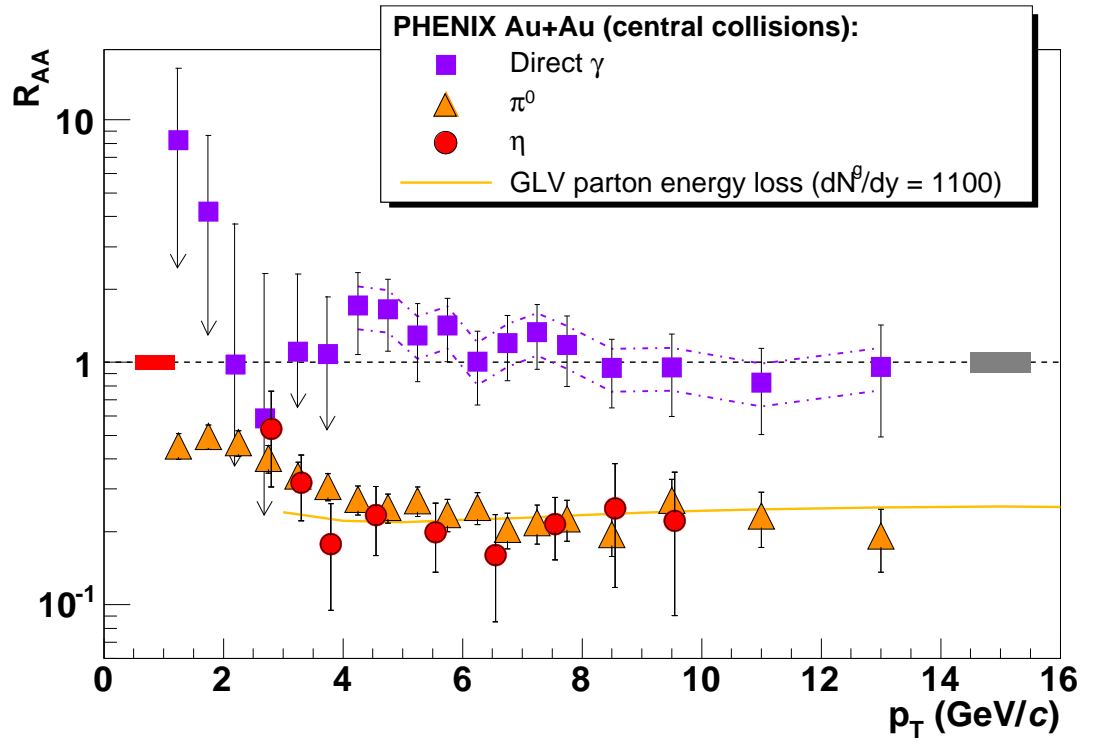


Figure 4.  $R_{AA}(p_T)$  measured in central Au+Au at  $\sqrt{s_{NN}} = 200$  GeV for  $\eta$ ,  $\pi^0$  and direct  $\gamma$ .

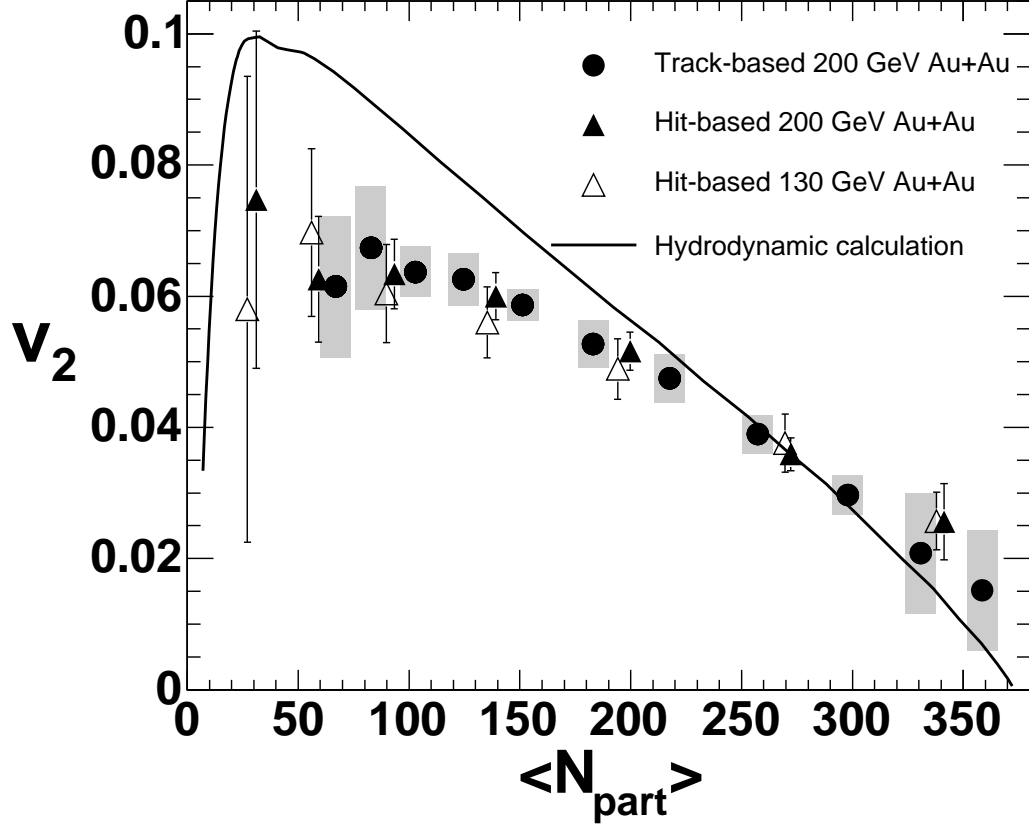


Figure 5. Elliptic flow of charged particles near mid-rapidity ( $|\eta| \lesssim 1$ ) as a function of centrality in Au+Au collisions at  $\sqrt{s_{NN}} = 200$  GeV using two different methods (closed circles and triangles) and at  $\sqrt{s_{NN}} = 130$  GeV (open triangles). Grey boxes show the systematic errors (90% C.L.) for the 200 GeV data. The curve shows the prediction from a relativistic hydrodynamics calculation.

Temperature and  $\mu_B$  characterize the phase space of the QCD matter. Identified particle ratios measurement can be used to study the chemical freeze out parameters and therefore the path in the QCD phase diagram traversed by heavy ion collisions. Using the statistical models, the proton particle ratios in particular can be used to predict the baryochemical potential. Presented in this thesis is the antiparticle to particle ratios measurement of protons, kaons, and pions as a function of collision centrality and transverse momentum as well as an estimate of the  $\mu_B$  for all the four colliding (Cu+Cu 200 GeV, Cu+Cu 62.4 GeV, Au+Au 200 GeV and Au+Au 62.4 GeV). In particular data from PHOBOS, one of the experiments at RHIC, is analyzed. In rest of this chapter are presented a few theoretical models used to describe primary features of the heavy ion collisions of particular relevance to this thesis. An overview of the RHIC facility and relevant details about the PHOBOS experiment are given in the next chapter.

### Models for heavy ion collisions

Following is a brief description of selected models in heavy ions that have bearing on the reported experimental analysis.

#### Thermal Model

The thermal model is a macroscopic approach heavy ion collisions (1), (2), (3), (4), (5). Equation 2.2 gives a most commonly used thermal model based on quantum statistics.

$$\langle n_i \rangle = (2J_i + 1) \frac{V}{(2\pi)^3} \int d^3p \frac{1}{\gamma_s^{-s_i} e^{(E_i - \mu_Q Q_i - \mu_s S_i - \mu_B B_i)/T} \pm 1} \quad (2.2)$$

where

- $\langle n_i \rangle$ : the yield of hadron  $i$
- $J_i$ : the spin of hadron  $i$
- $V$ : the volume in which the hadrons are created
- $\gamma_s$ : strangeness suppression factor
- $s_i$ : the sum of strange and antistrange quarks in hadron  $i$
- $E_i$ :  $\sqrt{p^2 + m_i^2}$
- $m_i$ : mass of hadron  $i$
- $\mu_Q$ : electric chemical potential
- $Q_i$ : charge of hadron  $i$
- $\mu_s$ : strange chemical potential
- $S_i$ : strangeness of hadron  $i$
- $\mu_B$ : baryochemical potential
- $B_i$ : baryon number of hadron  $i$
- $T$ : temperature
- $\pm$ : + for fermions, - for bosons for high energy and temperature both the distributions behave similarly



The free parameters, determined by fits to measured particle ratios or yields, are  $V$ ,  $\gamma_s$ ,  $\mu_Q$ ,  $\mu_s$ ,  $\mu_B$ , and  $T$ . The strangeness suppression factor,  $\gamma_s$ , accounts for incomplete strangeness equilibration when few strange quarks are produced. This has occurred in low energy collisions where strange particles are too heavy to be created abundantly. Full strangeness equilibration would result in  $\gamma_s = 1$ .

### **Transport Model**

The transport model, unlike any other model, tries to follow each particle and its trajectory through space and time. The evolution of the system follows a relativistic transport equation. Nucleons interact with each other by exciting resonances or strings. The decay of these strings produces soft particles. Transport models assumes point like classical particles whose mean free path is very large. This model works well for center of mass energies of  $< 10$  GeV. At higher energies, accounting for the sub-hadronic process is also required, usually done through an additive quark model like in RQMD.

### **Lattice QCD**

An approach to solve the equations of QCD directly is to perform lattice calculations. Here, space and time are discretized (therefore lattice). The properties of infinitely vast matter in equilibrium, and therefore the Equation of State, can be studied [needs reference]. Lattice QCD does not provide a dynamical description, but can give exact input to hydro- and thermodynamical models. It starts with a QCD partition function  $Z$  that is a function of function of the volume  $V$ , temperature  $T$ , and the quark number chemical potential  $\mu$ . After solving the

partition function thermodynamic functions can be derived. Lattice calculations clearly show a QCD phase transition as a function of increasing temperature and predict a smooth cross over.

## CHAPTER 3

### THE PHOBOS EXPERIMENT

PHOBOS experiment is one of the four main experiments of the Relativistic Heavy Ion Collider (RHIC). In the first couple sections of this chapter a brief introduction to the relativistic heavy ion collider followed by a detailed look at the PHOBOS detector is presented. In the later sections of this chapter, the operational details of the PHOBOS experiment are outlined for both online activities during data taking like triggering, data acquisition etc, and off-line activities like the vertexing, tracking etc. A more detailed description of the PHOBOS detector is beyond the scope of this document. Hence, emphasis on description is made for the topics relevant for physics goal of this thesis with citations providing additional details.

#### 3.1 Relativistic Heavy Ion Collider

The Relativistic Heavy Ion Collider (RHIC) is located at Brookhaven National Laboratory in Upton, New York . Figure 6 is a schematic diagram of RHIC facility, details of the RHIC complex design are given in (6), (7). The RHIC was primarily designed to produce heavy ion collisions. The main design features are

- To collide heavy ions (e.g. Au) at top energies of 100 GeV/c per nucleon, resulting in a center of mass energy of 200 GeV/c per nucleon pair. This design also allows p+p collisions of up to 250 GeV/c per nucleon. This is possible because, operational momentum increases with the charge to mass ratio which is  $\sim 1$  for gold ions and  $\sim 2.5$  for protons.

- The initial design luminosity was  $2 \times 10^{26} \text{ cm}^{-2} \text{ s}^{-1}$  for 10 hour long stores for heavy ions.
- Capability to collide a light ion with a heavier ion, for example deuterium on gold, which provided with interesting physics insights.
- Capability to do an energy scan starting from the top energy to the lowest possible energy. This is important to help bridge the gap between the physics at top RHIC energies and the previously performed low energy experiments.

Referring to Figure 6, the four main operational parts of the RHIC accelerator complex are,

- Tandem Van de Graff generator (8), (9) : This is the initial source of the heavy ions. As the name indicates, the tandem is essentially composed of two Van de Graff generators. Negatively charged heavy ions from the ion sputter source are accelerated from the ground potential to +14 MV. These negatively charged ions pass through a stripping foil in high-voltage terminal losing a few of its electrons producing positively charged ions. The amount of electrons lost depends on up on the species. These positively charged ions are passed through the second Van de Graph generator and accelerated back to ground potential. These ions are then transferred to the booster through the Tandem to Booster (TtB) line.
- Alternating Gradient Synchrotron (AGS) Booster : This was constructed as an upgrade to the AGS, hence the name, which increased the ability of the AGS to produce and collide heavier ions than silicon due to its superior vacuum. The ions after being injected

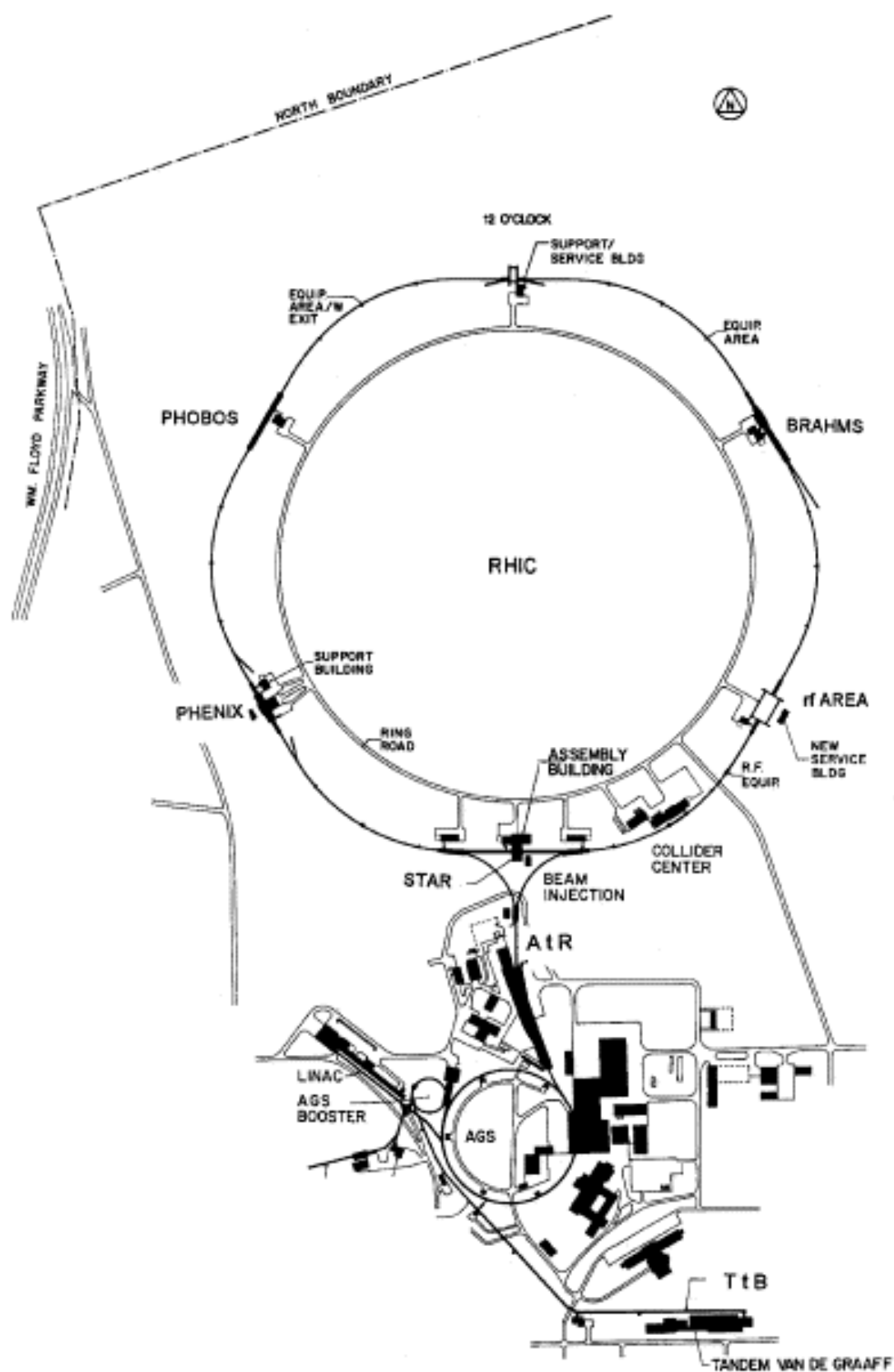


Figure 6. Schematic diagram of the Relativistic Heavy Ion Collider.

into the in the booster are further accelerated in bunches of six, after a multiple injections from the Tandem Van de Graff generator. The ions pass through further stripping foils before entering the AGS through the Booster to AGS (BtA) line.

- AGS : Alternating Gradient Synchrotron has 240 magnets with alternating field directions used to focus the beam in both horizontal and vertical directions. Four booster cycles are used to fill the AGS with 24 bunches, which are then converged into a four bunches which are later injected into the RHIC ring through the AGS to RHIC (AtR) line. Ions are completely stripped of electron before they enter the AtR line.
- RHIC ring : This consists of two separate hexagonally shaped rings (usually denoted by blue and yellow color) intersecting at six points with a circumference of about 3.8 km. Super-conducting niobium titanium magnets (1740 in count) are used to control the trajectory of the particles. Particles accelerate in opposite directions in both the rings and can be made to collide at any or all of the intersection points. The species of the particles in blue and yellow rings can be either same or different as both the rings are operated separately. The technology behind the design of the RHIC synchrotron is referred to as the intersecting storage rings[need a reference to ISR]. It differs from a traditional synchrotron in the sense that the rings are used to store the particles rather than continuously producing them. RHIC operates with 60 bunches at 360 RF buckets in each ring. Only the 56 bunches are filled, the other four are left empty for abort mode. The bunches are 63.9m apart and  $\sim 20$ ns in size. A minimum of 6 bunches are required for

collisions to be possible at the intersection points. The particles are injected in to either one of the rings from the AtR line.

RHIC started its operation in 2000 with a 56 GeV Au+Au run. Since then, it has been producing heavy ion collisions almost every year. The summary of the different collision species and the energy is given in the table (?). RHIC operational for a few months every year due to both the financial and logistic limitations.

TABLE I. Following table gives the summary of different collision species and collision energy as a function of year.

Year	Collisions
2000	Au+Au 56, Au+Au 130 GeV
2001	Au+Au 19.6, Au+Au 130, Au+Au 200 GeV, p+p 200 GeV
2003	d+Au 200 GeV, p+p 200 GeV
2004	Au+Au 200 GeV, Au+Au 62.4 GeV, p+p 200 GeV
2005	Cu+Cu 200 GeV, Cu+Cu 62.4 GeV, Cu+Cu 22 GeV, p+p 200 GeV, p+p 410 GeV
2006	

The following are the four major experiments located at the intersection points. The position of various experiments is described relative to the north most point of the RHIC storage ring, which is referred to as the 12'O clock point.

- BRAHMS (10), (11) : is located at 2'O clock position. This experiment has stopped its operation after the 2006 RHIC run.
- STAR (12), (13) : is located at 6'O clock position. Its a  $4\pi$  detector with an eta acceptance of  $\pm 1$ .
- PHENIX (14), (15) : is located at 8'O clock position.
- PHOBOS (16), (17) : is located at 10'O clock position. This experiment has stopped its operation after the 2005 RHIC run. Its main features include its really large coverage in pseudorapidity and particle identification to a very low momentum.

STAR and PHENIX are the bigger experiments while PHOBOS and BRAHMS are smaller experiments. PHOBOS and BRAHMS are no longer in commission. Since 2000, all the four experiments have delivered very interesting physics observations. The highlights include studies on particle multiplicities and their scaling behavior, suppression of high  $p_T$  particles, jet quenching and particle ratios.

In the next section PHOBOS experiment will be discussed with the detail relevant to analysis of this thesis work.



### 3.2 PHOBOS Experimental Setup

PHOBOS experiment was built with a primary goal of studying the bulk properties of the heavy ion collisions produced at RHIC. Figure 7 is the schematic diagram of the PHOBOS detector. A detailed description of the PHOBOS detector is given in (16). Presented in this section is a summary of all the PHOBOS detector subsystems with an inside out approach, i.e. starting from the subsystem closest to the collision interaction to the one farthest out.

In Figure 7, the right hand top corner shows reference axis of the PHOBOS detector system. The line running through the PHOBOS detector parallel to the z-axis is the beam-pipe. One of the main design goals of the PHOBOS detector was to study particles with very low transverse momentum. To achieve that goal, the detector pipe around the collision interaction point was replaced by a beryllium beam pipe of approximate thickness of 1.0 mm. This reduces the energy loss and multiple scattering while the particles are traversing through beam-pipe compared to the steel material used for the beam-pipe else where. The beryllium beam-pipe is approximately 16 m long and 76 mm in diameter. One of the main cons of using the beryllium beam-pipe was frequent vacuum excursions caused by the thin beam-pipe, which is not a big problem compared to the physics gain.

PHOBOS octagon detector surrounds the beam-pipe and is closest subsystem to the collision interaction point. It has pseudorapidity coverage of  $\pm 3.2$  units from the nominal interaction point. This detector is made up of 92 silicon pad detectors (1.10 m long and 90 mm face diameter) with almost complete azimuthal coverage (except of the holes for the spectrometer arms which will be described later). A transverse view (down the beam-pipe) of this detector

looks like an octagon, hence the name. The frame of the octagon detector is constructed using aluminium. Part of the frame is made of tubes through which chilled waters is run to cool keep the temperature low. Aluminium, with low-Z and low mass, reduces the secondary particle production and the multiple scattering. This detector along with six ring detectors located at the distances of  $\pm 1.3$ ,  $\pm 2.35$  and  $\pm 5.05$  m from the center of the PHOBOS detector are used for measuring the angular distribution of the charged particles with a combined psuedorapidity coverage of  $\pm 5.4$  units. Of the four detectors at RHIC, PHOBOS has made a unique (owing to the wide range of psuedorapidity coverage) and one of the early contribution towards the study of global charged particle distributions [need reference to the first PHOBOS publication]. There a total of 120 silicon pad sensors in the octagon and 60 in the ring detectors.

The vertex detector is next subsystem with two sets of finely segmented silicon pad detector (named the inner and the outer vertex detectors) placed on top and bottom (in y direction) of the octagon detector, with a primary goal to determine the vertex position with an accuracy better than 0.2 mm in z-direction. The psuedo-rapidity coverage of the inner vertex detector is about  $\pm 1.5$  and the outer vertex detector is about  $\pm 0.92$  units and these detector have also been used in the determination of charged particle multiplicity around mid-rapidity. The determination of vertex position is also complimented using other detectors, the actual algorithms used will be discussed in detail in the later part of this chapter.

At this point, it is essential to describe the PHOBOS magnet before discussing the next sub-detector, the Spectrometer. It has two dipole magnets with series current located on the either sides of the beam-pipe. Magnetic field lines produced are perpendicular to the collision

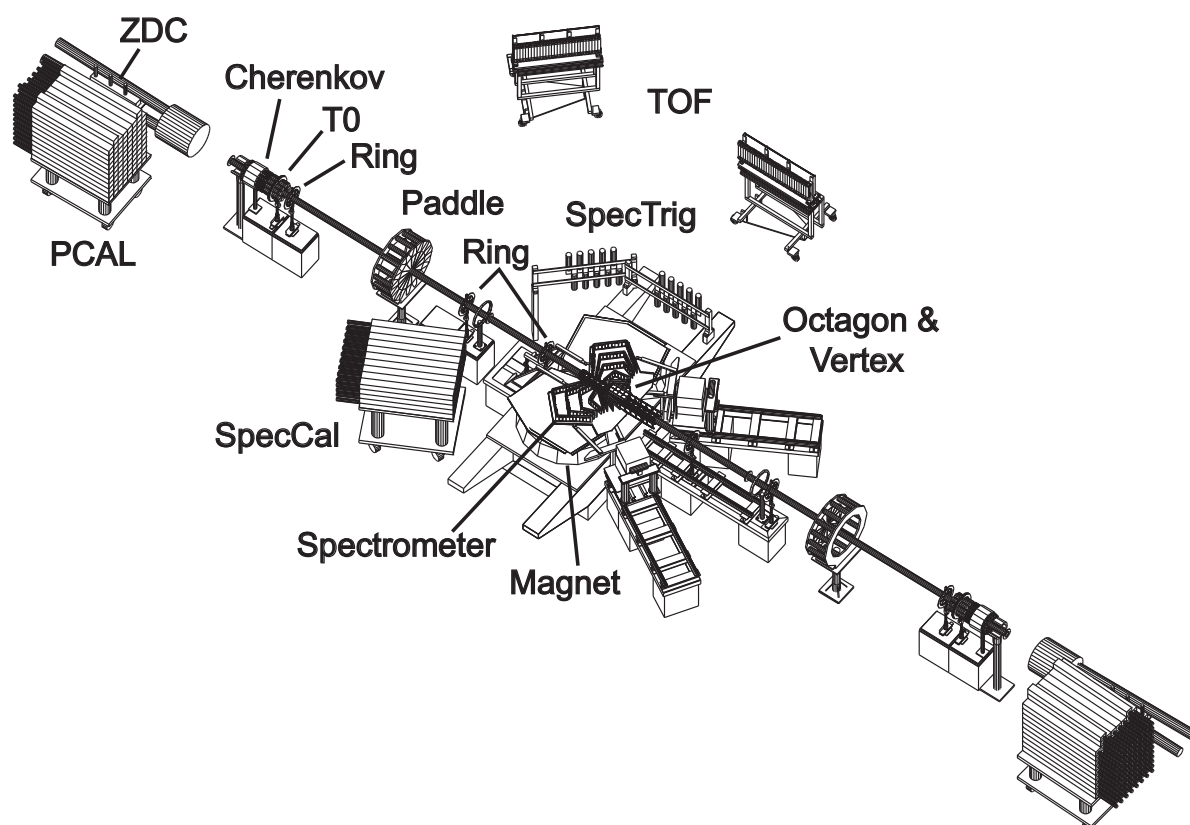


Figure 7. PHOBOS detector with its sub-systems.

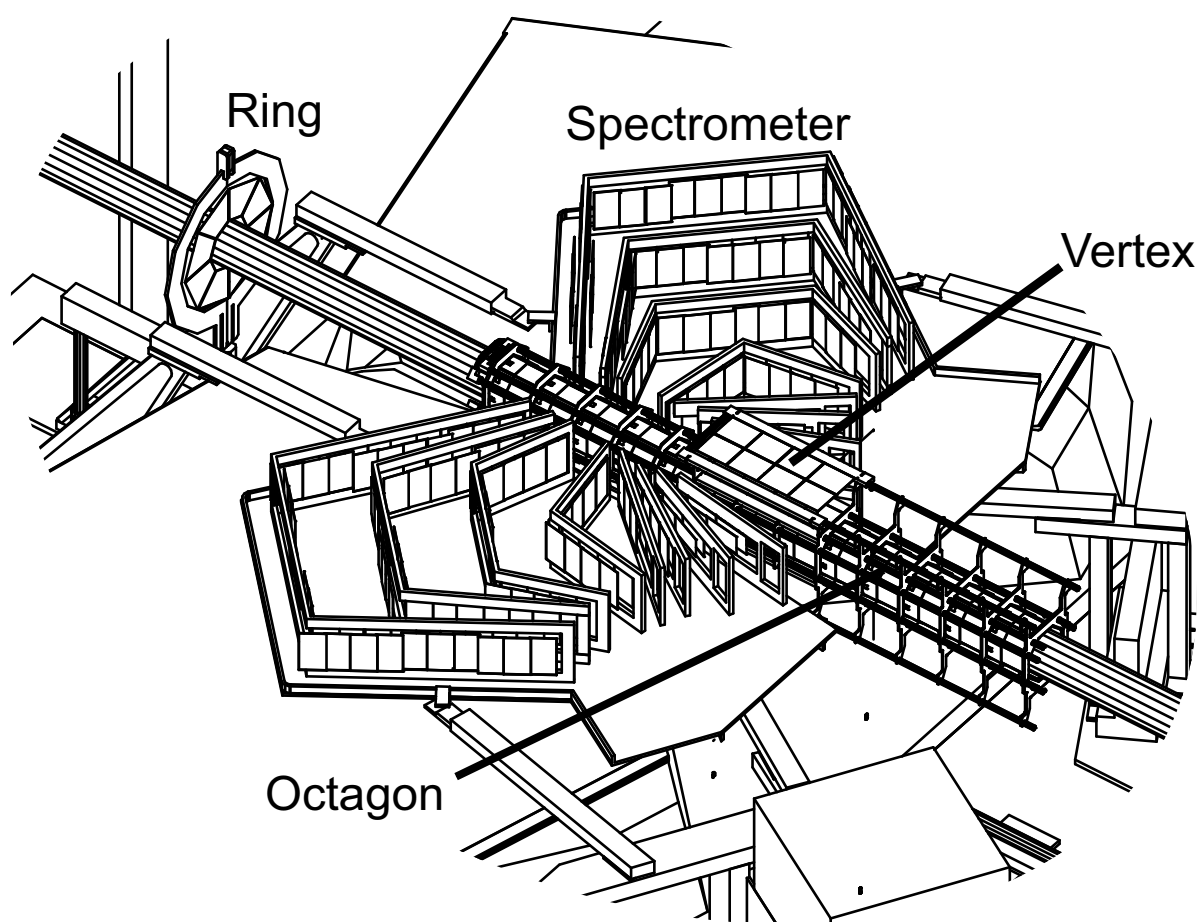


Figure 8. PHOBOS detector with its sub-systems.

axis with opposite polarity in each dipole side. They are designed to produce essentially zero field near and around the beam pipe and collision interaction region. The PHOBOS magnet operates at room temperature and has a total bending power of 1.5 Tm. The magnetic polarity is reversible, a property we exploit to the maximal effect in this analysis and will be described in more detail in the later chapter 4. Equal amounts of data is taken in both the field settings.

### **3.2.1 Silicon spectrometer**

Extending out in the x-y plane after the vertex detector on both sides of the beam-pipe is the tracking spectrometer. This is the main sub-detector for this analysis. A zoomed in view of the spectrometer is shown in Figure 8. Spectrometer consists of two arms of each consisting of 15 layers of highly segmented silicon pads. Each spectrometer arm has a geometrical acceptance of  $\pm 0.1$  radians in the azimuthal angle and 0.48 to 1.37 radians in polar angle ( $0.2 < \eta < 1.4$ ). The spectrometer arm on the positive x-side is called the positive spectrometer arm and the negative x-side is called the negative spectrometer arm. Each arm has 137 sensors and 780 readout chips assembled into 42 multi-sensor modules accommodating a total of 56064 channels. The first 9-layers of the spectrometer, on both sides, are located in the field free region and the rest of the layers are located in the magnetic field region. The hit information in the spectrometer is used to build the trajectory of the particles. The magnetic field bends unlike charged particles in opposite direction and hence the sign charge of the particle can be determined. Using the information from the energy deposited by the particles in the silicon pad detectors and the trajectory of the particles from the hits produced, particle identification is made possible.

Extended out in z-direction are the trigger detectors which include the paddle counters, the Time-Zero (t0) counters, the Cerenkov detectors and the Zero degree Calorimeter (ZDC's).

The paddle counters are scintillation counters, located 3.2 m on each side from the center of the collision interaction point. The pseudo-rapidity coverage of the paddle counters is  $3 < |\eta| < 4.5$ . Each paddle constitutes 16 individual detector slats that form an annulus around the beam-pipe on each side with an inner radius of 7 cm and outer radius of 25.6 cm. The pair of these counters form one of the main basis in the triggering system of PHOBOS.

The T0 counters and the Cerenkov counters are made of four Bicron (see footnote 3) BC800 Cherenkov radiators of 25 mm thickness and 50 mm diameter coupled to fast 50 mm diameter phototubes. These detectors are centered on a circle of diameter 151 mm around the beam line. The T0 counters also provide information about the collision vertex position from the time signals, its used in the triggering system.

The zero degree calorimeters (ZDCs) are instruments installed in all RHIC experiments to provide luminosity monitoring. The calorimeters detect forward moving neutral fragments originating from the collided ions. They are used in the online triggering system when the backgrounds get high and sometimes also in the off-line good event selection.

The next section describes the data acquisition system with an introduction to few terminology that are frequently used in the rest of the text.

### 3.3 Data acquisition

#### **RHIC stores and PHOBOS data**

A **Store** is defined by the RHIC experimental facility. It starts with ramping up of the beam to full intensity desired for collisions as driven by the ultimate luminosity goals. During this process localized bunches of the ions are injected in to the RHIC rings (Section 3.1), ramped up to desired collision energy, and tuned so that bunches traveling in opposite directions collide with each other at the interaction point of all the four experiments. After the tuning is done the experiments are notified that the beam is ready for the data taking. As the time progresses beam luminosity decreases due to collisions and other losses, including spreading out of bunches in time. At some point, often determined by the ‘voting’ system by the other experiments the RHIC experimental facility ramps down the beam. From ramp up to ramp down takes typically it takes about 4-6 hours. Usually there is a hour gap between each store.

Events recorded by the PHOBOS DAQ are grouped into files of 1GB size. Each file is called a **Sequence**. Sequences are grouped together into **Runs**. Run is not physical quantity but just an identifier. Each run on an average has 60 sequences. Data in each store is divided into runs and which are further divided in to sequences. The starting and stopping of the run is determined by a shift crew members. The number of sequences in a run depends solely on how long the run lasted. In PHOBOS, the practice has been to make a note of any special conditions during which the run was recorded. This information usually helps in the subsequent data analysis.

## Data acquisition

Produced collisions are recorded by the PHOBOS data acquisition system and eventually archived onto a tape drive system maintained by the RHIC Computing Facility(RCF). The trigger system, as explained in [needs reference for the next section], decides if a given event is to be recorded. For every collision event that is accepted, information from 150,000 silicon and 200 scintillator channels have to be recorded at the same time. Once the trigger is satisfied, initially the event is written into a 600 GB local pool and later to central RHIC storage system via a 30 MB/s Gigabit ethernet channel. PHOBOS data acquisition was initially designed to record events at 10 Hz. During the 2005 run the data acquisition was upgraded to record events at 400 Hz, which significantly improved the number of events to tape. Table II lists the total number of events recorded (in Millions) over the five years of PHOBOS data taking.

TABLE II. Following table gives the summary of all the data recorded on to the tape in millions of events units for different collision species and collision center of mass energy.

GeV	410	200	130	62.4	55.9	22.5	19.6
p+p	20	100					
d+Au		150					
Cu+Cu		400		110		20	
Au+Au		200	4.3	22	1.8		$\sim 1$



### 3.4 Hardware trigger setup

Like any other collider experiment, there are a lot of collisions produced at the intersection point of the PHOBOS experiment. Its interesting to record all the data for the purpose analysis. But, it is not possible due to logistic reasons like maximum rate at which events can be written out using the data acquisition (DAQ) system and availability of tape drive to store the events etc. Hence, the PHOBOS experiment typically operated with a two level hardware electronic trigger logic to determine if an event has to be written out using the DAQ or can be ignored. The trigger system is supported by the following different trigger counters and the decision making electronics,

- Paddles
- T0's
- Cerenkov's
- Zero degree calorimeter
- Spectrometer trigger

If an event passes the first level of the trigger logic, which is primarily based on the information from the paddles, all the front end electronics of the various detector sub-systems are prepared to start writing out all the channels. A much more sophisticated decision is made using the second level of the trigger logic. If the event passes even the second level, its completely written out in to the local pool [need reference from previous chapter] else a ‘fast clear‘ signal is sent to all the front end electronics to clean the buffers and prepare for the next event.

At this point, the definition of Crossing clock is important to further discuss the trigger logic. The Crossing clock is a signal obtained from RHIC operations every time a bunch crossing occurs at the PHOBOS interaction region. The most simple trigger would be to record an event every time there is a signal from crossing clock, as one would expect an event every time the bunches in the opposite direction cross each other. In reality, collisions occur with a very low probability for a given bunch crossing and its necessary to trigger on the collisions using the detector trigger system. Further more, the beam can also interact with residual gas in the beam pipe resulting in ‘beam gas events’ which again due to logistic reasons and physics reasons are not recorded. However, Crossing clock signal is used as a timing reference point for all the trigger electronics.

A schematic diagram of the trigger implemented for the Paddle Counters is shown in year 2004 for Au+Au data is shown in Figure 9.

#### **Level 0 :**

For the data in this thesis, Level 0 primarily uses the information from the paddle’s, and T0’s. It requires a coincidence between the paddles hit on the both sides of the PHOBOS detector central point. The coincidence gate width is 10 ns this is initially determined from simulations and later fine tuned using the actual data. The main goal behind this is to eliminate beam-gas events occurring outside the collision region. As [needs a figure] shows the simulation of the time difference between the negative and positive side of paddles. The beam gas has larger probability of occurring away from the center of the interaction region and hence, such events would lie on the edges of the given distribution shown in a different color. Requiring at

least one paddle slat hit on both side also corresponds roughly to min-bias trigger selection. Its still considered to be almost as the efficiency of this trigger is almost 100% for central events while less then that for peripheral events. These efficiencies are determined by using the mocked events and detector simulation, later on with cross from data [refer to Richards thesis]. After an event passes this Level 0 logic, the DAQ starts preparing to read the event out to the local pool.

### **Level 1 :**

Level 1 logic of the PHOBOS trigger system is usually a mixture of different kinds of triggers. It is a combination of both the pre-scaled min-bias trigger from the Level-0 and a vertex trigger. The vertex trigger is implemented using the timing signals of the T0. It is essentially a time difference between the first hit T0 on either side of the detector. This trigger is then calibrated, so that only events produced between  $Z=-15$  cms to  $Z=+20$  cms are recorded. The calibration is performed using real data. Events that pass the Level-1 are eventually written out to the local disk pool.

One other essential signal that forces an event to be written out is the Time calibration signal from the TDC of the TOF. This is signal that is produced at regular intervals.

All the trigger logic is read out in the form of a 32-bit word, 16 bits for each level of logic. Not all the bits are used for the data recorded in this thesis. In Table III and Table IV are listed the different bits are their assignments of the most extensively used trigger logic for both Cu+Cu and Au+Au data. Figure 10 shows the efficiency of different trigger bits as function of paddle mean signal.

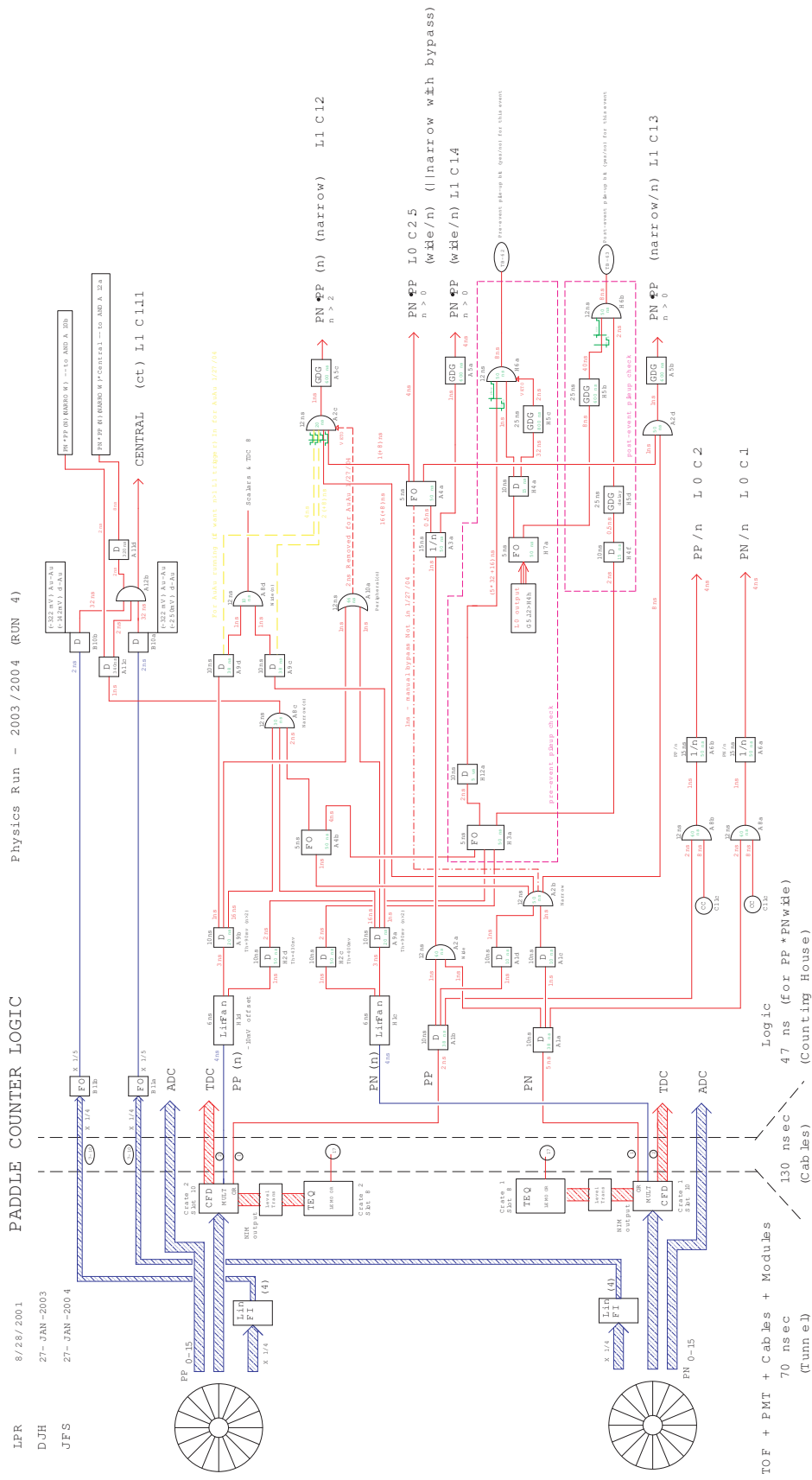


Figure 9.

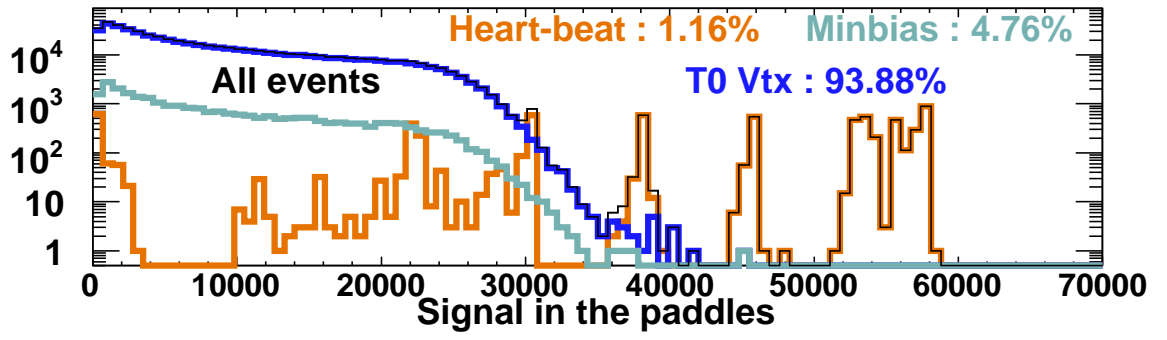


Figure 10. Cu+Cu 200 GeV L1 trigger efficiency as function of sum of the signals in both the paddles.

TABLE III. Description of the trigger bits that were turned on for Cu+Cu 200 GeV and 62.4 GeV runs analyzed in this thesis.

Bit	Description	Scale down
L0		
4	Coincidence between first paddle that is fired on the positive and the first paddle on the negative side, with a coincidence gate width of 10ns	1
5	Coincidence between the first T0 that is fired on the positive and the first T0 on the negative side, with a coincidence gate width of 6ns	1
9	TIMECAL gives out a pulse with uniform interval required to calibrate the TOF	1
14	Crossing Clock is the clock input from the RHIC experimental facility at the beginning of every bunch	1
15	VETO	0
L1		
16	Pre-scaled output from L0	1024
17	This a paddle coincidence trigger similar to the bit-4 from L0 with a pre-scale. It additionally requires at-least one paddle hit. It is called the min-bias bit.	64
20	This a T0 coincidence trigger similar to bit 5 but with pre-scale.	256
23	This is the T0 vertex trigger. Tuned to record data with a vertex range of -10cms to +15 cms	1
24	Heartbeat - is the same as the bit-9 from L1	1
23	Similar to bit 23 with a required coincidence with ZDC	1
31	BUSY	-

TABLE IV. Description of the trigger bits that were turned on for Au+Au 200 GeV and 62.4 GeV runs analyzed in this thesis.

Bit	Description	Scale down
L0		
4	Coincidence between first paddle that is fired on the positive and the first paddle on the negative side, with a coincidence gate width of 10ns	1
5	Coincidence between the first T0 that is fired on the positive and the first T0 on the negative side, with a coincidence gate width of 6ns	1
8	Uniform signal as input to the DAQ, to keep it from shutting down	1
9	TIMECAL gives out a pulse with uniform interval required to calibrate the TOF	1
14	Crossing Clock is the clock input from the RHIC experimental facility at the beginning of every bunch	1
15	VETO	0
L1		
16	L0	1024
17	This a paddle coincidence trigger similar to the bit-4 from L0 with a pre-scale. It additionally requires at-least one paddle hit. It is called the min-bias bit.	64
20	This a T0 coincidence trigger similar to bit 5 but with pre-scale.	256
23	This is the T0 vertex trigger. Tuned to record data with a vertex range of -10cms to +15 cms	1
24	Heartbeat - is the same as the bit-9 from L1	1
31	BUSY	-

### 3.5 Online and off-line calibration of the signals

### 3.6 Vertex reconstruction

In PHOBOS, the collisions can span  $\pm 60$  cm in z-direction around the center of the detector. Due to this large variation in vertex position, more than one sub-detector is used for vertex determination including the Vertex detector, Octagan detector and Spectrometer. Different algorithms used with the various sub-detectors will be briefly described in the rest of this section. These different algorithms have considerable overlap, which allows for cross check. A more detailed description is available at (18).

#### **“ZVertex” - using the Vertex detector**

The “ZVertex” method is one of the first developed vertex reconstruction algorithms. It reconstructs the vertex in z and y co-ordinates of the event vertex with a very good accuracy, and x co-ordinate with a limited accuracy. ZVertex algorithm uses the top and bottom layers of the vertex detector separately, and a comparison between them for reconstruction quality parameter estimation. Reconstruction process using this technique is a two step process. In the first step, cluster of merged hits (with a minimum threshold) are obtained. Plotting the number of pads in the cluster as function of z position results in a distribution as shown in Figure 11, (18), top histogram. The peak of the distribution gives the maximum probability of finding the z co-ordinate of the vertex. In the second step, combinations of clusters from the two layers of the vertex detector are projected back on to the  $y=0$  plane. The z co-ordinate of the vertex is determined by searching (with the reduced search range from the previous step) projected position distribution. A similar procedure of applied for determining the y co-ordinate of the



reconstructed vertex, except in this case a projection on to the  $x=0$  plane is considered. The reconstruction resolution of this algorithm in  $x$ ,  $y$  and  $z$  co-ordinate are  $2424 \pm 32$ ,  $163 \pm 1$  and  $85 \pm 1 \mu\text{m}$  respectively.

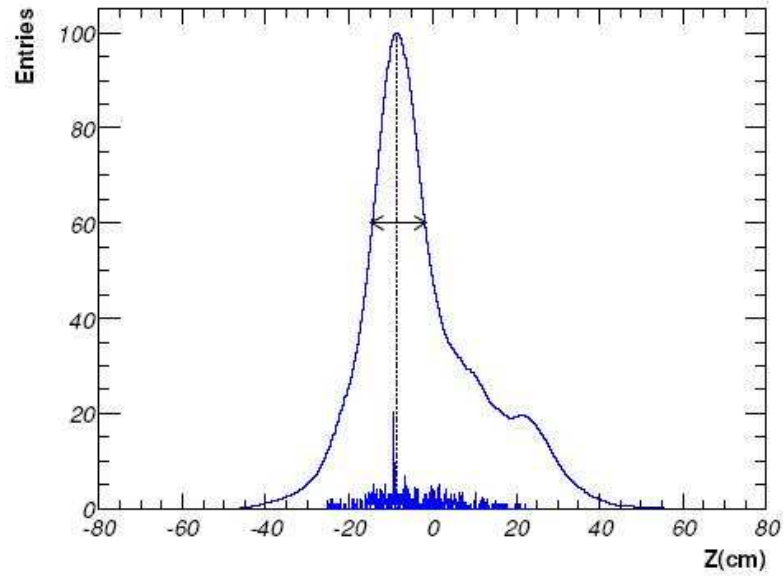


Figure 11. The vertex algorithm using the vertex detector for a typical DATA event. The top histogram is the Probability Histogram, which is used to determine the search range in the Position Histogram (the smaller histogram). The peak in the Position Histogram corresponds to the found vertex, the arrow indicates the typical peak-search range in the Position Histogram.

### **“OctMainVertex” - Using the Octagon detector**

This method uses the Octagon detector to reconstruct the vertex and only reconstructs the z-position. This algorithm is based on hit density (integrated over the  $2\pi$  acceptance of the Octagon detector) distribution as a function of z position, and has peak around the actual vertex position. The mean of the gaussian fit to the peak gives the reconstructed z co-ordinate for event vertex and the rms value the quality parameter. The reconstruction efficiency of the algorithm depends on the centrality of collision. This algorithm was primarily used in study of the Au+Au data. A different algorithm based on the energy deposited in the Octagon detector with improved accuracy (which was introduced much later) is used for the study in Cu+Cu data, a description of the algorithm is given later in the section.

### **“SpecMainVertex” - Spectrometer detector**

SpecMainVertex and SpecVtxPN (description in the following subsection) both use the Spectrometer sub-detector. In this reconstruction algorithm, initially the hits are merged to form clusters in the first couple of layers of the spectrometer (in the magnetic “field-free” region). Using a road following algorithm, vertex less straight line tracks are reconstructed. Tracks with  $\chi^2$  probability  $< 1\%$  are thrown out. Of the remaining tracks, pairs of tracks are considered at a time. For each pair, the mid point of distance of closest approach (DCA) is histogrammed in three dimensions. The peak of the histogram, in all the three co-ordinates independently gives the corresponding reconstructed vertex position in the different co-ordinates. A spread of the DCA distribution obtained through a second iteration through all the tracks gives the vertex reconstruction quality parameter. This has a vertex resolution of  $585 \pm 7$ ,  $385 \pm 5$  and  $593 \pm 10$

$\mu\text{m}$  in x, y and z co-ordinates. The only con of using the spectrometer for reconstructing a vertex is its very small radial acceptance, which makes it harder to find at least two tracks with in the spectrometer for peripheral collisions.

### **“SpecVtxPN” - Spectrometer detector**

This vertex finding algorithm is similar in implementation to the previous algorithm, except for a few differences in the detail. Straight tracks constructed using combinatorics in the four layers of the spectrometer, allowed to miss a hit on maximum one layer. These tracks are then fit with three point straight lines, and tracks with  $\chi^2$  fit probability more than  $10^{-6}$  are retained. A cone projection is defined for the layer with the missing hit to search for the missing hit while trying to maximize the  $\chi^2$  fit probability. Same logic is used to extend the tracks to the fifth and sixth layers. Once all the tracks are constructed a MINUIT minimization algorithm is used to obtain the vertex position, that minimizes the total distance from all the tracks. This is one of the slowest vertex finding algorithms.

### **“RMSSelVertex” - Combined vertex**

This algorithm is designed to pick the best of the above mentioned algorithms. This algorithm makes a selection based on the quality parameters. The cuts on the selection criterion are obtained from Monte-Carlo studies. This is primarily used in the study of Au+Au data set.

The following two algorithms are exclusively used in study of Cu+Cu data. There is no disadvantage in using these for Au+Au data. These algorithms were developed later in PHOBOS running, after the Au+Au data taking and before Cu+Cu data taking.

### **“OctProbMultVertex” - Octagon detector**

Similar to OctMainVertex this algorithm uses the Octagon detector. Unlike the OctMainVertex which uses the primarily the hit count information this algorithm also considers the energy deposited in the silicon of the octagon detector. This algorithm can be summarized in three steps. In the first step, the hits are merged together to form clusters (with a minimum cut off energy in MIPS) and, the energy and number of hits that form the cluster is recorded. In the second step, probability of the vertex position from each is determined. As demonstrated in Figure 12, the probability of the event vertex depends the size of the cluster. In the final step, the probability distributions from all the clusters are overlayed as a function of  $z$ . The point with maximum probability is determined to be the reconstructed vertex position. The reconstruction quality parameter is obtained from the statistical study of the Monte-Carlo data set. This algorithm has a reasonable vertex resolution, as shown in Figure 13 as function of multiplicity. A complimentary algorithm with a better resolution, OneTrackVertex, is also used for peripheral events where the OctProbMultVertex does not demonstrate the desired performance for a particular analysis.

### **OneTrackVertex**

One track vertex similar to RMSSelVertex, is a complimentary vertex finding algorithm but its not a average vertex like RMSSelVertex. As the name suggests, it relies on being able to find at least one track. In the first step, using combinatorics between the two different layers of the vertex detector, straight line tracks are determined. DCA to beam-orbit cut is applied, and an average of all surviving tracks is obtained (As long as at least one track survives). The

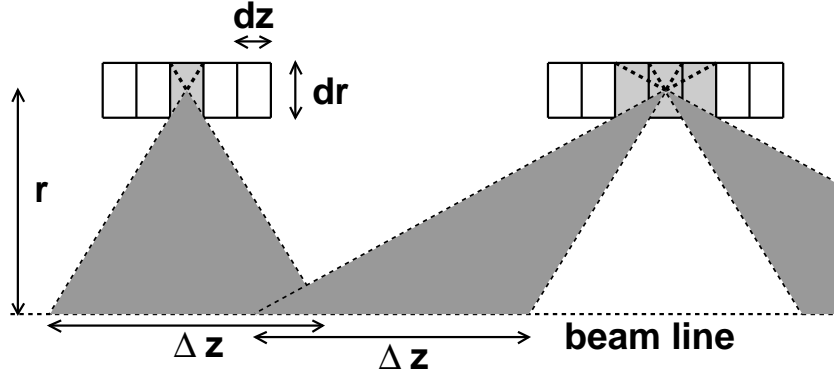


Figure 12. Examples of hits from primary particles leaving signals in one (left) or three (right) active elements of the silicon detector and the ranges of possible vertex positions,  $\delta z$ , defined by simple geometrical calculations.

same procedure is repeated with the first couple of layers of the spectrometer. If either the vertex reconstructed from the above two mentioned tracks agree with each other or one of them agrees with the previously reconstructed vertex, then vertex finding is considered successful. This vertex finding algorithm has a reasonable reconstruction efficiency for peripheral events as it requires at the least one track to be available.

A summary of the reconstruction resolution for selected vertex finding algorithms is presented in Table V. As the tracking relies on seeds that point back to the reconstructed vertex, a good resolution and a control over quality parameters is essential for further analysis.

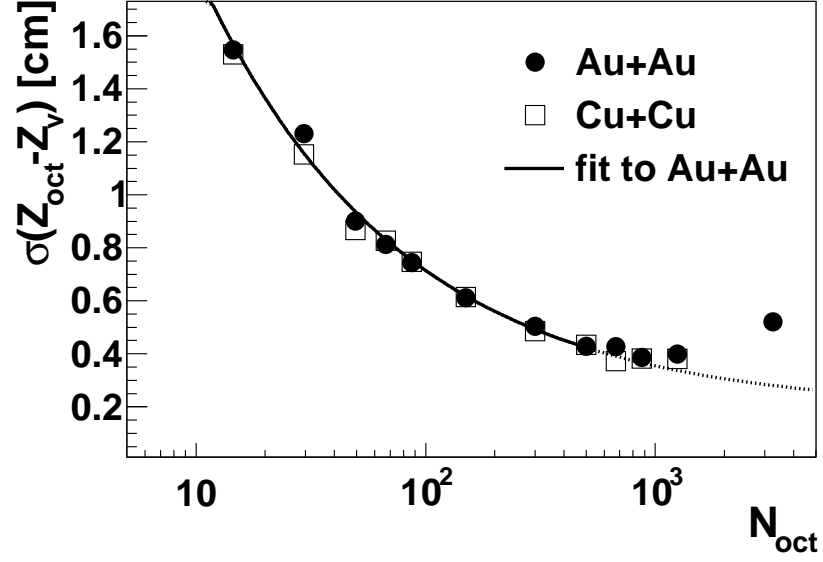


Figure 13. The error of the reconstructed vertex position,  $\sigma(Z_{oct} - Z_v)$ , as a function of the number of charged primary particles registered in the octagon,  $N_{oct}$ , for Au+Au and Cu+Cu collisions at  $\sqrt{s_{NN}} = 200$  GeV.

TABLE V

RECONSTRUCTED VERTEX RESOLUTION FOR DIFFERENT VERTEX ALGORITHMS.

Vertex Algorithm	X-resolution ( $\mu\text{m}$ )	Y-resolution ( $\mu\text{m}$ )	Z-resolution ( $\mu\text{m}$ )
SpecVertex SpecPN	$219 \pm 3$	$297 \pm 3$	$271 \pm 4$
SpecMainVertex	$585 \pm 7$	$385 \pm 5$	$593 \pm 10$
ZVertex	$2424 \pm 32$	$163 \pm 1$	$85 \pm 1$
RMSSelVertex	$238 \pm 4$	$182 \pm 2$	$81 \pm 1$

### 3.7 Centrality and Event Selection

This sub-section brief introduction to the concepts of centrality and event selection.

#### **Centrality**

Centrality is measured using more than one sub-detector. A correlation between the energy deposited in a given sub-detector and the collision centrality is studied using Monte-Carlo simulations, in particular with geometry based on glauher model. The correlation function developed using the Monte-Carlo studies is used with the data to estimate the number of participants. In Table VI is given the relation between the % cross section and average number of participants in the given bin. The first column represents the bin number, which is arbitrary, as used in PHOBOS.

#### **Event Selection**

Off-line event selection is primarily based on online (refined) event selection cuts and reconstructed vertex cut. Off-line event selection is different for the Cu+Cu data set from the Au+Au data set, due to their different triggering schemes.

#### **Cu+Cu 200 GeV and 62.4 GeV**

Following is the off-line event selection used for the Cu+Cu data set,

- Valid OctProbMultVertex and  $\text{Abs}(\text{OctProbMultVertex.vz}) < 9$
- Valid OneTrackVertex
- No HeartBeat
- $\text{Abs}(\text{PaddleTDiff}) < 5$

TABLE VI

Bin ber	Num- ber	Centrality cross- section	Number of participants			
			Cu+Cu		Au+Au	
			200 GeV	62.4 GeV	200 GeV	62.4 GeV
17		0 – 3%	$106.3 \pm 3.55$	$102.3 \pm 3.62$	$361 \pm 11$	$349 \pm 11$
16		3 – 6%	$100.3 \pm 4.30$	$95.3 \pm 4.38$	$331 \pm 10$	$325 \pm 10$
15		6 – 10%	$91.3 \pm 4.68$	$88.3 \pm 4.78$	$297 \pm 9$	$288 \pm 9$
14		10 – 15%	$79.3 \pm 4.76$	$76.3 \pm 4.79$	$255 \pm 8$	$248 \pm 8$
13		15 – 20%	$67.3 \pm 4.49$	$65.3 \pm 4.38$	$215 \pm 7$	$209 \pm 7$
12		20 – 25%	$57.3 \pm 4.18$	$55.3 \pm 4.04$	$180 \pm 7$	$174 \pm 13$
11		25 – 30%	$47.3 \pm 3.78$	$47.3 \pm 3.74$	$150 \pm 6$	$140 \pm 10$
10		30 – 35%	$30.3 \pm 3.43$	$38.3 \pm 3.39$	$101 \pm 6$	$124 \pm 6$
9		35 – 40%	$33.3 \pm 3.15$	$32.3 \pm 3.08$	$82 \pm 6$	$98 \pm 6$
8		40 – 45%	$27.3 \pm 2.87$	$25.3 \pm 2.80$	$65 \pm 6$	$78 \pm 6$

- Valid L1 timing
- Valid TAC bit

Requiring a valid reconstructed vertex ensures a good triggering efficiency. No heartbeat gets eliminates the triggered by the heart beat signal which is about 1.16% of the total recorded data, as explained in the previous section. A proper paddle time eliminates any residual beam-gas events. A Valid TAC bit implies requiring T0 vertex triggered data, for good event distribution with in spectrometer acceptance.



### **Au+Au 200 GeV and 62.4 GeV**

Following is the event selection used for Au+Au data set :

- Valid RMSSelVertex and  $\text{Abs}(\text{RMSSelVertex.vz}) < 10$
- No HeartBeat
- IsCol
- $\text{TrgT.Extra}[47]==0 \& \& \text{TrgT.Extra}[62]==0$
- Valid TAC bit

Au+Au off-line trigger is almost similar to Cu+Cu except for a few additional hardware requirements. The valid RMSSelVertex ensures good event selection. No heartbeat and Valid TAC similar to as explained in previous sub-section for Cu+Cu. IsCol is hardware trigger, which is a combination of paddle time difference and number of paddles hit. This trigger is tuned for good events and eliminating beam-gas. “ $\text{TrgT.Extra}[47]==0 \& \& \text{TrgT.Extra}[62]==0$ ” are again hardware triggers for identifying pileup events and not include them in the analysis by requiring them to be zero.

## CHAPTER 4

### OVERVIEW OF THE ANALYSIS

Starting with the definitions, relevant to this analysis, outlined in this chapter is the general principal of this analysis.

#### Definitions

Detectors in general, and the PHOBOS silicon spectrometer in particular, have a limited phase space coverage. This is not necessarily a negative statement, it is a mere fact. Hence, all the particles that are produced as an outcome of the collision are not reconstructed by the detector. Its the duty of the experimentalist to study and understand the relation between “reality” and “measurement”. Following are a few definitions commonly used with detectors about different kinds of yields needed to further the discussion on the produced (reality) and reconstructed (measurement) particles,

- Primary yield ( $Y_{pri}$ ): This is the particle yield that is produced at the at collision interaction point.
- Secondary yield ( $Y_{nonpri}$ ) : As the particles move away from the collision interaction point and swim through the detector material, the yield of the particles is modified. This is modification in the yield is due to two reasons. Firstly, the decay of the particle heavier particles to lighter particles. Secondly, interaction of the particles with the detector either causing absorption and/or additional particle production also effecting the yield of the

particles. This net modification to the yield, due to both the above mentioned reasons, is called the non-primary yield.

- Reconstructed yield ( $Y_{reco}$ ) : This is yield of the particles that are reconstructed using the detector.

Following is the relation between the primary and non-primary yields for a given species of particle,

$$\frac{Y_{pri}}{Y_{pri} + Y_{nonpri}} = C_{pri+nonpri}^{pri} \quad (4.1)$$

Following is the relation between the primary and non-primary with the reconstructed yields,

$$\frac{Y_{pri} + Y_{nonpri}}{Y_{reco}} = C_{reco}^{pri+nonpri} \quad (4.2)$$

From Equation 4.1 and Equation 4.2,

$$Y_{pri} = C_{pri+nonpri}^{pri} * C_{reco}^{pri+nonpri} * Y_{reco} \quad (4.3)$$

$C_{pri+nonpri}^{pri}$  is called the non-primary correction and  $C_{reco}^{pri+nonpri}$  is called the acceptance correction. Non-primary correction is dealt with in detail in a later chapter 7. To further understand the acceptance correction the term  $C_{reco}^{pri+nonpri}$  can be broken down into its components,

$$C_{reco}^{pri+nonpri} = acc_{geom}^{pri+nonpri} * eff_{reco}^{geom} \quad (4.4)$$

Where  $acc_{geom}^{pri+nonpri}$  stands for geometrical acceptance and  $ef f_{reco}^{geom}$  stands for the track reconstruction efficiency. To demonstrate the difference between geometrical acceptance and tracking reconstruction efficiency consider two almost similar hypothetical detectors shown in Figure 14 and Figure 15. Figure 14 has two sub-detectors called positive and negative silicon detectors of same shapes but placed asymmetrically on both sides of center of the detector, hence their geometrical acceptance is different. Both the sub-detectors have silicon pixel, represented by square boxes, of the same size. Either of them do not have any bad silicon pixel channels (which is highly unlikely in reality) and hence they will be able to reconstruct particles with the same efficiency. Figure 15 shows two sub-detectors of same shapes but placed symmetrically on both sides of center of the detector, hence the geometrical acceptance would be the same for both the sub-detectors. The red cells in the positive silicon detector of Figure 14 represent bad silicon pixels, leading to better reconstruction efficiency of the negative silicon detector which has all working pixels. Bad channels are a characteristic of the detector, that develop over its life time as consequence of exposure to radiation etc. This second scenario is more similar in construction to the PHOBOS detector. The positive and negative arms of the PHOBOS silicon spectrometer are located symmetrically on both sides of the collision interaction point. Hence positive and negative arms of the PHOBOS silicon spectrometer have the same geometrical acceptance but have different track reconstruction efficiency.

Equipped with these general definitions, in the next section the main principle of this analysis is given and some details are outlined concerning how the tracking efficiency correction is dealt with in this analysis.

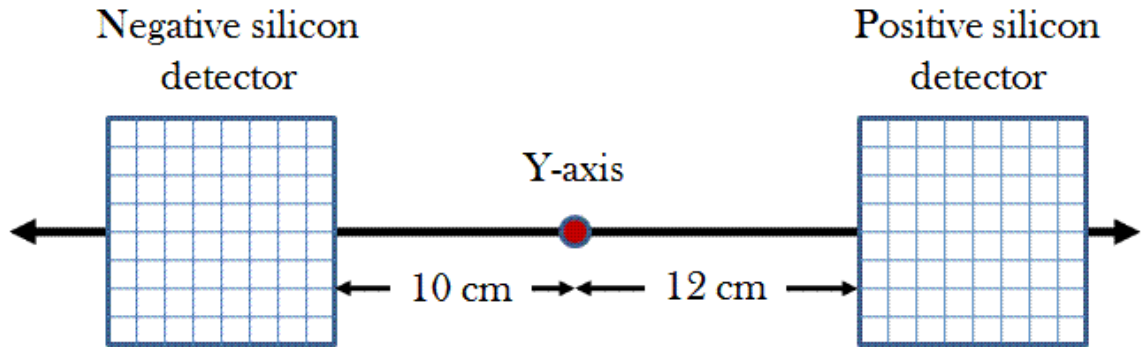


Figure 14. An example of a detector with two of its sub-detectors (named positive and negative silicon detector) of placed asymmetrically on both sides of the y-axis. The boxes inside the sub-detectors represent silicon pixels.

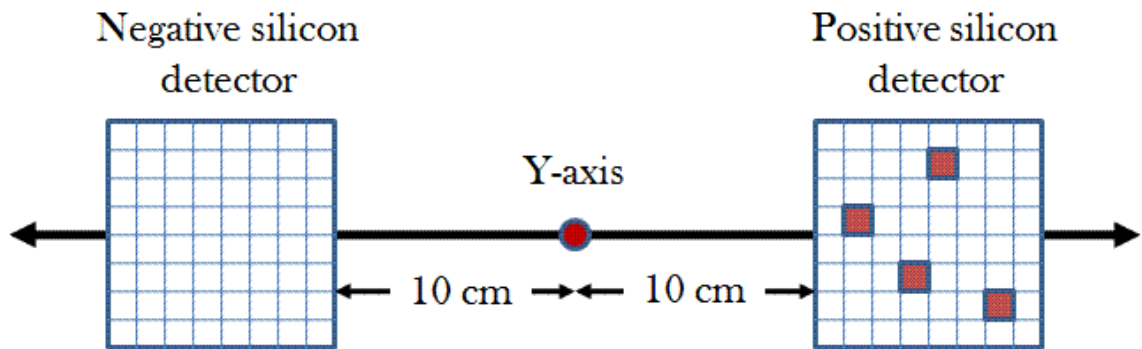


Figure 15. An example of a detector with two of its sub-detectors (named positive and negative silicon detector) of the same shape placed symmetrically on both sides of the y-axis. The boxes inside the sub-detectors represent silicon pixels. The red color pixel are the bad channels.

### The main principle behind the analysis

Mathematically, anti-particle to particle ratios can be represented as,

$$Ratio = \frac{\overline{P_{pri}}}{P_{pri}} \quad (4.5)$$

Where  $P_{pri}$  represents the yields of either protons, pions or kaons and  $\overline{P_{pri}}$  their respective anti-particles. Particles identification using the PHOBOS detector is detailed in the section 6.1. Using the Equation 4.3 in Equation 4.5

$$\frac{\overline{P_{pri}}}{P_{pri}} = \frac{\overline{C_{pri+nonpri}^{pri}}}{C_{pri+nonpri}^{pri}} * \frac{\overline{C_{reco}^{pri+nonpri}}}{C_{reco}^{pri+nonpri}} * \frac{\overline{P_{reco}}}{P_{reco}} \quad (4.6)$$

Where,  $C_{pri+nonpri}^{prim}$  and  $C_{reco}^{pri+nonpri}$  represent the corrections for particles.  $\overline{C_{pri+nonpri}^{prim}}$  and  $\overline{C_{reco}^{pri+nonpri}}$  represent the corrections for anti-particles. While the non-primary corrections are different for particles from anti-particles due to differences in absorption properties etc, the tracking efficiency correction is the same for both the particles and anti-particles. The equal tracking efficiency correction is not a consequence of the fact that it is same detector that is being used to measure antiparticle to particles, rather it is the selected subset of the data (i.e. same bending direction but opposite magnetic polarity) that is chosen to obtain the ratios. Revisiting of the PHOBOS spectrometer and the magnet are essential at this point to further elaborate the previous statement.

PHOBOS spectrometer (design details in section 3.2) has very small  $\phi$  acceptance of  $\pm 0.1$  radians, and can be approximated to a plane. Spectrometer arms, that are symmetrically placed

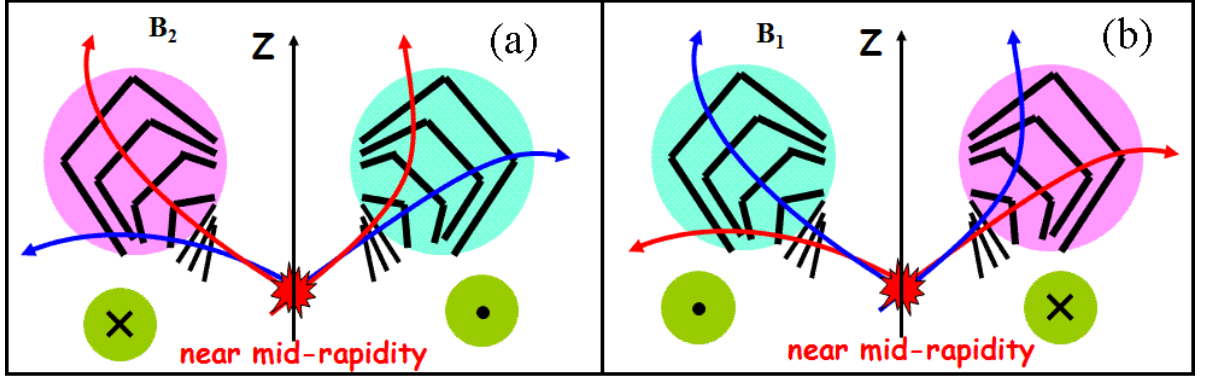


Figure 16. Cartoon of the PHOBOS spectrometer (schematic diagram is given in Figure 7) in two different magnetic field setting  $B_2$  and  $B_1$  is shown in panels (a) and (b) respectively. The Spectrometer is represented by black color lines, particles in blue color arrows, and anti-particles in red color arrows. The region where magnetic field is pointing into the page is represented by the pink color (with a cross) and green color (with a dot) for field pointing out of the page.

on either side of the beam-pipe, approximately have the same geometrical acceptance but the reconstruction efficiency is different as they both have different set of bad silicon pixels etc. The outer layers of both the spectrometer arms are located in a magnetic field of strength 2T. The magnetic field is essentially perpendicular to the plane of the spectrometer. Figure 16 is a cartoon of the spectrometer in two different magnetic field settings ( $B_1$  and  $B_2$ ). Equal amounts of data are taken in each field setting. In field setting  $B_1$ , as shown in Figure 16 (b) the magnetic field is pointing inward in the positive-arm of the spectrometer and pointing out in the negative-arm of the spectrometer. Hence all the positive particle traversing the plane of the spectrometer bend in the backward (away from the positive z-axis) and negative particles bend in the forward (towards the positive z-axis) direction in both the arms due to the opposite

direction of the field. Similarly, positive particle traversing the plane of the spectrometer bend in the forward and negative particles bend in the backward direction in both the arms in the opposite field setting  $B_2$ .

Due to the asymmetric design of a given PHOBOS spectrometer arm about the y-axis, particles bending in forward direction have a different acceptance than the particles bending in backward direction. But for a given arm, all the particles bending forward (backward) direction in a given magnetic field setting will have the same acceptance as the oppositely charged particles bending in forward (backward) direction in the reversed magnetic field setting and they will also have the same tracking efficiency. Hence, calculating the raw ratios using unlike charged particles in a given arm but in opposite field settings will cancel the acceptance term in the numerator and denominator. In the following equations the positive and negative spectrometer arms are represented by  $arm_p$  and  $arm_n$  respectively. For the forward bending particles in  $arm_p$  Equation 4.6 can be written as,

$$\frac{\overline{P_{pri}}(B_2)}{\overline{P_{pri}}(B_1)}(arm_p) = \frac{\overline{C_{nonpri}^{pri}}(arm_p, B_2)}{C_{pri+nonpri}^{pri}(arm_p, B_1)} * \frac{\overline{C_{reco}^{pri+nonpri}}(arm_p, B_2)}{C_{reco}^{pri+nonpri}(arm_p, B_1)} * \frac{\overline{P_{reco}}(arm_p, B_2)}{P_{reco}(arm_p, B_1)} \quad (4.7)$$

Now from the above discussion,

$$\overline{C_{reco}^{pri+nonpri}}(arm_p, B_2) = C_{reco}^{pri+nonpri}(arm_p, B_1) \quad (4.8)$$



Hence, the ratios for a given arm and being direction can be obtained by using

$$\frac{\overline{P_{pri}(B_2)}}{\overline{P_{pri}(B_1)}}(arm_p) = \frac{\overline{C_{pri+nonpri}^{pri}(arm_p, B_2)}}{\overline{C_{pri+nonpri}^{pri}(arm_p, B_1)}} * \frac{\overline{P_{reco}(arm_p, B_2)}}{\overline{P_{reco}(arm_p, B_1)}} \quad (4.9)$$

Similarly, backward bending particles in  $arm_p$

$$\frac{\overline{P_{pri}(B_1)}}{\overline{P_{pri}(B_2)}}(arm_p) = \frac{\overline{C_{pri+nonpri}^{pri}(arm_p, B_1)}}{\overline{C_{pri+nonpri}^{prim}(arm_p, B_2)}} * \frac{\overline{P_{reco}(arm_p, B_1)}}{\overline{P_{reco}(arm_p, B_2)}} \quad (4.10)$$

For the other arm, equations similar to Equation 4.9 and Equation 4.10 can be obtained.

$$\frac{\overline{P_{pri}(B_2)}}{\overline{P_{pri}(B_1)}}(arm_n) = \frac{\overline{C_{pri+nonpri}^{pri}(arm_n, B_2)}}{\overline{C_{pri+nonpri}^{pri}(arm_n, B_1)}} * \frac{\overline{P_{reco}(arm_n, B_2)}}{\overline{P_{reco}(arm_n, B_1)}} \quad (4.11)$$

Similarly, backward bending particles in  $arm_p$

$$\frac{\overline{P_{pri}(B_1)}}{\overline{P_{pri}(B_2)}}(arm_n) = \frac{\overline{C_{pri+nonpri}^{pri}(arm_n, B_1)}}{\overline{C_{pri+nonpri}^{pri}(arm_n, B_2)}} * \frac{\overline{P_{reco}(arm_n, B_1)}}{\overline{P_{reco}(arm_n, B_2)}} \quad (4.12)$$

The ratio of the reconstructed anti-particles to particles is called the raw ratios. Raw ratios are also the measured ratios. After applying the non-primary corrections, ratio of the primary anti-particle to particles is obtained and its called the corrected ratios. As there are two arms and two magnetic field settings, four different sets of corrected ratios are obtained. The final ratios are an average (weighted using their statcal and systematic errors) over all these four obtained ratios.

$$\begin{aligned}
Final\ Ratios = & W(arm_p, B_2, B_1) * \frac{\overline{P_{pri}(B_2)}}{\overline{P_{pri}(B_1)}}(arm_p) + \\
& W(arm_p, B_1, B_2) * \frac{\overline{P_{pri}(B_1)}}{\overline{P_{pri}(B_2)}}(arm_p) + \\
& W(arm_n, B_2, B_1) * \frac{\overline{P_{pri}(B_2)}}{\overline{P_{pri}(B_1)}}(arm_n) + \\
& W(arm_n, B_1, B_2) * \frac{\overline{P_{pri}(B_1)}}{\overline{P_{pri}(B_2)}}(arm_n)
\end{aligned}$$

Where W is the weight and satisfies

$$W(arm_p, B_2, B_1) + W(arm_p, B_1, B_2) + W(arm_n, B_2, B_1) + W(arm_n, B_1, B_2) = 1 \quad (4.13)$$

Details of how the weight is obtained is given in the chapter 9. Step by step description of analysis follows the rest of this chapter.

### Analysis steps

In Figure 17 shows the flow diagram of analysis.

### Data quality Studies

The data for this analysis has been recorded over a period of few couple of months. The conditions under which the data is recorded do not remain the same. The analysis is performed over a few millions of events. Hence, it is not possible to pick every event and study its conditions in order to determine weather to keep the event for the analysis. Instead statistical methods are employed where an average quantity over a run is determined. And a decision

is made about using the run depending on the average value. Details are given in chapter 5. Essential at the end of this module, a subset of the total data set is obtained, which has fairly consistent behavior, for further analysis.

### **Particle identification and raw ratios determination**

Protons, kaon and pions are the three particles that can be fairly easily identified using the PHOBOS detector using the momentum of the reconstructed tracks and energy deposited. Particles identification cuts are first determined. These cuts are then used to obtain the raw ratios as a function of centrality and momentum. Details about the particle identification and raw ratio determination are given in chapter 6.

### **Corrections**

As described in subsection 4, there is no acceptance correction in determination of ratios. There still are some detector effects like absorption mainly in the beam pipe, secondary production due to interaction with the detector material and the feed-down from the heavier particles that modify the yield differently for particles and anti-particles. Obtaining these corrections are described in the chapter 7.

### **Systematic studies**

Systematic studies are given in the chapter 8.

### **Ratios**

The final ratios obtained by combining the raw ratios and corrections. The final ratios with the systematic errors are given in the chapter 9.

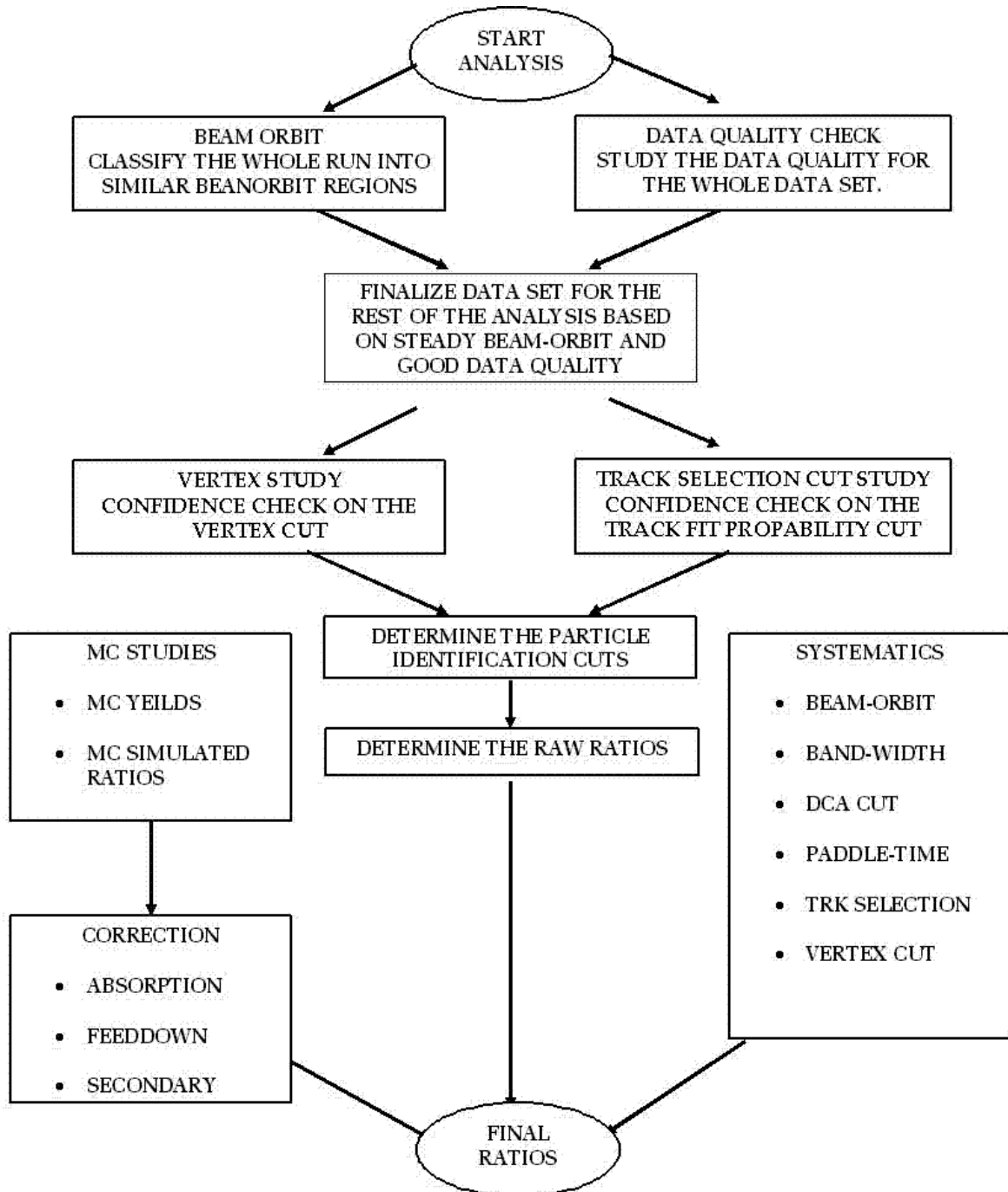


Figure 17. Flow diagram of the analysis.

## CHAPTER 5

### DATA QUALITY STUDIES

The quality of the data recorded over a period is defined by its “consistency” as a function of time. The inconsistencies can be caused due to change in

- Beam parameters : the position of the beam, pileup, undesired radiation due to the very high luminosity, undesired background, etc.
- Detector effects : change in detector response for various reasons including the life time of the detector, radiation damage, etc.

Monitoring of the data quality is done both online as well studied off-line (which will be described later in this chapter). The monitoring of the online data quality, which mainly focuses on the beam parameters is fed back to the RHIC operators to try and correct for them in the next store. The off-line studies performed are more detailed with an eventual goal of obtaining a subset of the data recorded which is consistent and usable for physics analysis.

The “consistency” is itself a multi-dimensional variable. It mainly involves the study of the average value of signals in the paddle trigger detectors, reconstructed vertex position, reconstructed track momentum etc. The following two sections contain a study of these variables in two logical steps. In the first step, Beam-orbit studies, data is broadly classified in to different subgroups depending on the  $\langle x \rangle$  and  $\langle y \rangle$  positions of the reconstructed events. In the second

step, run average data quality studies, within each of the subsets defined from the previous step run averages are studied.

## 5.1 Beam-orbit Studies

### Definition of beam-orbit

Average of x and y collision interaction points over a stable period, usually over a run, is called the beam-orbit.

### Details of the study

Track reconstruction efficiency in the spectrometer depends upon the collision interaction point, mainly on the x and y points. This is, as explained previously, because of the narrow  $\phi$  acceptance of the PHOBOS spectrometer. In this study data runs with similar beam-orbit values are broken-down into beam-orbit regions. Further data is analyzed within a chosen beam-orbit region. In Figure 18 the beam-orbit distribution for the complete Cu+Cu 200 GeV data recorded in the year 2005 is plotted as a function of run number, chronologically. The three grey bands (marked A, B & C) represent example beam-orbit regions, the subsets of data that are considered for further analysis.

This study aims not only at a steady beam-orbit value as function of time but also for different magnetic field settings. As shown in Figure 18 region A, data from different field settings are also compared. As explained in 4, the tracking efficiency of the negatively charged particles and the positively charged particles for a given arm and bending direction is assumed to be the same. Hence, the classification of the data in beam-orbit regions is important for this

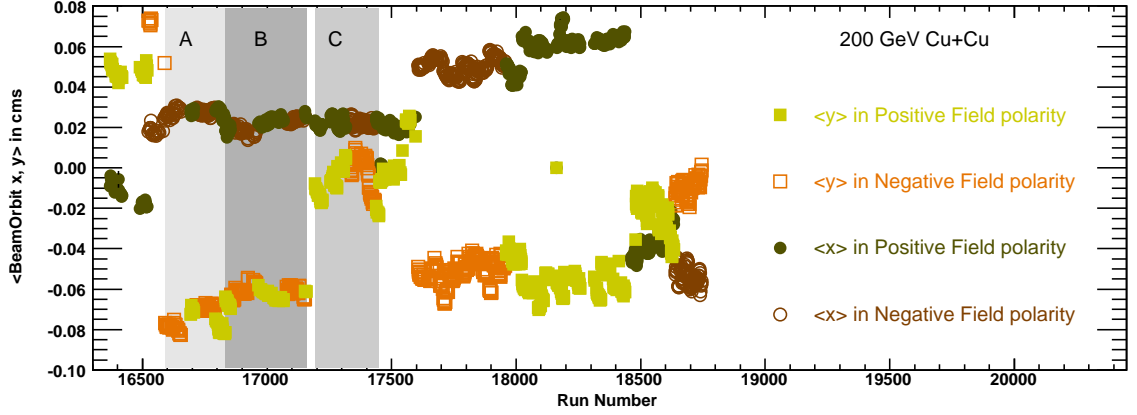


Figure 18. Beam-orbit  $\langle x \rangle$  and  $\langle y \rangle$  as a function of run number for Cu+Cu 200 GeV data. The three highlighted regions A, B and C represent steady beam-orbit regions.

analysis with an ultimate goal to arrive at one particular beam-orbit region to work with. The other beam-orbit regions are used for further systematic studies.

### Cu+Cu 200 GeV

The beam-orbit distribution of the Cu+Cu data and its classification is shown in Figure 18. All the three marked regions (A, B & C) have a steady beam-orbit distributions in addition to having sufficient statistics in both the polarities. All the data in a given beam-orbit region is of the same kind of hardware trigger. There is a jump in beam-orbit value  $y$  between the regions B and C. It was due to the T0 miss firing, which was diagnosed and corrected for. Comparing the values in the Table VII for different polarities for Cu+Cu 200 GeV data, it can be safely concluded that beam-orbit regions A & B have better agreement between different polarities compared to C. Beam-orbit region A has been chosen for the further studies. A detailed study

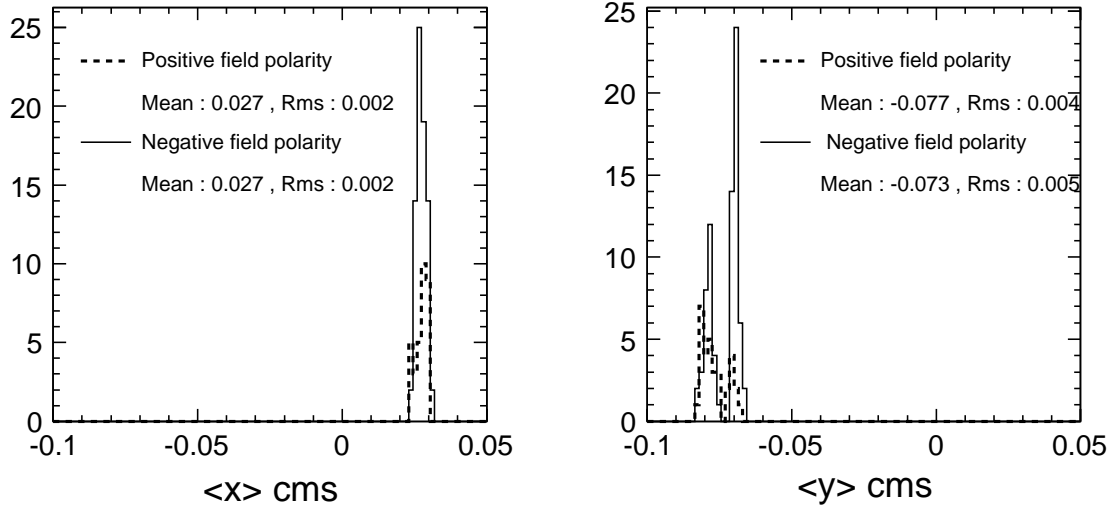


Figure 19. Detailed study of beam-orbit distribution for region - A (as shown in Figure 18) for 200 GeV Cu+Cu data. Right Panel is the  $\langle x \rangle$  distribution for different polarities. Left Panel is the  $\langle y \rangle$  distribution for different polarities.

of the beam-orbit region A is shown in Figure 19. The mean for  $\langle X \rangle$  is  $0.027 \pm 0.002$  cms in positive field polarity and  $0.027 \pm 0.002$  cms in negative polarity, and agree with in the errors. The mean for  $\langle y \rangle$  is  $-0.077 \pm 0.004$  cms in positive field polarity and  $-0.73 \pm 0.005$  cms in negative polarity, but agree with in the errors.



### Cu+Cu 62.4 GeV

Cu+Cu 62.4 GeV was a relatively short run lasting for a duration of 12 days and 110 million events on the tape. Figure 20 shows the beam-orbit distribution of the complete Cu+Cu 62.4 GeV data with projections given in Figure 21. Owing in large part to the short period of data taking, there are not too many jumps in the beam-orbit distribution. And due to fewer statistics compared to 200GeV Cu+Cu, all of the data is put under the same beam-orbit category. The systematic effect of beam-orbit variation is obtained from the Cu+Cu 200 GeV data studies.

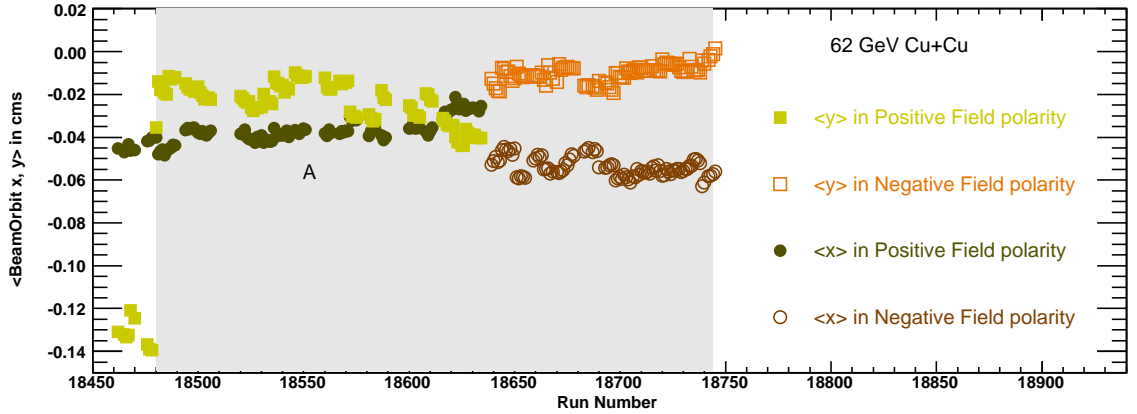


Figure 20. Beam-orbit  $\langle x \rangle$  and  $\langle y \rangle$  as a function of run number for Cu+Cu 62 GeV data. The highlighted region A is the only steady beam-orbit region for this data set.

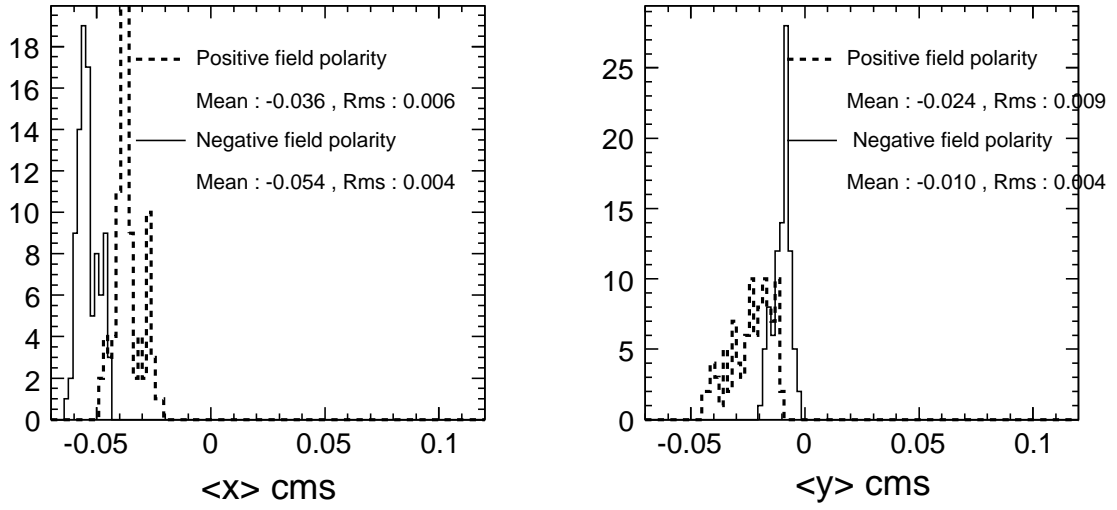


Figure 21. Detailed study of beam-orbit distribution for region - A (as shown in Figure 20). Right Panel is the  $\langle x \rangle$  distribution for different polarities for Cu+Cu 62.4 GeV data. Left Panel is the  $\langle y \rangle$  distribution for different polarities.

### Au+Au 200 GeV

Figure 22 shows the beam-orbit distribution as a function of run number for Au+Au 200 GeV data recorded in 2004 by the PHOBOS detector. During the early part of the running, there was a large shift in the beam-orbit as shown by the jump between the runs 13000 - 13400. Owing to the sensitivity of this analysis to the beam-orbit shifts, this early “unstable” data was not used for the analysis. The rest of the data is classified into 3 regions A, B and C as shown in the figure. Beam-orbit region B is chosen for the final analysis, due to its high statistics. A one-dimensional projection of the beam-orbit distribution in this region is shown in Figure 23. The mean  $x$  and  $y$  values for different magnetic field settings are in reasonable agreement with in the errors.

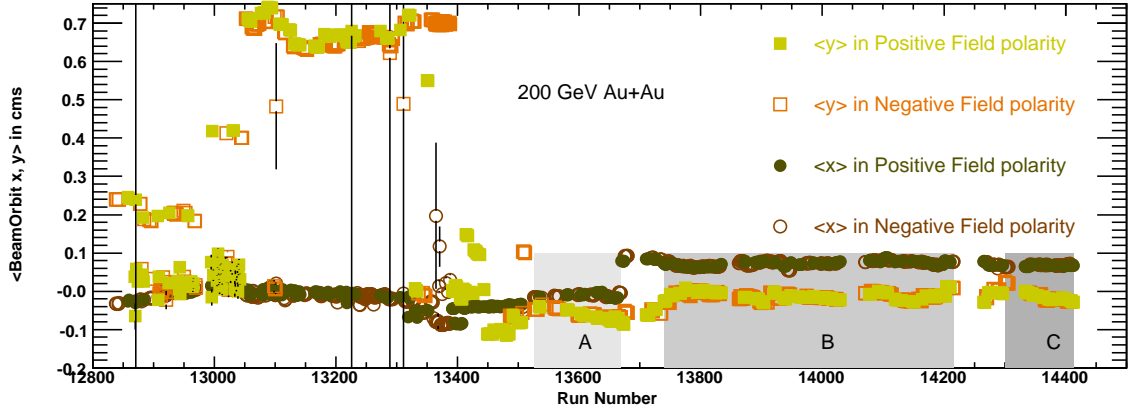


Figure 22. Beam-orbit  $\langle x \rangle$  and  $\langle y \rangle$  as a function of run number for Au+Au 200 GeV data. The three highlighted regions A, B and C represent steady beam-orbit regions.

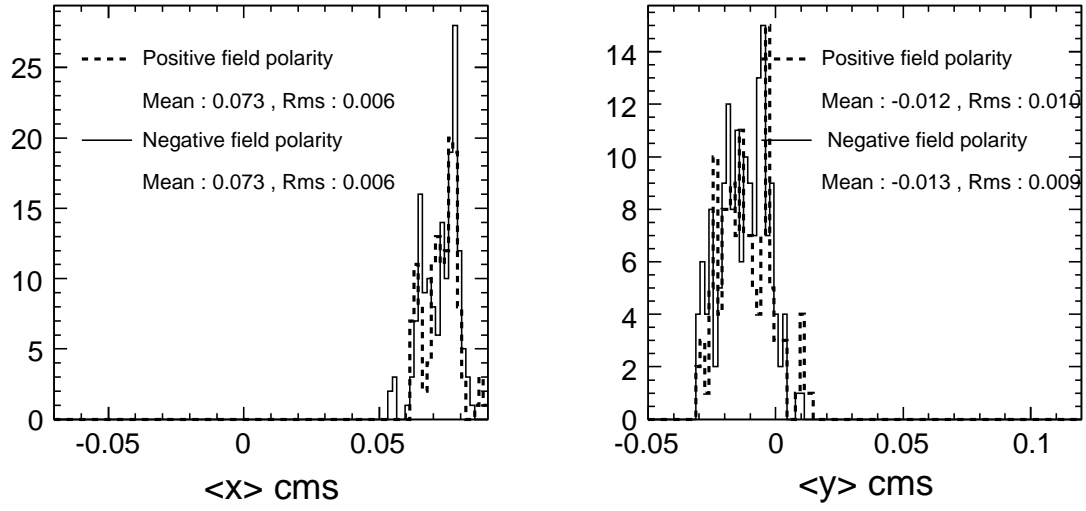


Figure 23. Detailed study of beam-orbit distribution for region - B (as shown in Figure 22). Right Panel is the  $\langle x \rangle$  distribution for different polarities for Au+Au 200 GeV data. Left Panel is the  $\langle y \rangle$  distribution for different polarities.

### Au+Au 62.4 GeV

Au+Au 62.4 GeV data is beam-orbit distribution as a function of run number is shown in Fig. Figure 24. Similar to Cu+Cu 62.4 GeV, this also was a short run. Hence the data is grouped into only one beam-orbit region. A one-dimensional projection of the distribution in this region is shown in Figure 25. Systematic effect of beam-orbit variation is obtained from the Au+Au 200 GeV data studies.

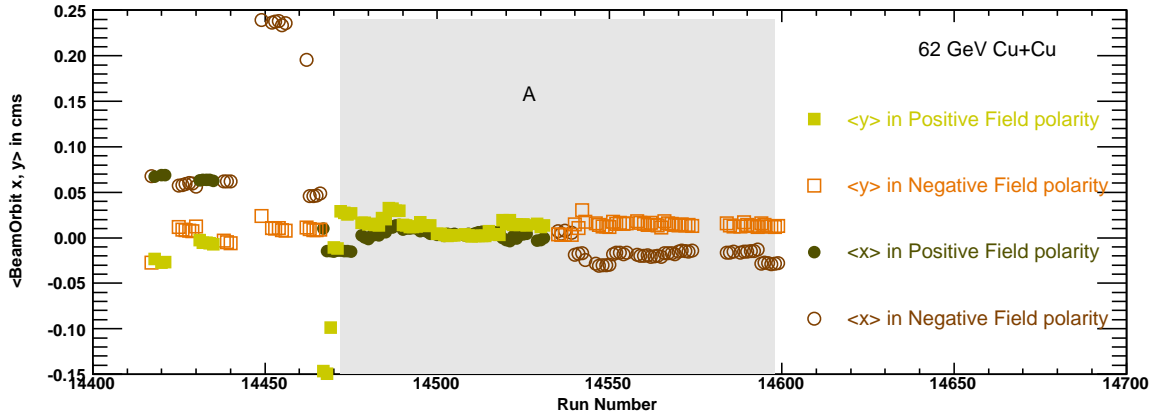


Figure 24. Beam-orbit  $\langle x \rangle$  and  $\langle y \rangle$  as a function of run number for Au+Au 62 GeV data. The three highlighted regions A is the only steady beam-orbit region for this data set.

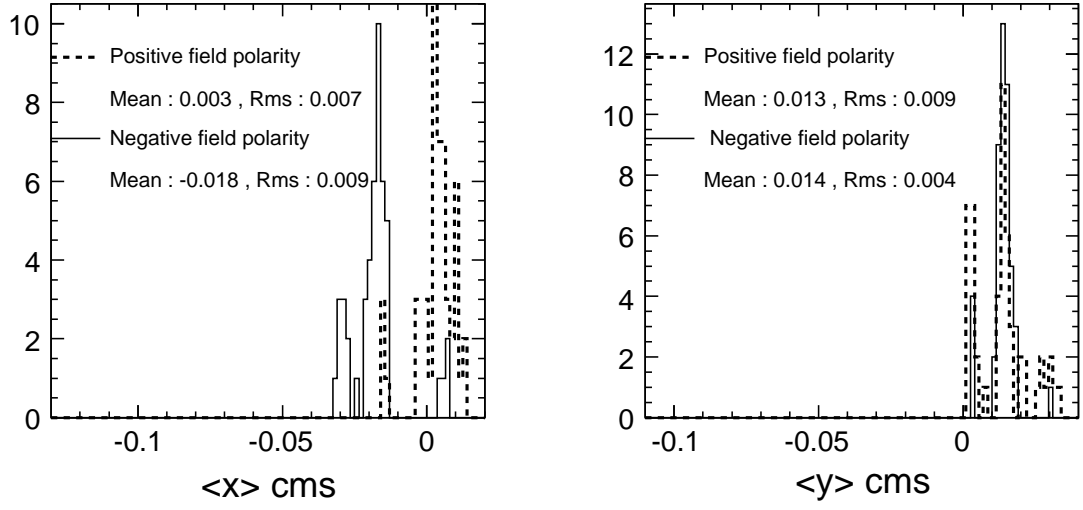


Figure 25. Detailed study of beam-orbit distribution for region - A (as shown in Figure 24) for Au+Au 62.4 GeV data. Right Panel is the  $\langle x \rangle$  distribution for different polarities. Left Panel is the  $\langle y \rangle$  distribution for different polarities.

TABLE VII. Given in the table is the summary of the beam-orbit study. Each sub-table corresponds to a combination of different energy and species. Each row in the sub-table corresponds to different beam-orbit region represented by the name and the run-range in the first column. Each entry corresponds to the mean $\pm$ rms of beam-orbit for that given run-range. Beam-orbit values for x and y and different polarities are given in different columns.

Beam-orbit	Negative - polarity		Positive - polarity	
	X (cms)	Y(cms)	X (cms)	Y(cms)
Cu+Cu 200 GeV				
A(16590-16831)	$0.027 \pm 0.002$	$-0.077 \pm 0.004$	$0.027 \pm 0.002$	$-0.073 \pm 0.004$
B(16833-17158)	$0.021 \pm 0.003$	$-0.061 \pm 0.002$	$0.022 \pm 0.003$	$-0.064 \pm 0.002$
C(17193-17450)	$0.022 \pm 0.002$	$-0.010 \pm 0.008$	$0.022 \pm 0.002$	$-0.008 \pm 0.007$
Cu+Cu 62.4 GeV				
A(18480-18744)	$-0.054 \pm 0.004$	$-0.010 \pm 0.004$	$-0.036 \pm 0.006$	$-0.024 \pm 0.009$
Au+Au 200 GeV				
A(13526-13688)	$-0.012 \pm 0.004$	$-0.045 \pm 0.003$	$-0.011 \pm 0.006$	$-0.046 \pm 0.004$
B(13739-14216)	$0.073 \pm 0.006$	$-0.013 \pm 0.009$	$0.073 \pm 0.006$	$-0.012 \pm 0.010$
B(14300-14412)	$0.068 \pm 0.002$	$-0.011 \pm 0.017$	$0.067 \pm 0.002$	$-0.015 \pm 0.008$
Au+Au 62.4 GeV				
A(14472-14598)	$-0.018 \pm 0.009$	$0.014 \pm 0.004$	$0.003 \pm 0.007$	$0.013 \pm 0.009$

## 5.2 Run average data quality studies

As the name suggests, in this study run based average of the following variables is calculated for all the runs in a given beam-orbit region (subsection 5.1).

- number of tracks per event.
- paddle hits per event.
- reconstructed track vertex.
- difference between reconstructed track vertex and the event vertex.
- difference between the SpecVtxPN (subsection 3.6) and the beam-orbit X.
- difference between the ZVertex (subsection 3.6) and the beam-orbit Y.

To determine if a particular run is deviating from the normal behavior, first the mean and RMS ( $\sigma$ ) over all the runs is obtained. This mean is determined separately for all the above listed variables. Even for a given variable, an independent study is performed for different combinations of spectrometer arms, polarity of the magnetic field, and particle charge sign. List of all the runs with average values lying outside of the  $\pm 3\sigma$  of the mean is determined. These runs are later excluded from the final analysis. The motivation for the previous step is to remove runs where beam or detector conditions are not ideal or consistent with the rest of runs. In this section the detailed study of only the first three variables from the above list is presented, as the intention is only to elaborate the technique. In the same spirit, the conclusions made are also quite qualitative. The summary of all the deviant runs is presented in Table IX in section 5.2 obtained using all the variable from the list.



### General description of the plots in this section

The following Figure 27 - Figure 34 have four panels each (they are named using roman numerals on upper left corner). There are two differently colored graphs in each panel represent two different spectrometer arms. Panel (I) and panel (IV) both correspond to the forward bending tracks for different sign charge and magnetic field while panel (II) and panel (III) correspond to the backward bending tracks. Figure 35 - Figure 38 have two panels each, one for each polarity. Similar to the previous set of plots, differently colored graphs in each panel represent two different spectrometer arms. Figure 39 - Figure 42 also have two panels each corresponding to two different polarity settings of the data. For this set of plots though, there is only one plot in a given panel as there is no possibility to further sub-divide them in to separate arms.

Distributions are represented using a solid line. The  $\pm 3\sigma$  region of the distribution is represented by the shaded region. The unshaded region out-side of the  $\pm 3\sigma$  corresponds to all the runs that are named deviant and are not included in the final analysis. In the major part of the rest of this section observations about all of the above mentioned distributions, made to arrive at the deviant runs, will be highlighted. These studies are more qualitative in nature, as the results from this section don't effect the analysis directly instead contribute toward the final systematic studies.

### Average number of track studies

In this section a detailed study of the average number of tracks reconstructed is presented. Figure 27, Figure 28, Figure 29 and Figure 30 corresponding to the studies for Cu+Cu 200 GeV, Cu+Cu 62.4 GeV, Au+Au 200GeV and Au+Au 62.4 GeV respectively. Following listed are a few observations from the plots

- The average number of tracks produced is very sensitive to beam-orbit values. As shown in the Figure 26 using the data from Au+Au which has considerable shift in the beam-orbit  $\langle y \rangle$  value [ Figure 22]. Much more detailed study is not possible as the experiment does not allow you to control the value of beam-orbit. Despite of that fact the following conclusion can be made from the Figure 26; a change in couple of millimeters ( $\sim 2\text{mm}$ ) in the beam-orbit value affects the track reconstruction.
- Colliding system size : The average number of tracks reconstructed depends on the collision system size. For given colliding system center of mass energy the multiplicity of Au+Au system is higher than the Cu+Cu system hence the average number of tracks reconstructed is higher for Au+Au ( Figure 29 panel-I) compared to Cu+Cu ( Figure 27 panel-I).
- Colliding system energy : The average number of tracks reconstructed depends on collision center of mass energy. For a given system of colliding ions more particles are produced for higher collision center of mass energy, as there is more energy available to produce more particles. Comparing the different energies for Cu+Cu ( Figure 27, Figure 28) or

Au+Au ( Figure 29, Figure 30) there are more particles produced for 200 GeV collisions compared to 62.4 collisions.

- Bending direction : The forward bending tracks have more acceptance than the backward bending as demonstrated by the difference in the average values between panel-1 & IV and panel II & III all the four plots.
- Different spectrometer arms : There is a difference in the average number of reconstructed tracks in both the arms. The number of dead channels in the silicon of the spectrometer arms and the beam-orbit values are the two main contributing factors to this. In both Cu+Cu and Au+Au 200 GeV data one of the arm-2 is consistently lower than the arm-1. While in the Cu+Cu and Au+Au 62.4 GeV data, the behavior is different for the forward bending and the backward bending tracks. As the final ratios are obtained independently for the forward bending tracks and the backward bending tracks, a consistency within the forward and backward bending tracks for different arms is all that is required.

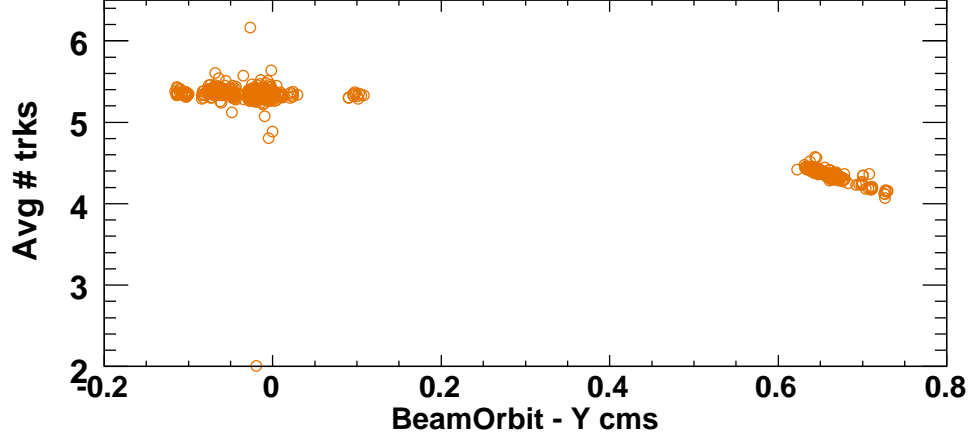


Figure 26. Average number of tracks per event as a function of beam-orbit Y in Au+Au 200 GeV data.

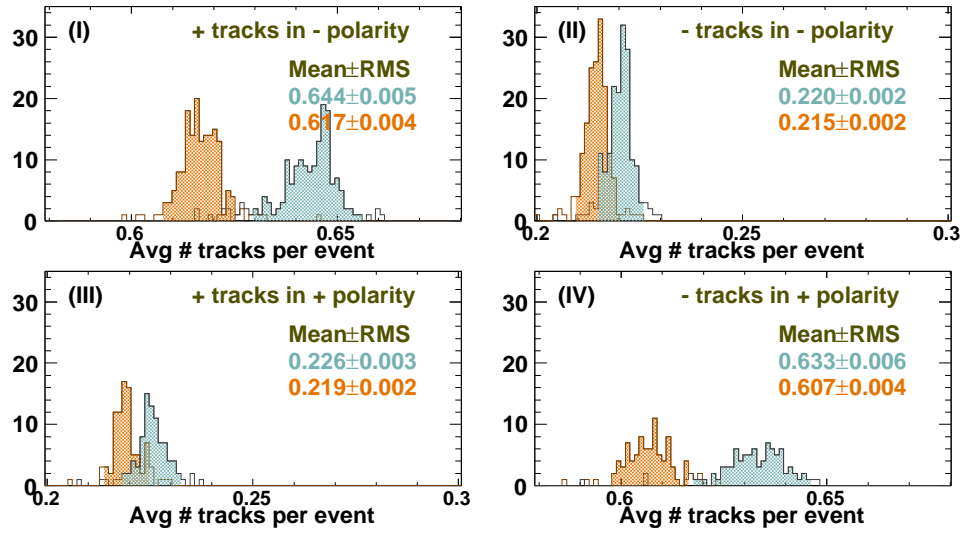


Figure 27. Average number of tracks per event in Cu+Cu 200 GeV data. Blue corresponds to arm -1 and orange corresponds to arm -2.

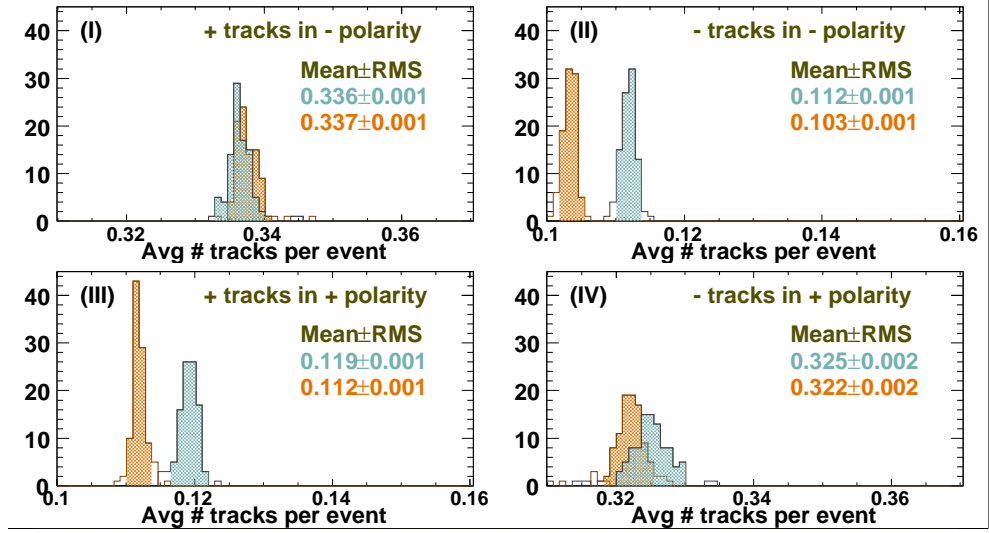


Figure 28. Average number of tracks per event in Cu+Cu 62.4 GeV data. Blue corresponds to arm -1 and orange corresponds to arm -2.

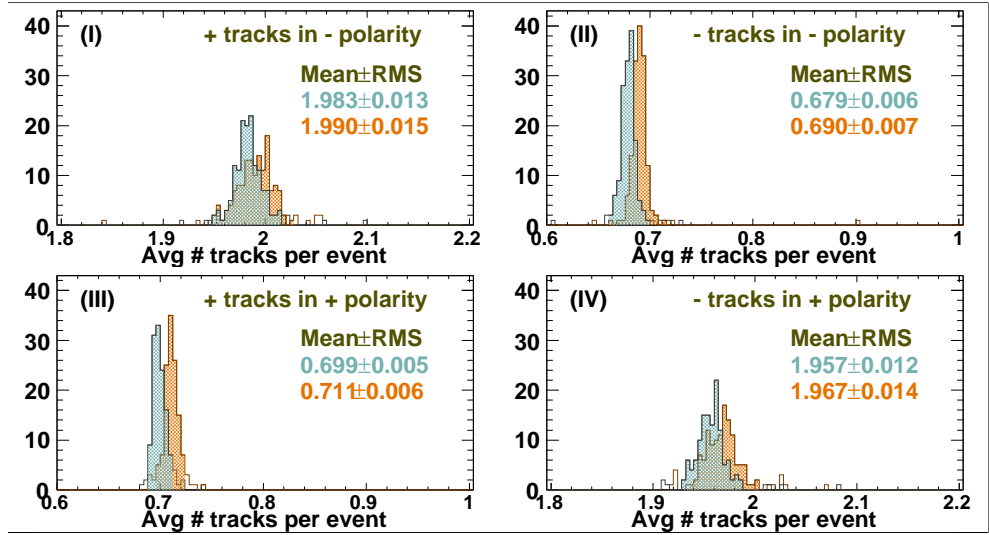


Figure 29. Average number of tracks per event in Au+Au 200 GeV data. Blue corresponds to arm -1 and orange corresponds to arm -2.

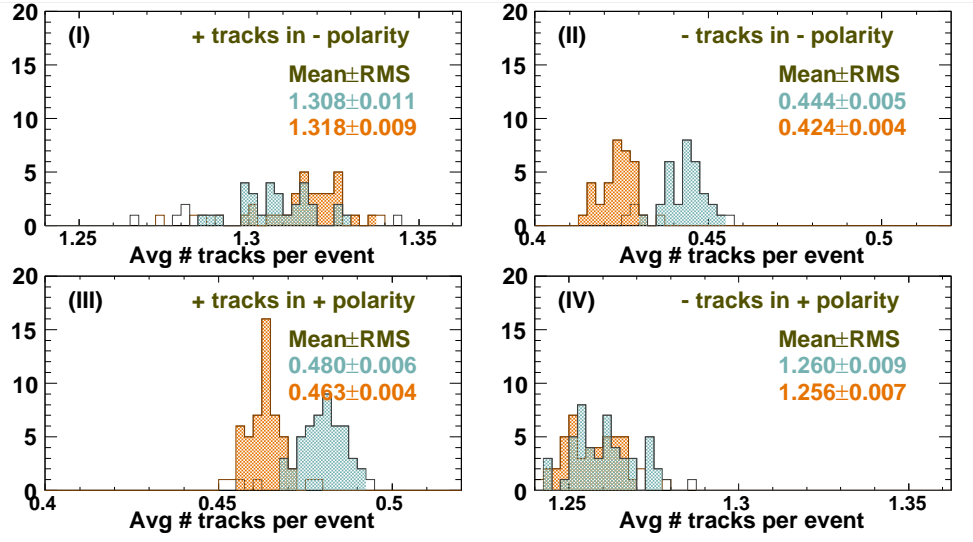


Figure 30. Average number of tracks per event in Au+Au 62.4 GeV data. Blue corresponds to arm -1 and orange corresponds to arm -2.

### Average reconstructed track momentum

In this section a detailed study of the average reconstructed track momentum is presented. Figure 31, Figure 32, Figure 33 and Figure 34 corresponding to the studies for Cu+Cu 200 GeV, Cu+Cu 62.4 GeV, Au+Au 200 GeV and Au+Au 62.4 GeV respectively. The study of the average number of tracks and the average momentum of the tracks is correlated to the first order. The study of the average momentum of the tracks has advantage precipitating the runs that end with a problem in the silicon of the tracker. Following are the few observations from the plots,

- Colliding system size : As the system size increases (for a given center of mass energy of the collisions) the number of binary collisions per event increases which in turn increases the total multiplicity. Naively one would expect the momentum spectrum to scale with the number of collisions or the number of participants or a combination of both. But studies have shown that there is suppression of the high transverse momentum particles which to first order scales with the size of the system (?). Hence, the difference in the average momentum of the reconstructed particles depends on the kinematic region of the detector. In the PHOBOS detector, the average average transverse momentum of the particles being reconstructed is higher for a larger system size. This is the same behavior for both the energies.
- Colliding system energy : Increase in the center of mass energy of the colliding system leads to harder collisions, hence more particles with higher momentum are produced. Comparing the Cu+Cu 200 GeV with Cu+Cu 62.4 GeV and Au+Au 200 GeV with

Au+Au 62.4 GeV, both cases 200 GeV collisions have higher average reconstructed transverse momentum.

- Different spectrometer arms : From the study of the mean value of the average track momentum, the arm-2 has a consistently lower than the arm-1 all but for the Au+Au 200 GeV data. To understand the reason behind this, a further re-analysis of the data set after applying the track selection cuts has been performed. The results are presented in the Table VIII. The Au+Au 200 GeV data behaves similar to the other data sets. Also, the runs that are selected to be deviant with and with out the track selections cuts are the same. Hence, no further re-analysis of the data is performed.

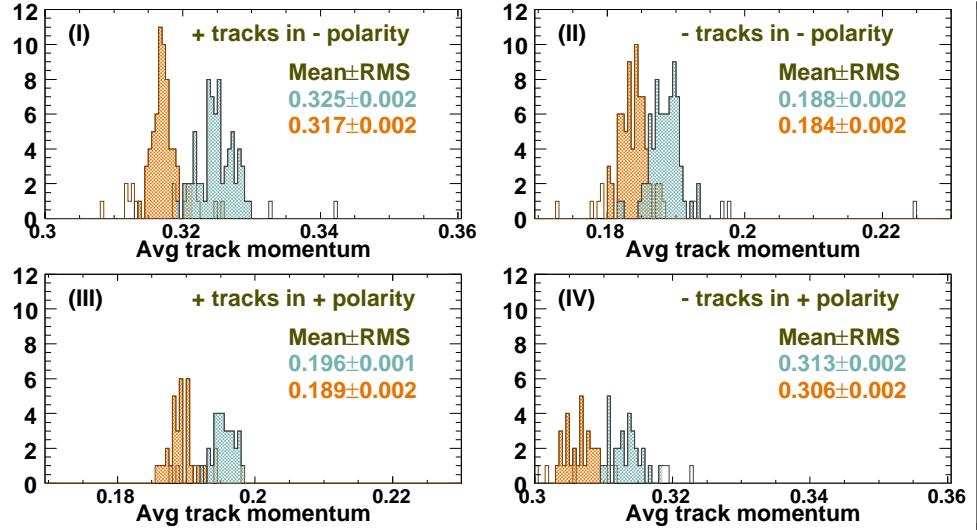


Figure 31. Average track momentum per event in Cu+Cu 200 GeV data. Blue corresponds to arm -1 and orange corresponds to arm -2.



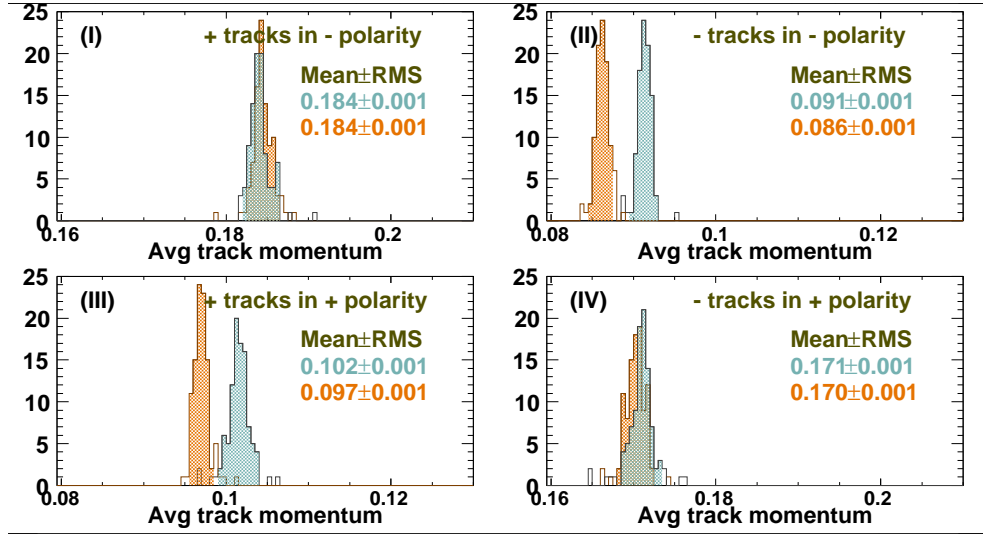


Figure 32. Average track momentum per event in Cu+Cu 62.4 GeV data. Blue corresponds to arm -1 and orange corresponds to arm -2.

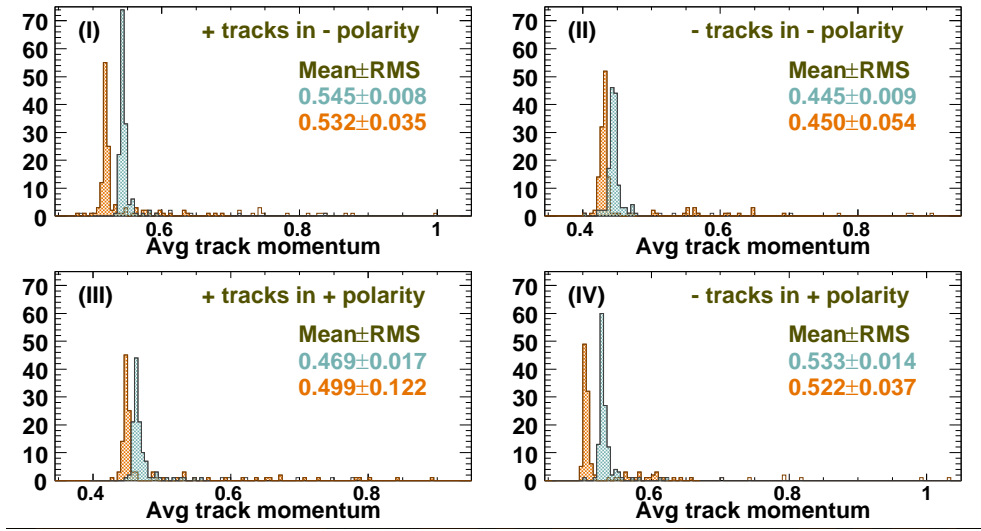


Figure 33. Average track momentum per event in Au+Au 200 GeV data. Blue corresponds to arm -1 and orange corresponds to arm -2.

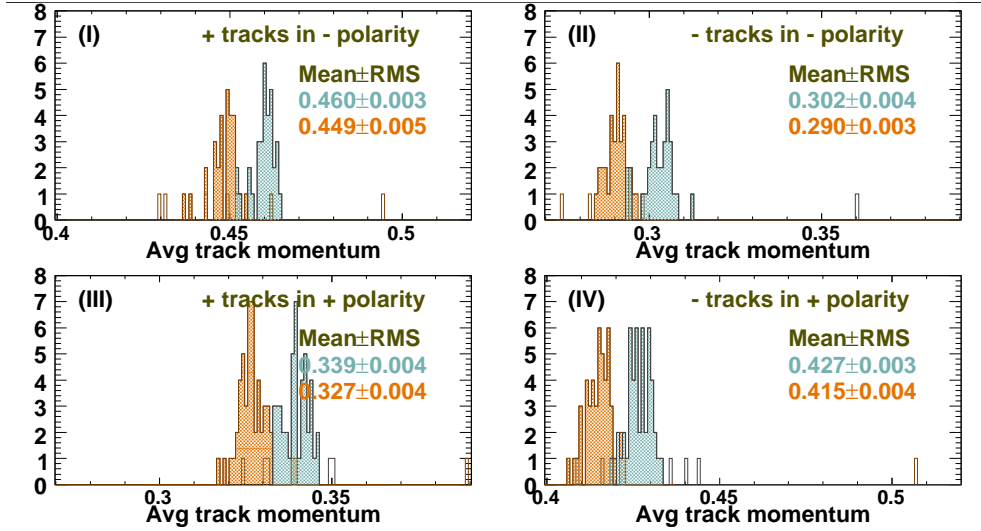


Figure 34. Average track momentum per event in Au+Au 62.4 GeV data. Blue corresponds to arm -1 and orange corresponds to arm -2.

TABLE VIII. Mean of the average momentum per run for different arms of the spectrometer is listed in the table. A comparison between arms is performed by taking the ratio for different combinations of bending directions and magnetic polarity.

Positive polarity						
	Forward Bending			Backward bending		
200 GeV	Arm - 1	Arm -2	Ratio	Arm -1	Arm -2	Ratio
Au+Au	0.533	0.522	1.02	0.469	0.499	0.94
Au+Au with track selection cuts	0.479	0.481	1.00	0.385	0.381	1.01
Cu+Cu	0.313	0.306	1.02	0.196	0.189	1.03
Negative Polarity						
	Forward Bending			Backward bending		
200 GeV	Arm - 1	Arm - 2	Ratio	Arm - 1	Arm - 2	Ratio
Au+Au	0.545	0.532	1.02	0.445	0.450	0.99
Au+Au with track selection cuts	0.493	0.495	0.99	0.371	0.367	1.01
Cu+Cu	0.325	0.317	1.03	0.188	0.184	1.02

### **Average reconstructed track distance of closest approach**

In this section a detailed study of the average reconstructed track distance of closest approach (DCA) is presented. Figure 35, Figure 36, Figure 37 and Figure 38 corresponding to the studies for Cu+Cu 200 GeV, Cu+Cu 62.4 GeV, Au+Au 200GeV and Au+Au 62.4 GeV respectively. Distance of closest approach is the length of the shortest line between the event vertex and the trajectory of the reconstructed track. The x and y co-ordinates of the event vertex are obtained from the beam-orbit for that run and the z-coordinate of the event vertex is obtained from the reconstructed vertex position of the event. The algorithm for the vertex reconstruction is different for Au+Au and Cu+Cu [3.6]. The mean value of the average DCA per event per run is the same with in the errors for both the Cu+Cu energies. While it seems to be different for different arms for both Au+Au energies. But the difference between them in the Au+Au data is of the order of a couple of millimeters, and lying outside the DCA cut applied for the analysis. Again as done previously, a re-analysis of the data as summarized in the data [table] Au+Au data looks much similar to the Cu+Cu data.

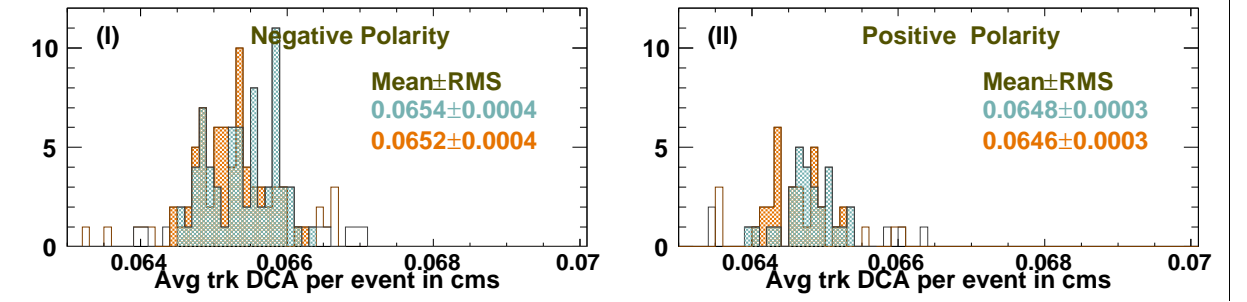


Figure 35. Average track distance of closest approach per event in Cu+Cu 200 GeV data.  
Blue corresponds to arm -1 and orange corresponds to arm -2.

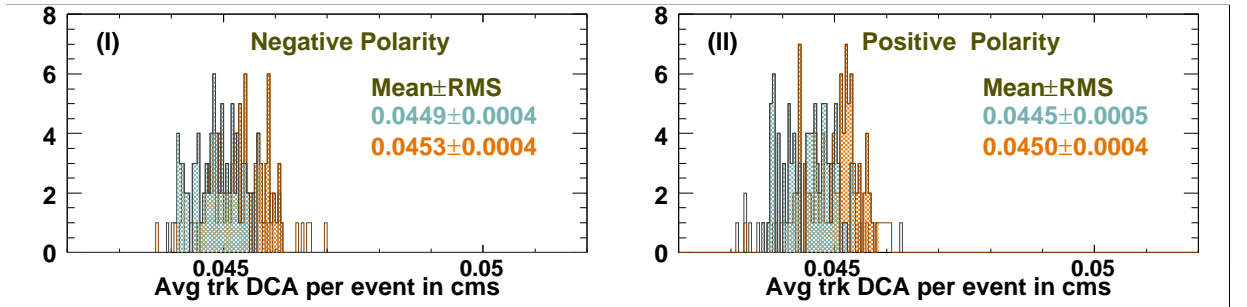


Figure 36. Average track distance of closest approach per event in Cu+Cu 62.4 GeV data.  
Blue corresponds to arm -1 and orange corresponds to arm -2.

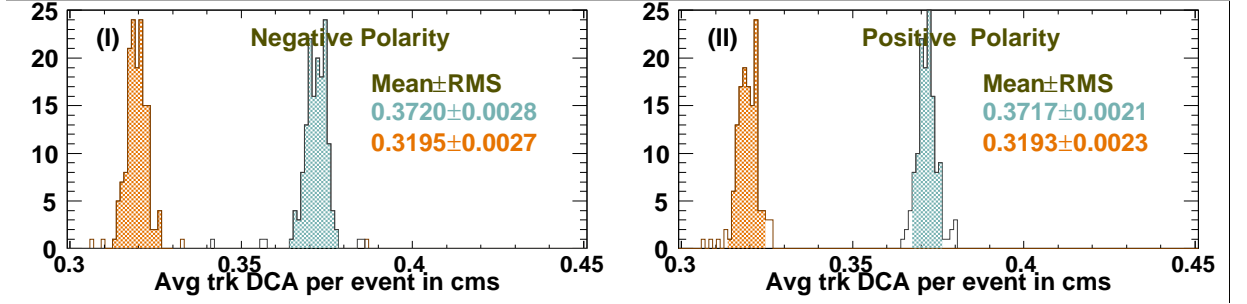


Figure 37. Average track distance of closest approach per event in Au+Au 200 GeV data.  
Blue corresponds to arm -1 and orange corresponds to arm -2.

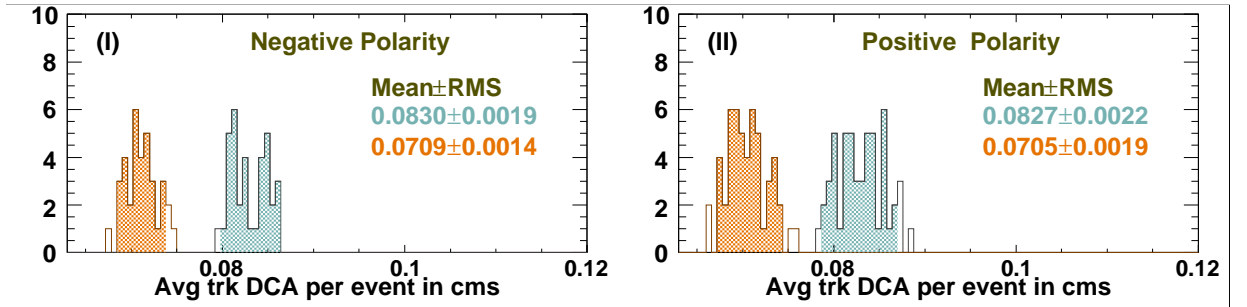


Figure 38. Average track distance of closest approach per event in Au+Au 62.4 GeV data.  
Blue corresponds to arm -1 and orange corresponds to arm -2.

### Average of the total signal in the paddles

In this section a detailed study of the average of the total signal in the paddles is presented. Figure 39, Figure 40, Figure 39 and Figure 40 corresponding to the studies for Cu+Cu 200 GeV, Cu+Cu 62.4 GeV, Au+Au 200GeV and Au+Au 62.4 GeV respectively. The average hits in the paddle scales with multiplicity. Hence, just like the average number of tracks, bigger the colliding system or more the colliding energy there is more signal in the paddle. Average signal in the paddles is sensitive to the pileup events [needs reference, probably Ian's thesis]. Hence, the runs that make it to the deviant run list using that study are mostly the runs with higher percentage of pile up in them.

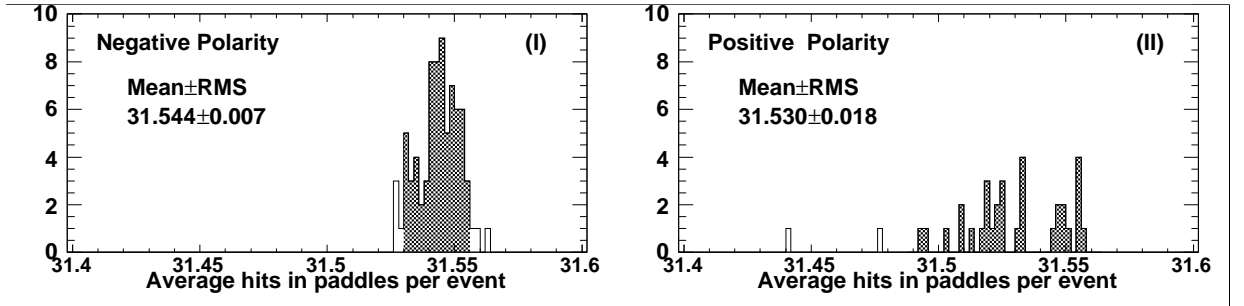


Figure 39. Average track distance of closest approach per event in Cu+Cu 200 GeV data.

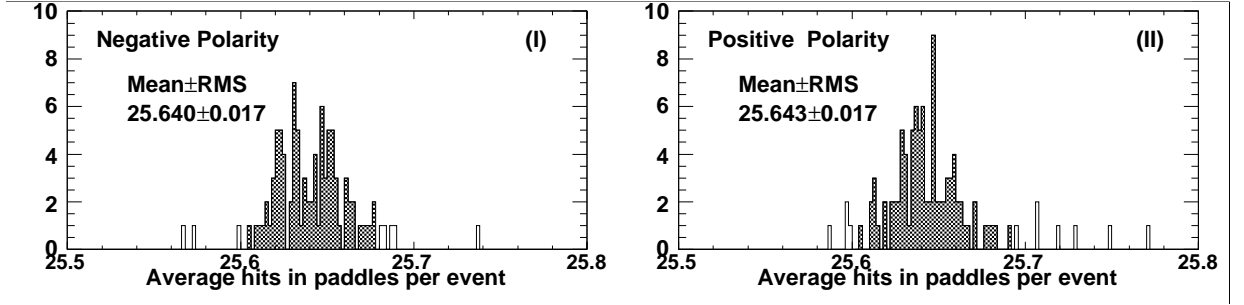


Figure 40. Average track distance of closest approach per event in Cu+Cu 62.4 GeV data.

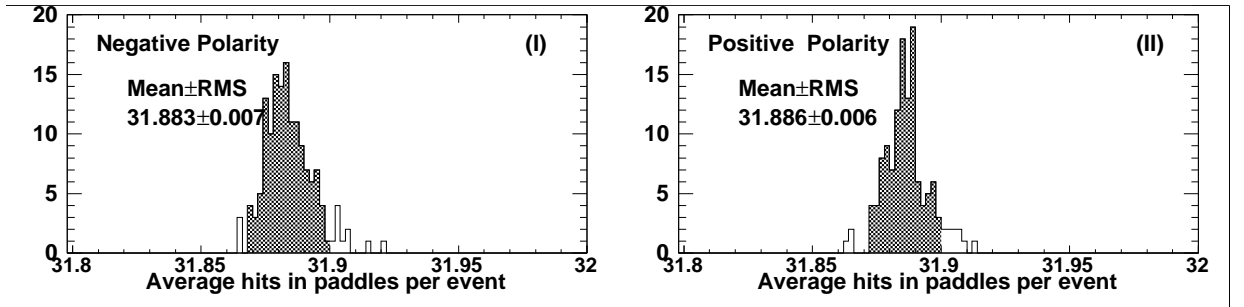


Figure 41. Average track distance of closest approach per event in Au+Au 200 GeV data.

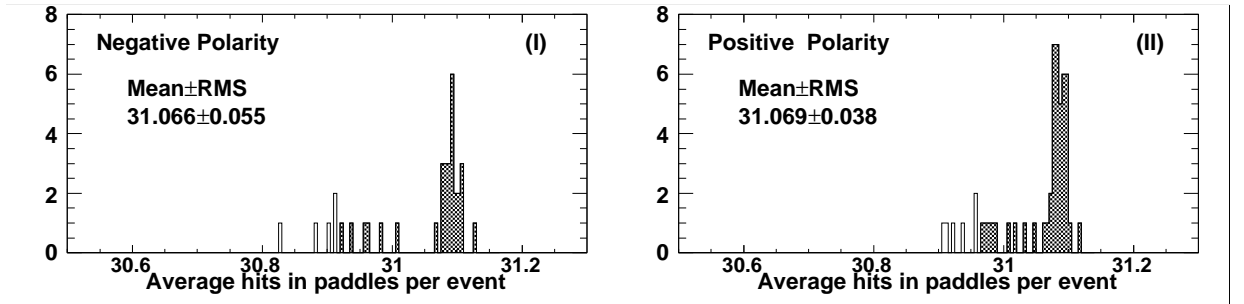


Figure 42. Average track distance of closest approach per event in Au+Au 62.4 GeV data.



### Deviant runs

TABLE IX

FOLLOWING IS THE LIST OF THE SUMMARY OF DEVIANT RUNS (WITH IN THE CHOSEN BEAM-ORBIT REGION FROM THE PREVIOUS SECTION) THAT HAVE NOT BEEN INCLUDED IN THE FINAL ANALYSIS. DIFFERENT ROWS CORRESPOND TO DIFFERENT COLLIDING SYSTEMS. RUNS WITH NEGATIVE AND POSITIVE POLARITY HAVE BEEN GROUPED SEPARATELY IN COLUMNS.

Colliding System	Deviant Runs							
	Negative Polarity				Positive Polarity			
Cu+Cu 200 GeV	16599	16600	16601	16608	16694	16700	16803	16807
	16622	16639	16739	16746	16809	16813	16820	16823
	16785	16786			16826			
Cu+Cu 62.4 GeV	18650	18674	18676	18684	18521	18527	18533	18534
	18690	18693	18708	18731	18536	18538	18539	18546
	18734	18735	18736	18737	18551	18569	18575	18604
Au+Au 200 GeV					18605	18608	18630	
	13740	13750	13751	13784	13744	13758	13779	13788
	13795	13796	13799	13807	13789	13800	13811	13828
	13823	13824	13893	13921	13865	13869	13896	13898
	13937	13938	13949	13963	13926	13978	14024	14083
	14004	14029	14077	14095	14084	14085	14099	14109
	14106	14127	14150	14185	14147	14157	14169	14183
Au+Au 62.4 GeV	14194	14195	14207		14187	14215		
	14479	14485	14487	14488	14536	14540	14541	14542
	14496	14497	14502	14508	14552	14565	14570	14571
	14512	14517	14523					

A list of the deviant runs is given in the 5.2. With an intension to understand if there are any common trends to the deviant runs, following is list is the summary of the entries from looking up the log-book entries 3.3 of these runs.

- About 40% of those runs have less than 15 sequences and ended up with Latchup.
- About 20% of them were terminated due to DAQ problems.
- About 20% of them were terminated under some abnormal conditions.
- About 20% of them have a high pileup, which is an indicative of the high luminosity conditions.

Runs listed as deviant, as explained before, are not included in the final analysis. A systematic study of the final ratios is preformed by doing the analysis by including these runs.

## CHAPTER 6

### PARTICLE IDENTIFICATION AND RAW RATIOS

Raw ratios [4] are obtained by counting the identified particles. The first half of this chapter deals with particle identification techniques. In the later half of this chapter are presented the raw ratios.

#### 6.1 Particle Identification

The particle identification (PID) uses the tracking (chapter ??) and energy information from the Spectrometer. In Figure 43 the momentum of the reconstructed particles (section ??) is plotted versus the truncated mean of the energy deposited by the particles (chapter ??) in the silicon of the detector. Due to different energy deposition characteristics of different particles results in separation of these particles into bands as function of the momentum. These bands can be characterized by the Bethe-Bloch function, which will be elaborated in the next section followed by different techniques to separate these bands.

#### **Bethe-Bloch formula**

Bethe-Bloch function ( Equation 6.1) characterizes the mean energy deposited by swift charged particles inside a material due to electromagnetic interactions, mainly the ionization of the electrons inside the material. Detailed derivation is given (19) and (20). Electrons present in the material can take up significant amount of energy from the fast moving particles causing only slight change to the moving particles trajectory, hence leading to their ionization. Nuclei

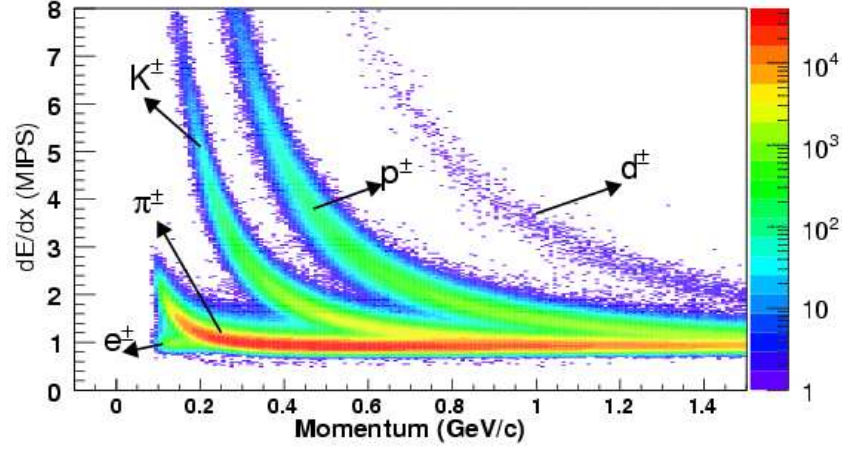


Figure 43. Momentum (GeV/c) on the x-axis and truncated mean of the energy deposited in the silicon of the spectrometer layers (MIPS) on the y-axis for Cu+Cu 200 GeV data for both positive and negatively charged particles.

in the material (massive compared to the electrons) scatter the fast moving particles through small angles, without absorbing too much energy.

$$-\frac{dE}{dx} = 2\pi N_a r_e^2 m_e c^2 \rho \frac{Z}{A} \frac{z^2}{\beta^2} \left[ \ln \left( \frac{2m_e c^2 \gamma^2 \beta^2 T_{max}}{I^2} \right) - 2\beta^2 - \delta - 2 \frac{C}{Z} \right], \quad (6.1)$$

$N_a$  = Avogadro's number ( $6.022 \times 10^{23} \text{ mol}^{-1}$ )

$r_e$  = electron radius ( $2.817 \times 10^{-13} \text{ cm}$ )

$m_e$  = electron mass ( $511 \text{ keV}$ )

$\rho$  = absorber density ( $2.33 \text{ g/cm}^2 \text{ for Si}$ )

$$\begin{aligned}
Z &= \text{absorber atomic number (14 for Si)} \\
A &= \text{absorber atomic weight (28.09 g/mol for Si)} \\
z &= \text{incident particle charge}(\pm 1) \\
\beta &= \text{incident particle velocity divided by the speed of light} \\
\gamma &= 1/\sqrt{1-\beta^2} \text{ unit less} \\
T_{max} &= \frac{2m_e c^2 \beta^2 \gamma^2}{1 + 2\gamma \frac{m_e}{M} + \frac{m_e^2}{M^2}} \simeq 2m_e c^2 \beta^2 \gamma^2. \\
M &= \text{incident particle mass (keV)} \\
I &= \text{absorber mean excitation potential (173 eV for Si)} \\
\delta &= \text{density correction} \\
C &= \text{shell correction}
\end{aligned} \tag{6.2}$$

The amount of kinetic energy lost by any incident particle per unit length of the path traversed in the medium is given by Equation 6.1 and has the following properties,

- It is inversely proportional to the velocity of the particles.
- When measured as  $\text{MeV cm}^2/\text{g}$ , the energy depends solely on the  $Z/A$  of the material.
- $T_{max}$  is the maximum kinetic energy transferred to an electron. It rises with  $\gamma^2$ . This gives rise to the relativistic rise [Figure 44] at high momentum.
- Bethe-Bloch equation provides only the mean of the “stopping power”, but no information on fluctuations in it. Fluctuations are the maximum for very thin layers.

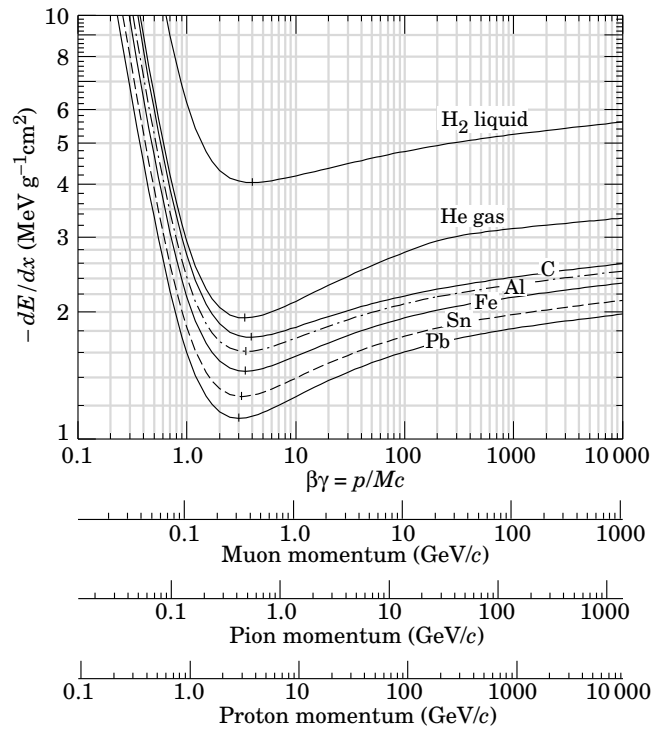


Figure 44. Plot from the particle data group (21) demonstrating the relativistic rise. Mean energy loss rate in liquid (bubble chamber) hydrogen, gaseous helium, carbon, aluminum, iron, tin, and lead.

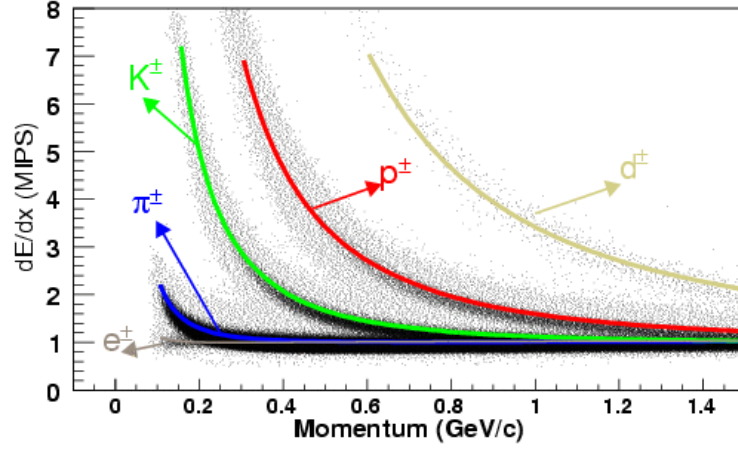


Figure 45. Momentum (GeV/c) on the x-axis and truncated mean of the energy deposited in the silicon of the spectrometer layers (MIPS) on the y-axis. Cu+Cu 200 GeV data is represented in black marker. The bands obtained from Bethe-Bloch function are overlaid on the data for different particles represented in different colors.

- The density correction arises from the screening of remote electrons by close electrons, which results in a reduction of energy loss for higher energies (transverse electric field grows with  $\gamma$ ). The effect is largest in dense matter, i.e. in solids and liquids.
- Shell correction is only important for low energies where the particle velocity has the same order of magnitude as the “velocity” of the atomic electrons. This essentially can be interpreted as a correction to Bethe-Bloch function when the assumption that target electrons are stationary is no longer valid.

The silicon layers in the PHOBOS Spectrometer [3.2.1] are very thin, hence their energy loss distribution is a Landau distribution [??]. For improved accuracy to match the experimental data additional correction factors need to be added. Hence a modification to the Bethe-Bloch

function is utilized to incorporate this effect. An upper limit to the energy loss is determined and all the particles with energy loss more than upper limit are neglected. The modified formula is given in Equation 6.3. This leads to flattening of the Bethe-Bloch function as shown in Figure 45.

$$-\frac{dE}{dx} = 2\pi N_a r_e^2 m_e c^2 \rho \frac{Z}{A} \frac{z^2}{\beta^2} \left[ \ln \left( \frac{2m_e c^2 \gamma^2 \beta^2 T_{upper}}{I^2} \right) - \left( 1 + \frac{T_{upper}}{T_{max}} \right) \beta^2 - \delta - 2\frac{C}{Z} \right] \quad (6.3)$$

The following subsections has two different particle identification techniques outlined. The first technique makes use of the Bethe-Bloch function. Second technique is much more statistical in nature.



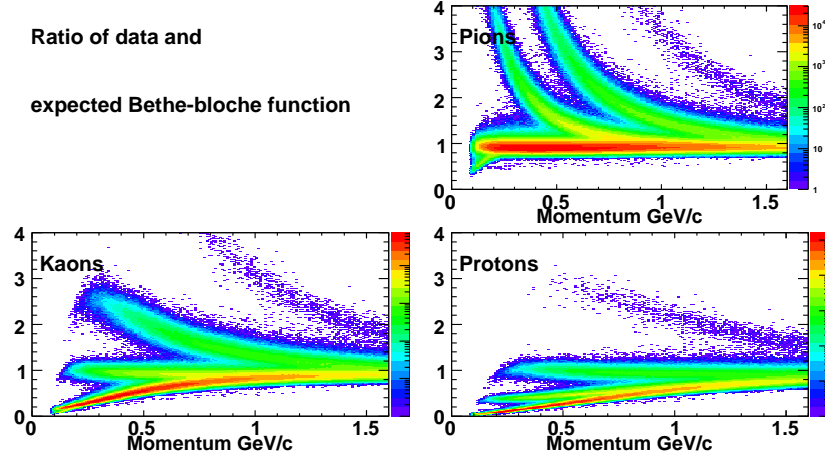


Figure 46.

### Method - 1

The basic idea behind this method is to obtain a correction to the theoretical prediction of the Bethe-Bloch function and hence is called the ‘Corrected Bethe-Bloch’ function technique. The Bethe-Bloch function [Equation 6.3] gives an approximate theoretical description of the data, an additional correction function is used to provide a better description of the data. To obtain this correction function, the measured  $dE/dx$  ( Figure 43) is divided by the expected value from the Bethe-Bloch function. As the Bethe-Bloch function gives a different line for protons, kaons and pions, there are three different correction functions ( Figure 46) obtained. An approximately linear distribution of the particle band, which is now centered around 1 on the y-axis is obtained for all the three particles. For every particles, the mean value of particle band is extracted ( Figure 47). The mean values function is fit with a sixth order polynomial

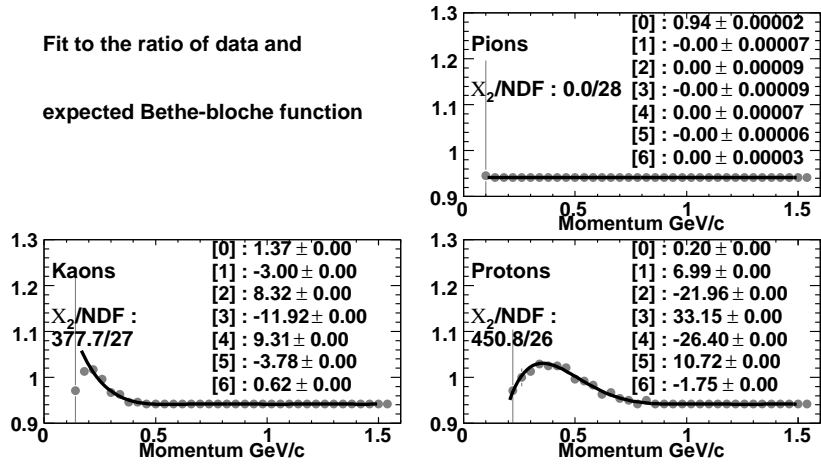


Figure 47.

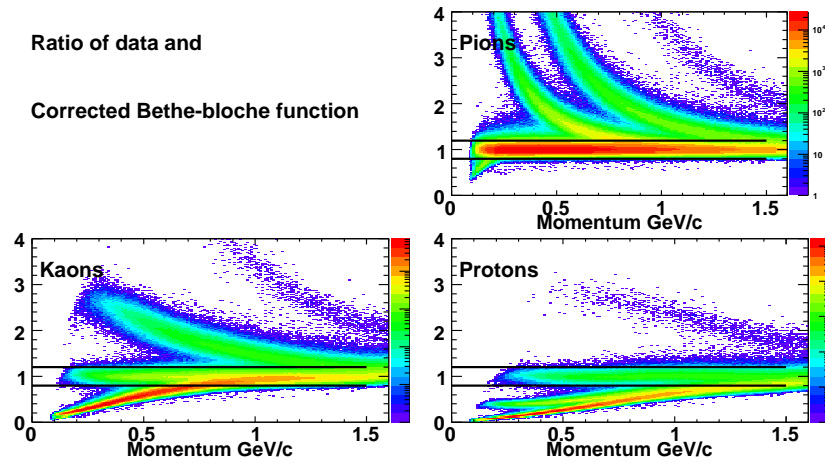


Figure 48.

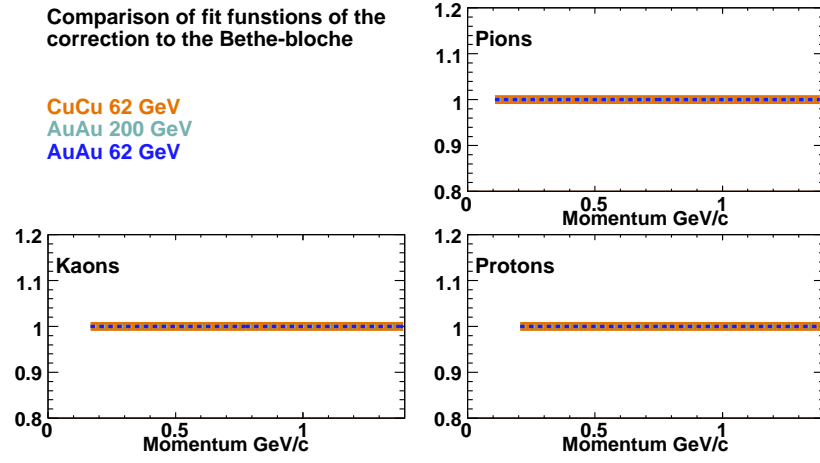


Figure 49. Ratio of correction function obtained using the Cu+Cu 62 GeV, Au+Au 200 GeV and Au+Au 62 GeV data with the Cu+Cy 200 GeV data.

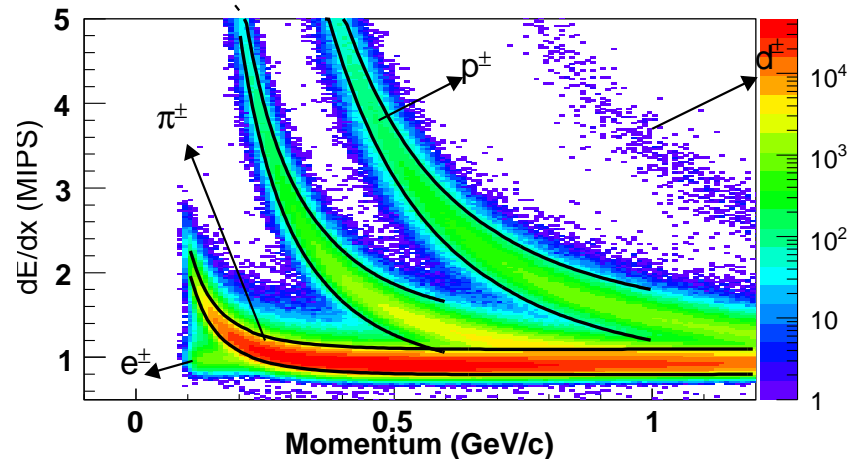


Figure 50.

fit, which is the correction function. The fit values are listed for all the three particles in the Figure 47. The product of the expected Bethe-Bloch function and the fit function gives a better estimate of the particle bands, its called the corrected Bethe-Bloch function. A ratio of the data and the corrected Bethe-Bloch function for all the three particles independently is given in Figure 48. Figure 49 has the ratio of the correction function obtained for Cu+Cu 62 GeV, Au+Au 200 GeV and Au+Au 62 GeV with Cu+Cu 200 GeV. An almost linear ratio obtained as shown in ?? to demonstrate the independence of the correction function from the energy of collision or the species of collision. Finally, obtained particles identification bands are shown in Figure 50.

## Method - 2

This method is based on statistical separation of the bands using gaussian fit functions. Data is analyzed in the bins of momentum (bin size 0.1 GeV/c). A projection of the  $dE/dx$  distribution for a given momentum bin is obtained, as presented in Figure 51 for momentum 0.5-0.51 GeV/c bin. Given here is a truncated mean distribution, hence the individual particle distribution can be represented by the gaussian distributions. Local maxima obtained for each momentum bin are fitted with Gaussian function. The mean and sigma are obtained as a function of momentum for every species. The limit of particle separation (in momentum) is found by measuring the contribution of the neighboring peak. A Cut off in momentum is defined where the contribution from the neighboring peak is more than 4% of its total yield. PID bands are defined from the  $2-\sigma$  distribution around the mean as a function of momentum. Figure 52 shows PID bands obtained using this technique.

## Additional improvement

A technique which is a concoction of both the above mentioned techniques has also been studied. In the improved technique, a triple gaussian fit to the  $dE/dx$  distribution of the particles for a given momentum bin is obtained. The triple gaussian fit has nine parameters. Initial mean value of all the three gaussian is set from the corrected bethe-bloch function using the first method. A very little variation of mean value is allowed. Figure 53 shows the fits for momentum bin from 0.70 GeV/c to 0.79 GeV/c with 0.01 GeV/c bin size. Additional plots for all the momentum bins are available in [??] This method improves the transverse momentum reach of the results.

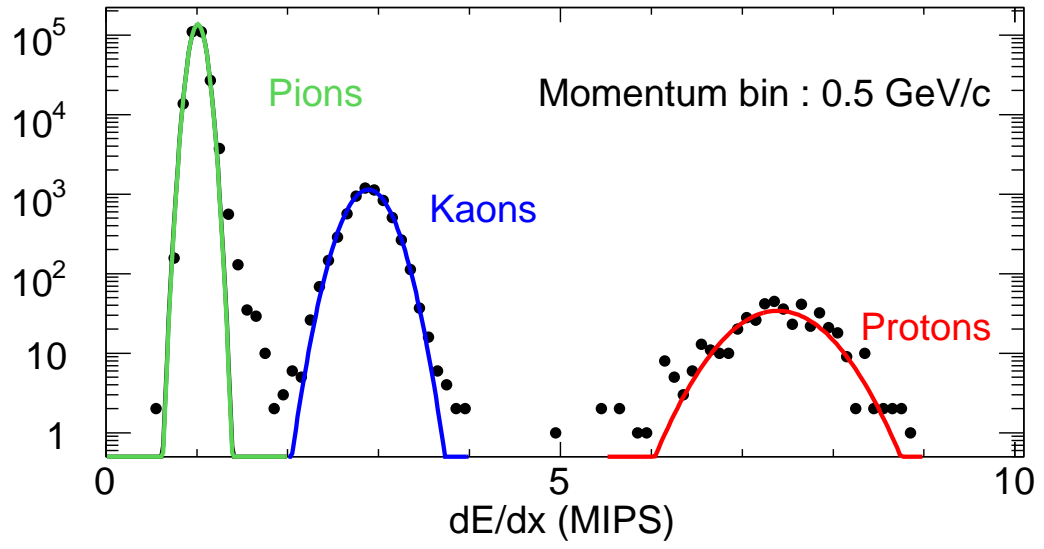


Figure 51.

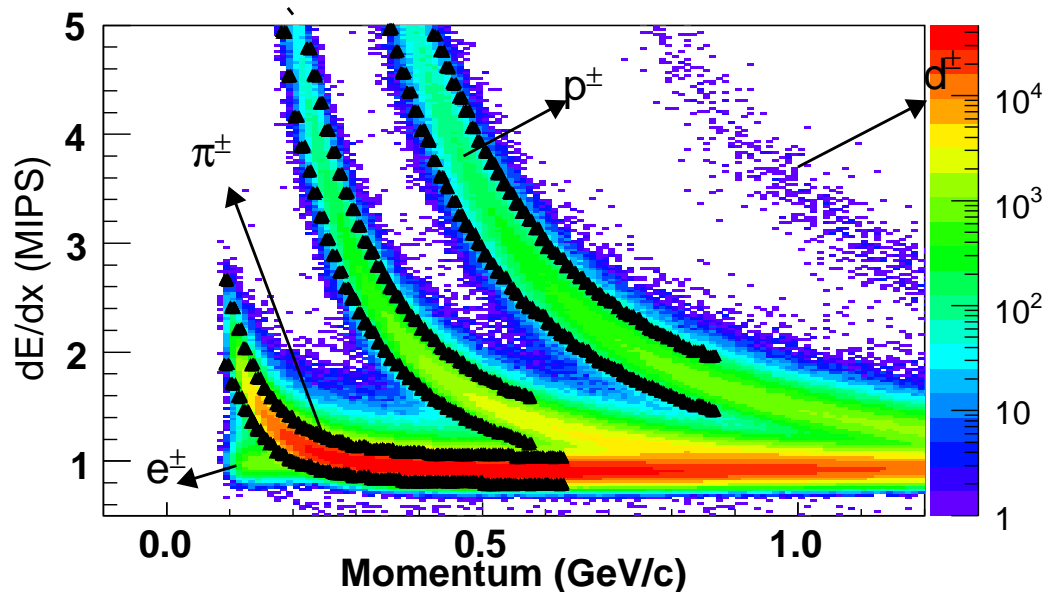


Figure 52.

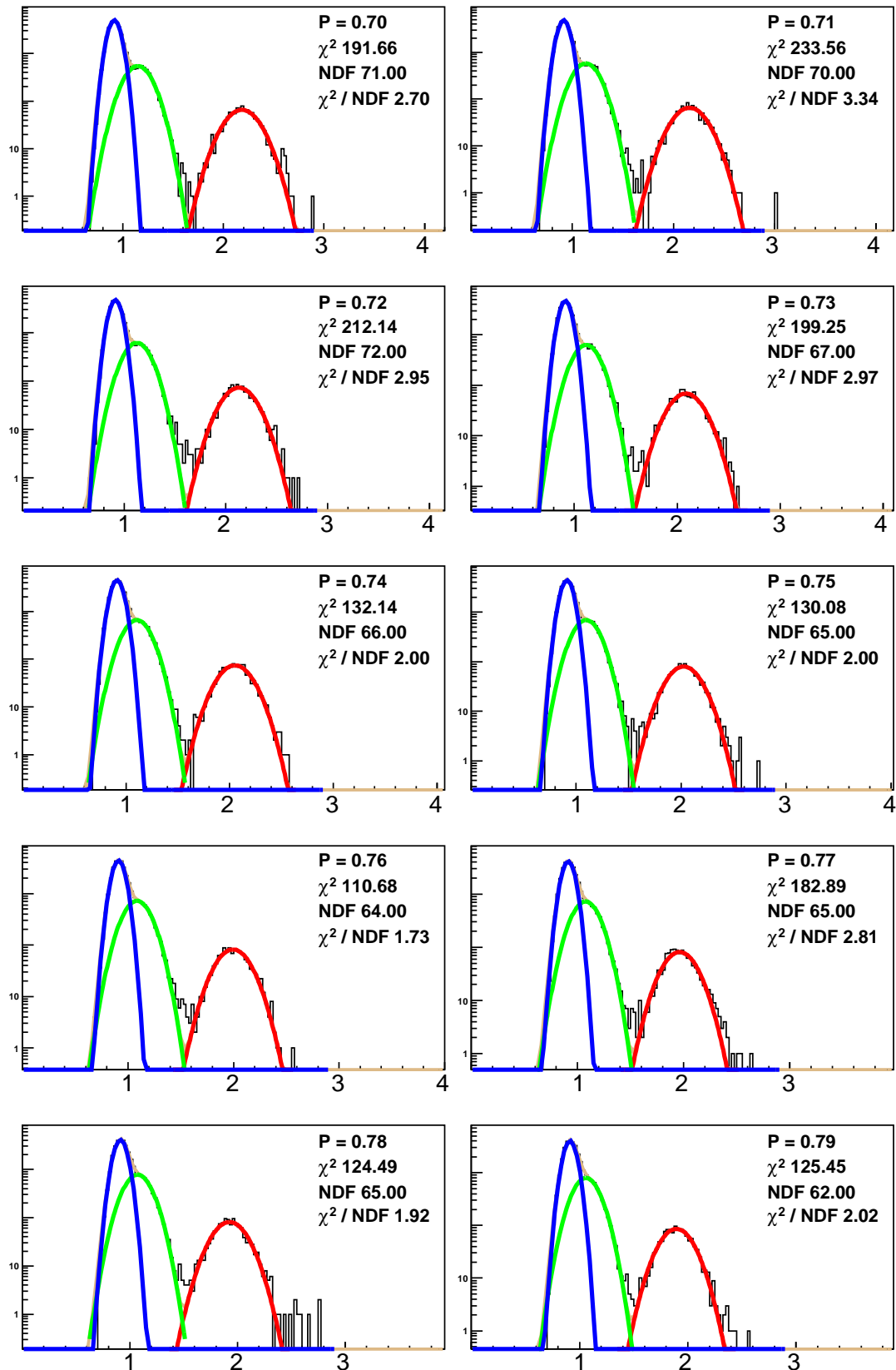


Figure 53.

## 6.2 Raw ratios

Raw ratios (4) for a given arm and bending direction is determined simply by the ratio of number of reconstructed antiparticles ( $\overline{P}_{reco}$ ) per event to that of the particles ( $P_{reco}$ ) per event. This is computed for a given arm and bending direction.

$$\frac{\overline{P}_{reco}(arm, B)}{P_{reco}(arm, B')} \quad (6.4)$$

In considering the oppositely charged particles bending in the same direction, data from opposite magnetic field settings are used. Hence, in the above equation,  $B$  and  $B'$  represent opposite magnetic field settings. That implies if  $B$  equals  $B_1$  then  $B'$  equals  $B_2$  and viceversa, where  $B_1$  and  $B_2$  are the two available field settings as explained previously in 4.

Using the particle identification technique developed in the previous section pions, kaons and protons are differentiated. Counting of the particles is done separately in each spectrometer arm for the forward bending particles and the backward bending particles. As explained previously in the 4, there are four combinations of arms and bending directions obtained. In the following plots the raw ratios obtained for all the four combinations is represented independently. In Table X is given the total number of events, in each polarity, used to produce the raw ratios.

Raw ratios obtained using the PID technique method-II as a function of both the centrality (subsection 3.7) and transverse momentum is presented in the following sub-sections. ?? has raw ratios obtained using method-I. In each plot, different panels correspond to different particle species. In each panel, raw ratios obtained for combinations of different arms and



bending directions are plotted using differently markers. The vertical error bars represent the statistical errors.

### Discussion on statistical error

To obtain equation for the statistical error for the raw ratios, writing the Equation 6.4 explicitly in terms total measured yield(p) and normalization(N)

$$RR(arm, B) = \frac{\overline{P_{reco}}(arm, B)}{\overline{P_{reco}}(arm, B')} = \frac{\overline{p_{reco}}(arm, B)}{N(arm, B)} * \frac{N(arm, B')}{p_{reco}(arm, B')} \quad (6.5)$$

Where RR is the raw ratio. Statistical error for a count of C is  $\sqrt{C}$ . Percent statistical error is given by  $\sqrt{C}/C$ . Percent statistical error for each individual term in the above equation is added quadratically to obtain the over all percent statistical error for the ratio, hence the final error is given by the following equation

$$\sigma_{RR(arm, B), stat} = RR(arm, B) \sqrt{\frac{1}{\overline{p_{reco}}(arm, B)} + \frac{1}{N(arm, B)} + \frac{1}{p_{reco}(arm, B)} + \frac{1}{N(arm, B')}} \quad (6.6)$$

this error computed for every centrality bin and transverse momentum bin separately. It is represented using error bars in the following section.

### Raw ratios as a function of centrality bin

Raw ratios are presented here as a function of centrality bin number. Results are analyzed only for the top centrality bins where there is a guaranteed 100% triggering efficiency. The presented results are integrated over transverse momentum. In the following plots, there is

TABLE X. Total number of events in different polarities used to obtain the final ratios.

	Positive Polarity	Negative Polarity
Cu+Cu 200 GeV	$1.24205 \times 10^7$	$1.37073 \times 10^7$
Cu+Cu 62.4 GeV	$1.85468 \times 10^7$	$1.96633 \times 10^7$
Au+Au 200 GeV	$6.2283 \times 10^6$	$6.55428 \times 10^6$
Cu+Cu 62.4 GeV	$2.1246 \times 10^6$	$2.30824 \times 10^6$

general agreement between the raw ratios obtained using different arms and bending directions, with in statistical error.

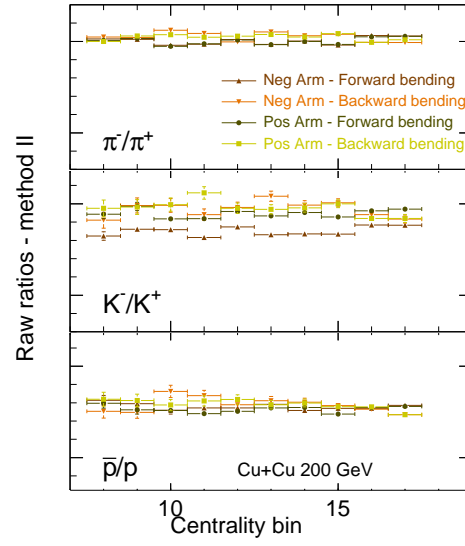


Figure 54. Raw ratios for Cu+Cu 200 GeV data determined using method-II plotted as a function of centrality bin.

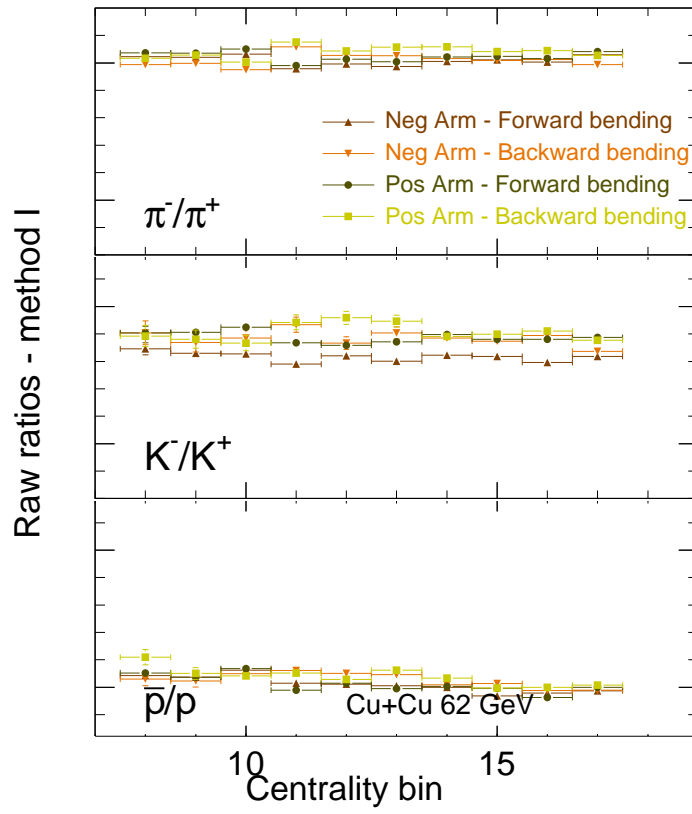


Figure 55. Raw ratios for Cu+Cu 62.4 GeV data determined using method-II plotted as a function of centrality bin.

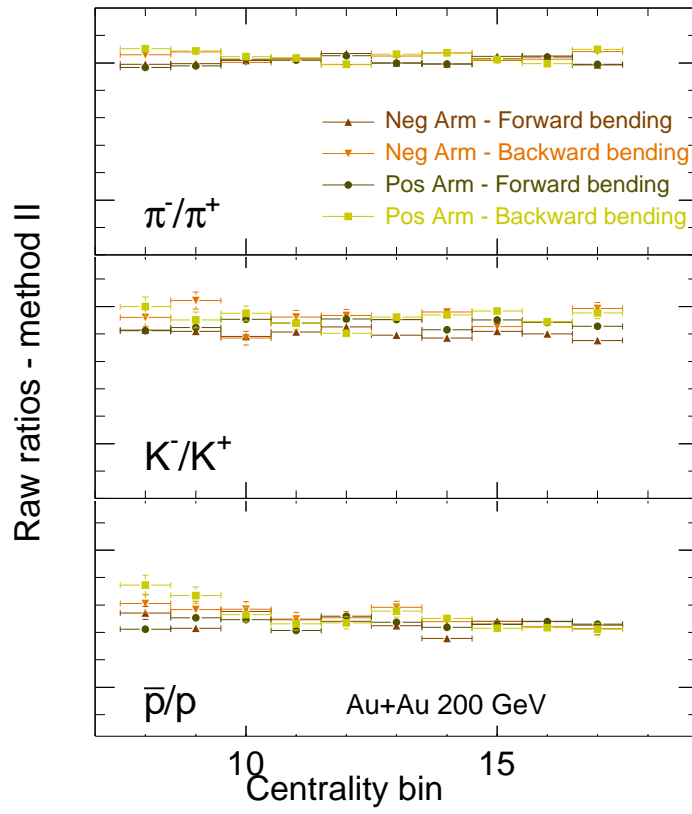


Figure 56. Raw ratios for Au+Au 200 GeV data determined using method-II plotted as a function of centrality bin.

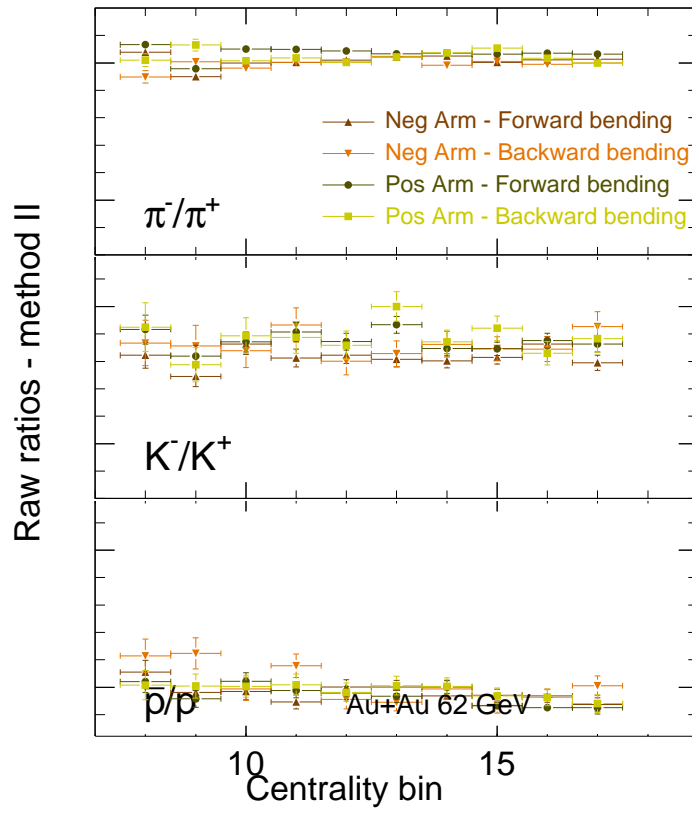


Figure 57. Raw ratios for Au+Au 62.4 GeV data determined using method-II plotted as a function of centrality bin.

### Raw ratios as a function of transverse momentum

Raw ratios in this section are presented as a function of the transverse momentum. Only the top 12% central collisions are considered. The first and the last bins have bigger statistical errors compared to the rest of the bins.

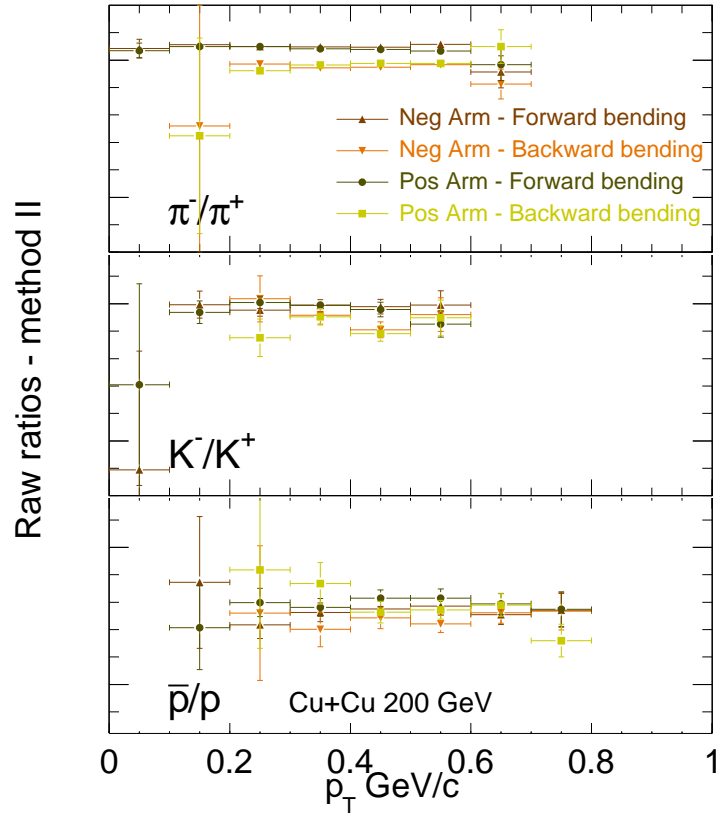


Figure 58. Raw ratios for Cu+Cu 200 GeV data determined using method-II plotted as a function of centrality bin.

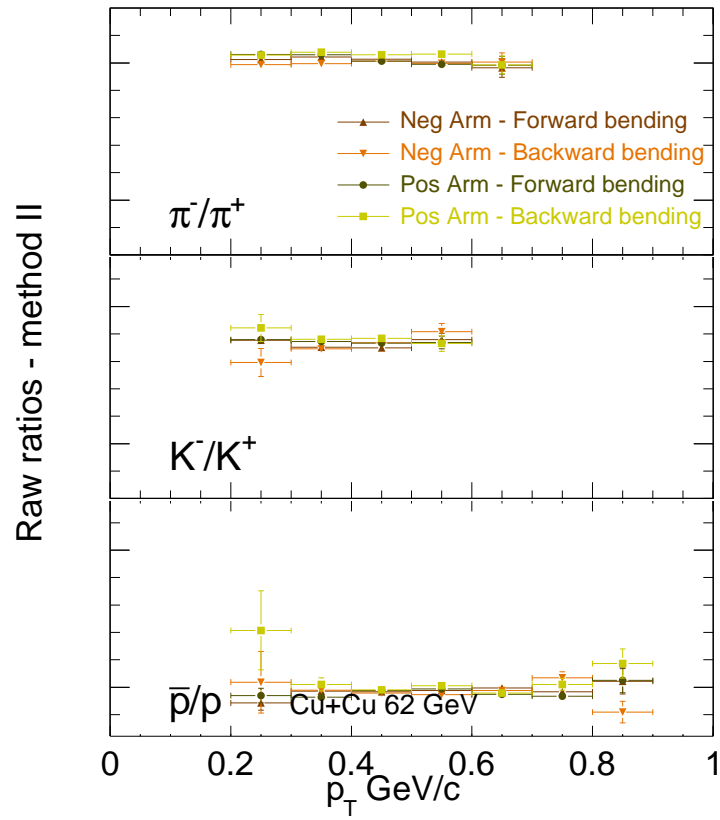


Figure 59. Raw ratios for Cu+Cu 200 GeV data determined using method-II plotted as a function of centrality bin.



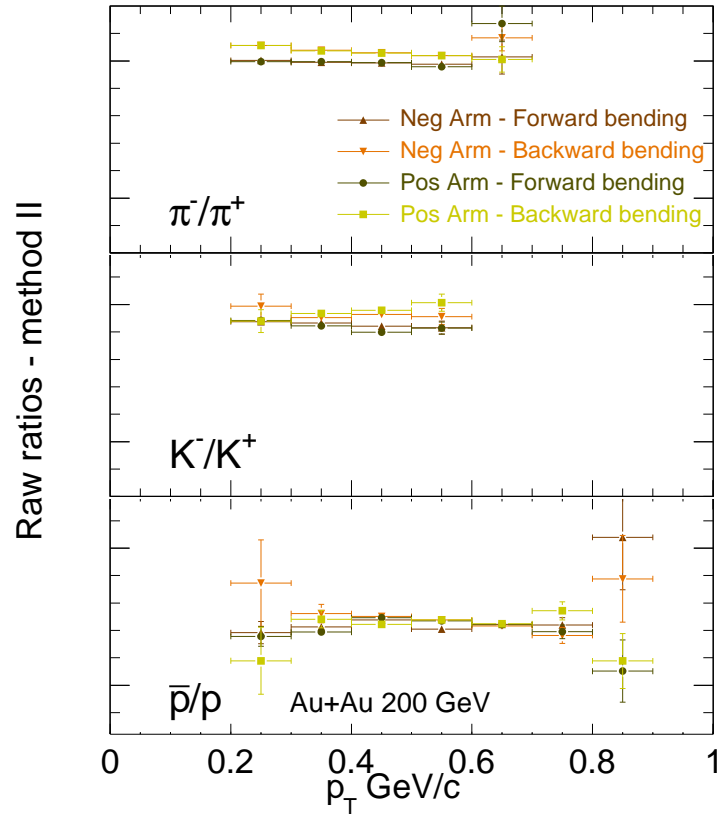


Figure 60. Raw ratios for Au+Au 200 GeV data determined using method-II plotted as a function of centrality bin.

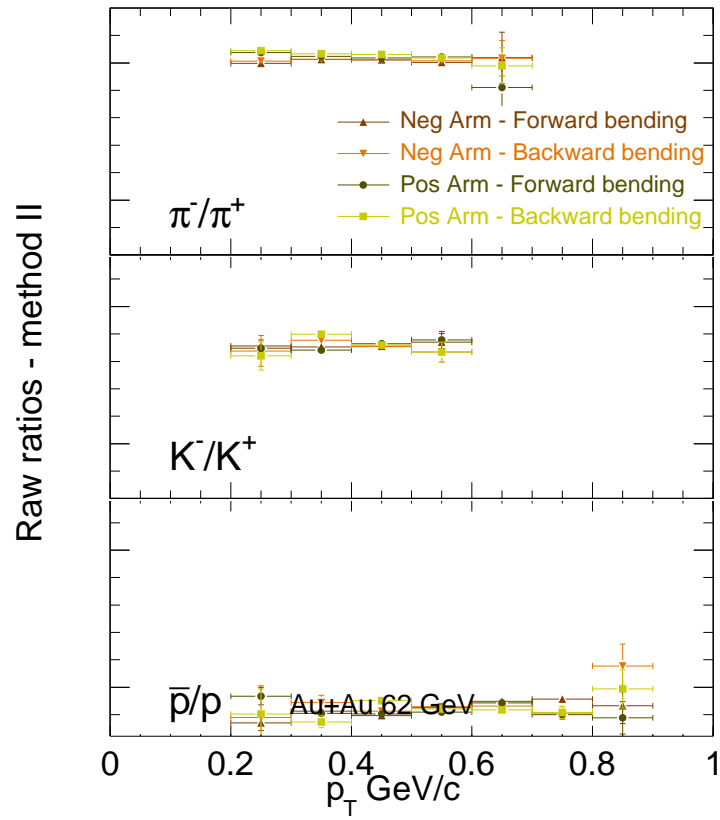


Figure 61. Raw ratios for Au+Au 200 GeV data determined using method-II plotted as a function of centrality bin.

## CHAPTER 7

### CORRECTIONS

The primary yield produced at the interaction point is modified when the particles start swimming through the detector material. This change in the yield can be broadly classified in to two categories.

- Hadronic interactions : The interaction of the particles with the detector material mainly results in their absorption and secondary particle production. Both effects are dominant in the low momentum region ( $p_T < 0.2\text{GeV}/c$ ). The effect of both the absorption and secondary particles production is different in antiparticles from particles. Both these effects are studied independently and corrections are applied successively.
- Decay of particles : Decay of the unstable collisions products, usually hyperons, produces feed-down particles. If the decay length is smaller than the distance between the spectrometer and the collision interaction point, there is finite probability the feed-down particles are reconstructed in the spectrometer. The effect of the feed-down yield is different in the particles compared to anti-particles.

From the discussion of non-primary yield in the 4 Equation 4.1 and Equation 4.6, the correction to the ratio is defined as,

$$\text{non - primary correction to ratio } C(p_T) = \frac{\overline{C_{pri+nonpri}^{pri}}}{C_{pri+nonpri}^{pri}} \quad (7.1)$$

This correction to the ratio can be broken down to absorption correction ( $C_{abs}$ ), secondary correction ( $C_{sec}$ ) and feed-down correction ( $C_{fd}$ ) given by the following equation.

$$C(p_T) = C_{abs}(p_T) * C_{sec}(p_T) * C_{fd}(p_T) \quad (7.2)$$

Secondary particles and the feed-down particles do not always point to the collision interaction point. Requiring the distance of closest approach to reconstructed vertex to be less than 0.35cm reduces the number of non-primary particles(antiparticles) being miss-identified as primary particles(antiparticles). In spite of this requirement of minimum DCA, there is a non-negligible non-primary yield that are reconstructed. Monte-Carlo event generator HIJING is used for studies of the non-primary yields. More detailed description of the corrections and how they are obtained are explained in the following sub-sections.

### **7.1 Absorption correction**

The antiparticles and particles navigating the detector are absorbed by the material due to hadronic interactions with the detector material. This absorption occurs mainly in the beam-pipe region of the detector as it is located closest to the collision interaction point and it is the only detector material the particles pass through before hitting the spectrometer (there are openings in the octagon where the spectrometer arms are located). This correction depends mainly on the transverse momentum of the particles in flight, and it is independent of the multiplicity of the individual events.

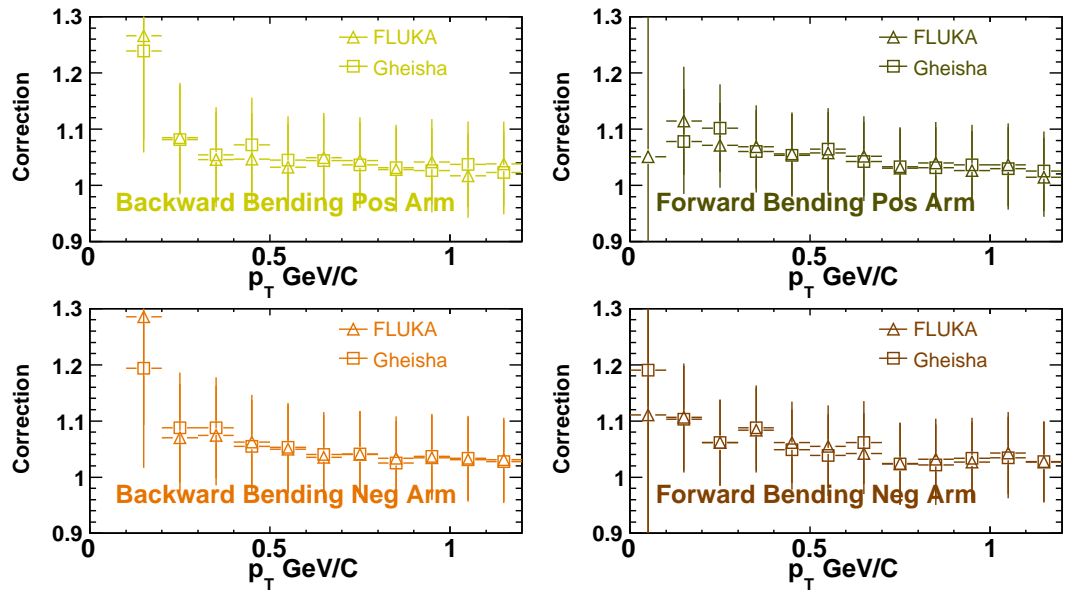


Figure 62. Absorption correction to the ratio for protons as a function of transverse momentum for all four combinations of arms and bending directions represented by different panels. In each panel, triangular marker represents the correction obtained using the FLUKA hadronic interactions package and squares represent the GHEISHA hadronic interactions package.

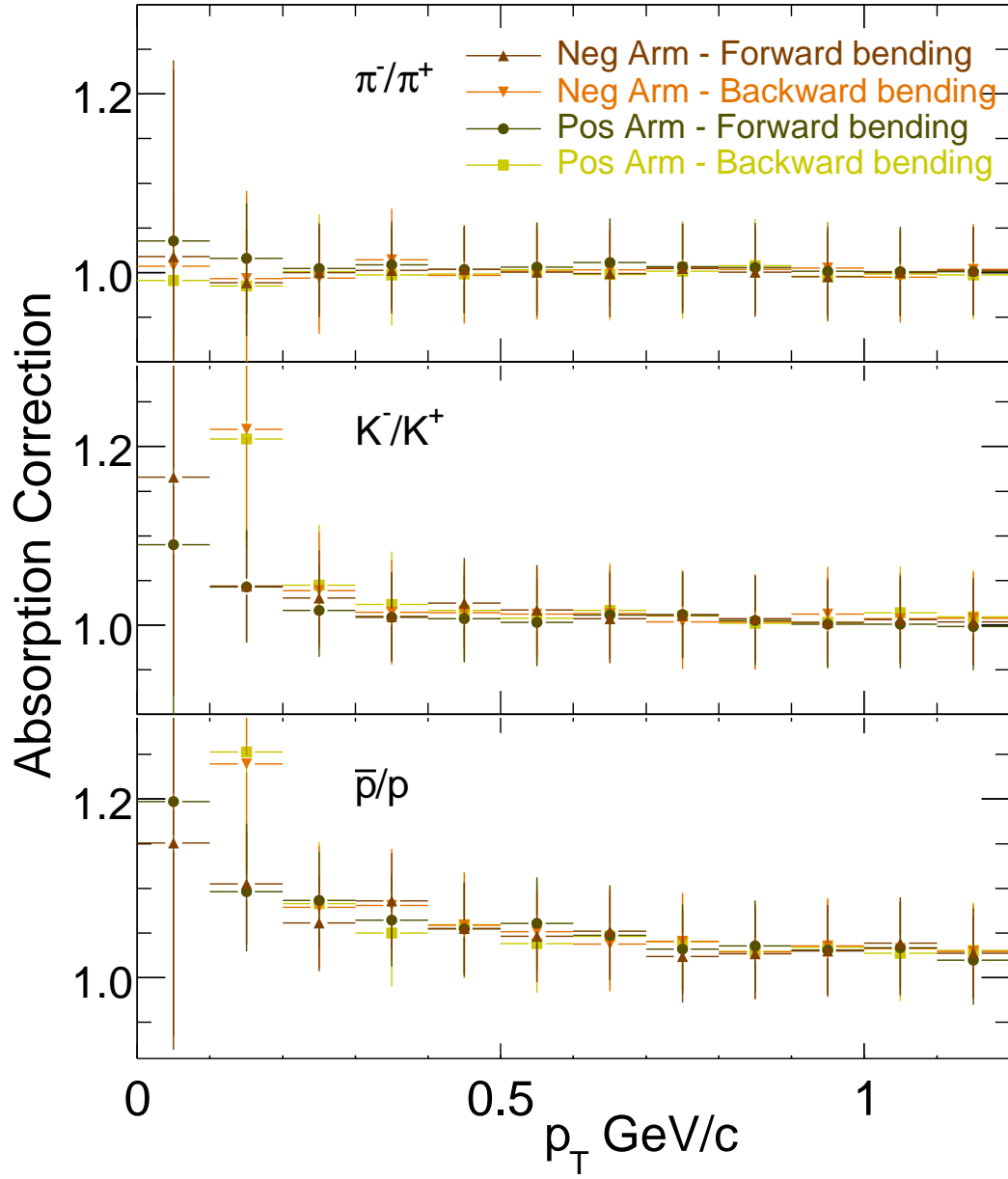


Figure 63. The absorption correction to the ratio as a function of transverse momentum for all the three identified particles corresponding different panels. In each panel, different markers represent different combinations of arms and bending directions.

To determine this correction, GEANT simulation of the detector is used. Antiparticles and particles, with uniform  $p_T$  and pseudorapidity distribution are produced. These Antiparticles and particles are then made to swim through the GEANT simulation of the detector with and without the hadronic interactions switched on. Complete reconstruction of the particles(antiparticles) is performed in the detector. The ratio of yield of the particles(antiparticles) without the hadronic interactions to the yield with the interactions gives the absorption correction to the yield, as shown in Equation 7.3

$$\text{Absorption correction to the yield}(p_T) = \frac{\overline{Y_{reco}}(\text{with out abs})}{\overline{Y_{reco}}(\text{with abs})} \quad (7.3)$$

where  $\overline{Y_{reco}}$  represents the antiparticle, similar correction for the particles is also obtained. Absorption correction to the raw ratio of antiparticle to particle is the ratio of correction to the antiparticle to the correction to the particle, Equation 7.4.

$$\text{Absorption correction to the raw ratio}(p_T) = \frac{\overline{Y_{reco}}(\text{with out abs})}{\overline{Y_{reco}}(\text{with abs})} * \frac{Y_{reco}(\text{with abs})}{Y_{reco}(\text{with out abs})} \quad (7.4)$$

In GEANT there are two different packages, GHEISHA (22) and FLUKA (23), available to simulate the hadronic interactions. The difference in both packages lies in the different methods used to obtain the interaction-cross section. For this study both packages have been used to understand the effect of absorption in the detector material for antiparticles and particles.

Figure 62 shows the absorption correction for different arms and bending directions using both the packages for protons for combinations of different arms and bending directions. Using a complete reconstruction to study the absorption correction function shows that there is no statistically significant difference between both the packages. The average of both the packages has been used for final correction. The variation between both the packages is used for the final systematic error due to absorption correction.

Figure 63 shows the average (between different hadronic interactions packages) absorption correction for different combinations of arms and bending directions for all the three particles. This correction is the most dominant for the anti-proton to proton ratios ranging 0-10% from high to low momentum. A 1% systematic error is assigned due to this correction.



## 7.2 Secondary correction

Secondary particles(antiparticles) are produced when primary particles(antiparticles) in flight interact with the detector material. This interaction with the detector material produces more particles than antiparticles, leading to an undesired effect on the final ratios. The following equation describes the secondary correction as a function of transverse momentum,

$$C_{fd}(p_T) = \frac{\overline{Y_{prim}}}{\overline{Y_{prim}} + \overline{Y_{sec}}} \frac{Y_{prim} + Y_{sec}}{Y_{prim}} \quad (7.5)$$

Rearranging the above equation,

$$C_{fd}(p_T) = \frac{1.0 + \frac{\overline{Y_{sec}}}{\overline{Y_{prim}}}}{1.0 + \frac{Y_{sec}}{Y_{prim}}} \quad (7.6)$$

To obtain this correction, events generated with HIJING followed by complete detector simulation are used. For both particles and antiparticles separately, ratio of reconstructed secondaries to reconstructed primaries ( $\frac{\overline{Y_{sec}}}{\overline{Y_{prim}}}, \frac{Y_{sec}}{Y_{prim}}$ ) is determined as a function of transverse momentum. Final correction function obtained for all the three particles is presented in Figure 64 for Cu+Cu 200 GeV data. The error bars in the Figure 64 are the systematic errors obtained from varying the distance of closest approach cut and the uncertainty of using the Monte-Carlo events.

Protons have the largest correction of up to 1% at low transverse momentum. Kaons and Pion have a almost negligible correction. The secondary production scales with the multiplicity of the event. But in ratios the effect of this scaling with multiplicity is the same in numerator and denominator. Studies were performed as function of collision centrality. To perform this study, a Monte-Carlo events generated using HIJING and processed through a GEANT simulation of the PHOBOS detector is required. Due to limited statistics of availability of complete simulated data, the correction function to the ratio remained constant.

The studies are performed independently for all the collision species and energies.

### 7.3 Feed-down correction

Decay of the unstable collision products, usually hyperons, produces feed-down particles. If the decay length is smaller than the distance between the spectrometer and the collision interaction point, there is finite probability the feed-down particles are reconstructed in the spectrometer. The magnitude of the correction for feed-downs depends on the hyperon relative yield to the primary particles(antiparticles) as demonstrated in the following derivation.

Feed-down correction in terms of yields is given,

$$C_{fd}(p_T) = \frac{\overline{Y_{prim}}}{\overline{Y_{prim}} + \overline{Y_{fd}}} \frac{Y_{prim} + Y_{fd}}{Y_{prim}} \quad (7.7)$$

Replacing the non-primary yield with product of branching ratio (br) and the hyperon parent yield (HP) for particles and antiparticles respectively,

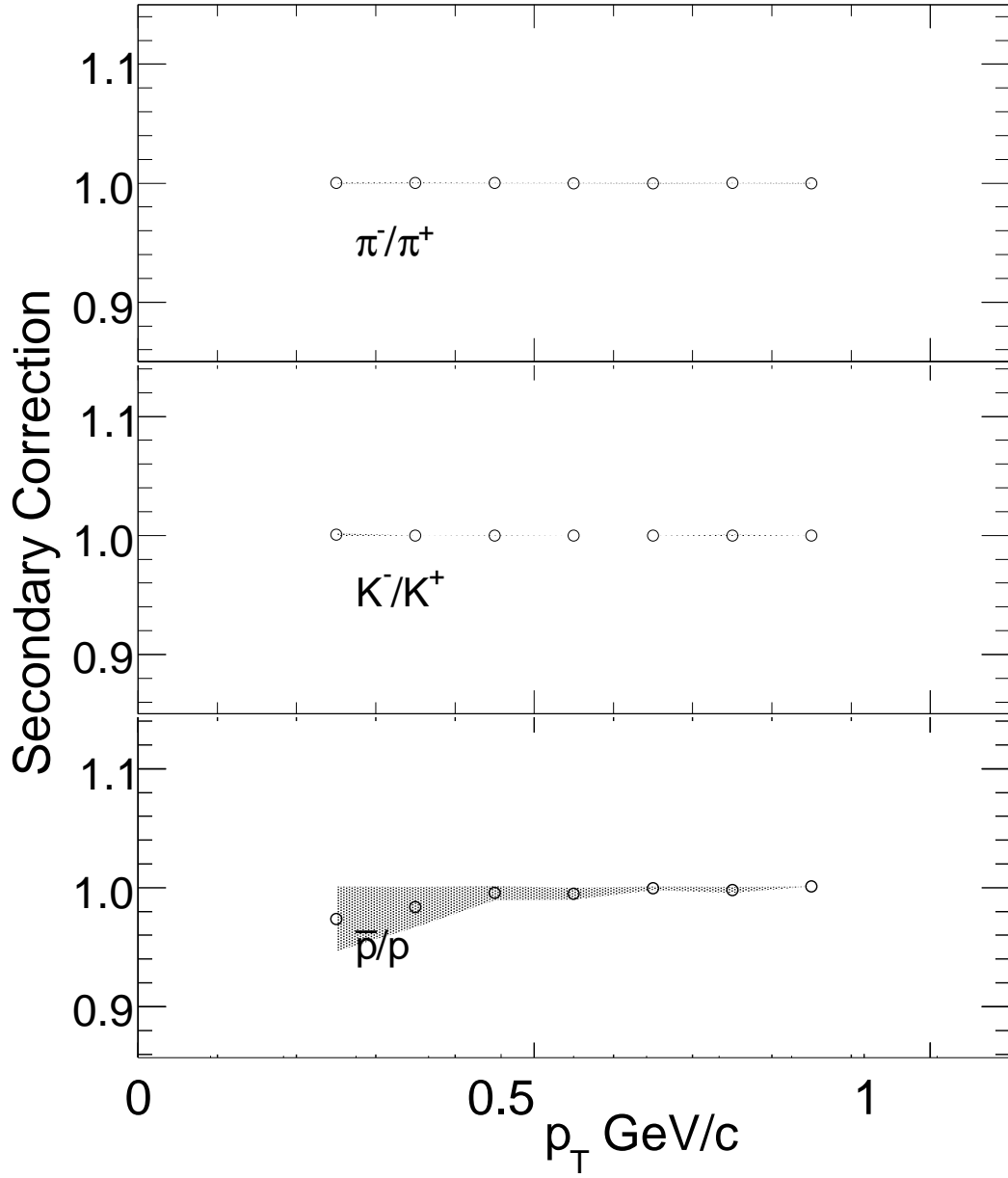


Figure 64. Secondary correction as function of transverse momentum obtained using Cu+Cu 200 GeV HIJING Monte-carlo data. Different panels represent different identified particles.

$$C_{fd}(p_T) = \frac{\overline{Y_{prim}}}{\overline{Y_{prim}} + br * HP_{\overline{Y}}} \frac{Y_{prim} + br * HP_Y}{Y_{prim}} \quad (7.8)$$

Rearranging that equation,

$$C_{fd}(p_T) = \frac{1 + \frac{br * HP_Y}{Y_{prim}}}{1 + \frac{br * HP_{\overline{Y}}}{\overline{Y_{prim}}}} \quad (7.9)$$

The feed-down particles(anti-particles) are produced from the secondary vertex due to mid-flight decay of the hyperon parents. Applying a distance of closest approach cut effects the feed-down particles(anti-particles) differently than the primary particles(anti-particles) which originate from the collision vertex. Hence, an additional acceptance term (acc) needs to be applied as shown in Equation 7.10,

$$C_{fd}(p_T) = \frac{1 + acc * \frac{br * HP_Y}{Y_{prim}}}{1 + \overline{acc} * \frac{br * HP_{\overline{Y}}}{\overline{Y_{prim}}}} \quad (7.10)$$

Possible hyperons that contribute to non-primary yield are listed in the Table XI.

### Protons

For protons, the main contributing factor for the feed-down correction comes from lambda particles. Rewriting the Equation 7.10 for protons and Lambda's.

TABLE XI

LIST OF HYPERONS THAT CONTRIBUTE TO THE NON-PRIMARY YIELD

Hyperon	Decay Length (cm)	Decay mode	Branching Ratio
$\Lambda$	7.89	$P \pi$	$63.9 \pm 0.5$
$\bar{\Lambda}$	7.89	$\bar{P} \bar{\pi}$	$63.9 \pm 0.5$
$\Sigma^+$	2.40	$P \pi^0$	$51.57 \pm 0.30$
$\Sigma^+$	2.40	$N \pi^+$	$48.31 \pm 0.30$
$\Sigma^-$	4.43	$N \pi^-$	$99.848 \pm 0.005$
$\Xi^0$	8.71	$\Lambda \pi^0$	$99.523 \pm 0.013$
$\Xi^-$	4.91	$\Lambda \pi^-$	$99.878 \pm 0.035$

$$C_{fd}(p_T) = \frac{1 + acc * \frac{br * \lambda_P}{P_{prim}}}{1 + \overline{acc} * \frac{br * \lambda_{\bar{P}}}{\lambda_{prim}}} \quad (7.11)$$

Determining factors in understanding this correction are the acceptance and the relative ratio lambdas and primary protons (correspondingly anti-lambdas and primary anti-protons). The acceptance, stands for the ratio of acceptance of the protons produced from lambdas and primary protons (correspondingly for antiparticles). This is studied, similar to absorption correction, by producing a flat (in transverse momentum and psuedorapidity) of both the feeddown protons and the primary protons. These produced particles are then made to swim though the GEANT simulation of the detector. A reconstructibility criterion is defined for the particle, what is percentage of these particles are reconstructed. Acceptance for protons is obtained by taking the ratio of percent of feeddown protons that are reconstructible and percent of primary

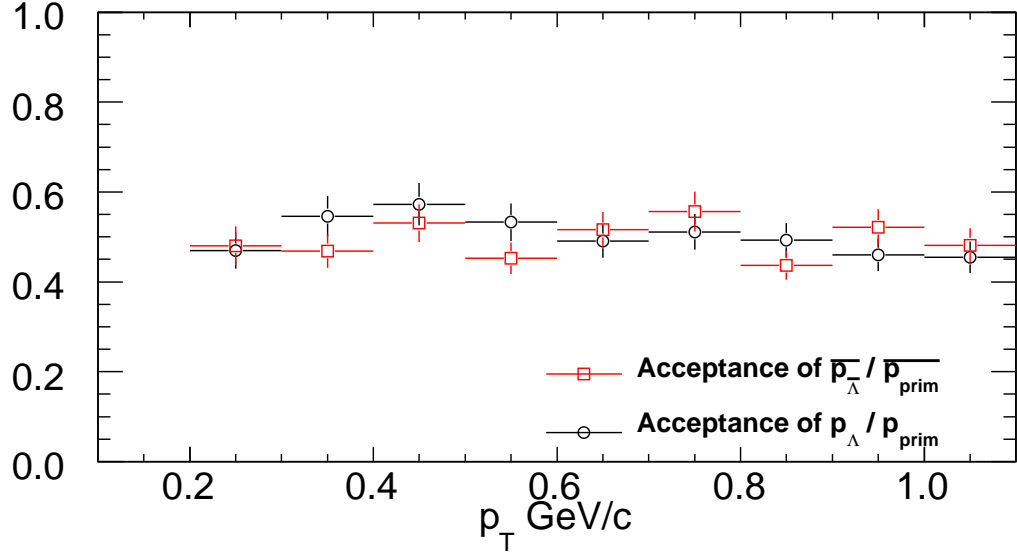


Figure 65. Ratio of acceptance of feed-down and primary protons(antiprotons) as a function of transverse momentum.

protons that are reconstructible, shown using the black markers in Figure 65. A similar study of the antiprotons is shown in red markers. From this study it can be concluded that  $acc$  and  $\bar{acc}$  are similar, and largely independent of transverse momentum. This acceptance does depend on the distance of closest approach cut. The independence of the acceptance as a function of transverse momentum is expected. The track reconstruction efficiency (which depends mainly on the transverse momentum) is the same for feeddown protons and primary protons, hence it cancels out in the ratio.

The lambda to primary proton ratio in the actual collision introduces a additional uncertainty in the analysis. Primarily this ratio is obtained from the HIJING Monte-Carlo. Previ-

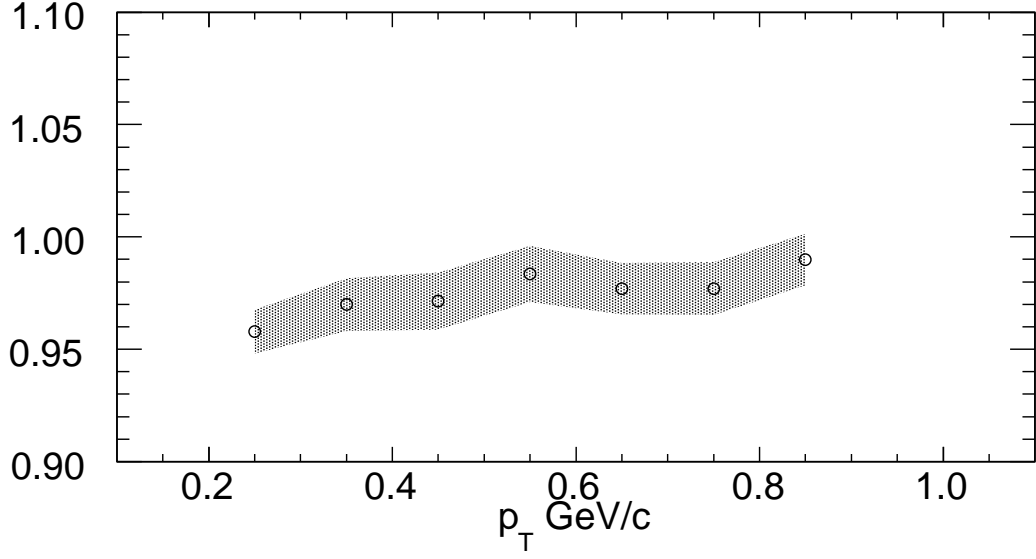


Figure 66. Ratio of acceptance of feed-down and primary protons(antiprotons) as a function of transverse momentum.

ously published data (Au+Au 130 GeV data) has shown that, this ratio of Lambda over Proton in HIJING is not consistent with data. For Cu+Cu collisions, published data is not available. Another approach to this problem is using the Quark Coalescence model (24). In this model the number of primary particles produced is assumed to be proportional to the product of the number of constituent quarks.

$$\frac{\lambda_{\bar{P}}}{P_{prim}} \frac{P_{prim}}{\lambda_P} = \frac{\lambda_{\bar{P}}}{\lambda_P} \frac{P_{prim}}{P_{prim}} = \frac{\bar{u}\bar{d}\bar{s}}{uds} * \frac{uud}{\bar{u}\bar{u}\bar{d}} = \frac{u\bar{s}}{\bar{u}s} \quad (7.12)$$

$$\frac{\lambda_{\bar{P}}}{P_{prim}} \frac{P_{prim}}{\lambda_P} = \frac{K^+}{K^-} \quad (7.13)$$

Using this argument, the ratio Lambda over proton ratio can be adjusted to the ratio of measured kaons. For this analysis, the feed-down correction was obtained using the HIJING Monte-Carlo events. A systematic error is assigned to the feed-down correction proportional to the difference in the obtained feeddown correction by adjusting the lambda over proton ratio to the kaon ratio. The same procedure is used for all the species and collision energies.

### **Kaons and Pions**

For kaons and pions, the overall feed-down contribution is negligible. This partly due to the fact that the feed-down contributions are mostly due to symmetric (contributing the same amount to particles and anti-particles). Approximately 1% systematic error is included to account for any unaccounted for uncertainty.



The corrections are studied as a function of transverse momentum. To obtain the correction for a given centrality bin, weighted average over the transverse momentum is considered. The weight is obtained from the statistics of the given transverse momentum bin.

## CHAPTER 8

### SYSTEMATIC STUDIES

A systematic study of the all the applied cuts in this analysis have is performed. Other than the off-line event selection cuts as described in subsection 3.7, cuts applied for track selection and particle identification are also studied. Following is the list of variables considered.

- Beam-orbit : Data from different beam-orbit regions were used to understand the systematic variations on the final ratios.
- Distance of closest approach (DCA) to beam-orbit cut : A 0.35 cm DCA cut has been used in the analysis. A variation DCA from 0.1 cm to 0.5 cm has been studied.
- Paddle-time difference : Paddle time difference is a an off-line good event selection cut. It has different values for different data sets.
- Particle identification band width : A  $2\text{-}\sigma$  cut on the particle identification bands has been used to obtain the raw ratios. A variation of  $1\text{-}\sigma$  to  $3\text{-}\sigma$  has been studied.
- Track selection cut study : A track selection cut of track fit probability  $> 0.04$  is used for the analysis. A variations of track fit probability cut from 0 to 1 is studied.
- Vertex-cut study : In Cu+Cu 200 GeV and 62.4 GeV data a reconstructed vertex cut of  $\pm 9$  cm and, in Au+Au 200 GeV and 62.4 GeV data a reconstructed vertex cut of  $\pm 10$  cm is used. A variation of  $\pm 2$ cms around the vertex cut is studied.

Following is the procedure used to understand the effect of systematic variation.

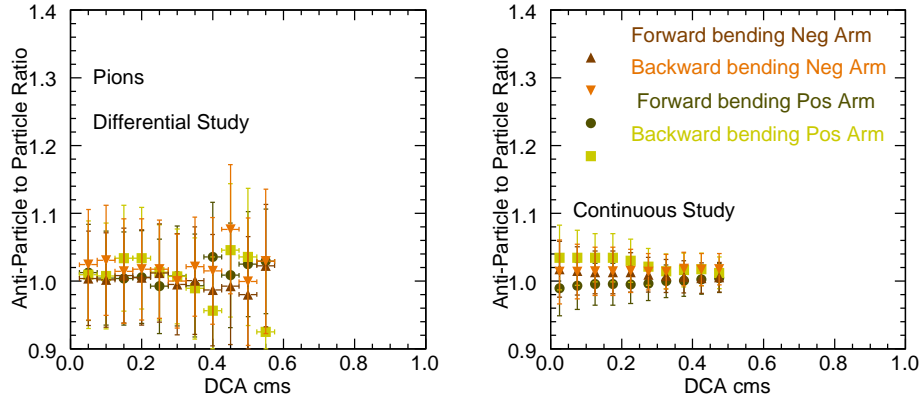


Figure 67. Study of the systematic variation of the DCA cut. Left panel, min-bias raw ratios in the bins of the DCA cut. Right panel, min-bias raw ratio as a function of applied cut. The data presented here is for pions in Cu Cu 200 GeV.

- Step 1 :** Min-bias raw ratio in the bins of the given variable is obtained. For example, Figure 67 left panel plotted is the raw ratios in the bins of DCA for pions. The purpose of this study is to see any anomalous behavior occurring outside the statistical uncertainty. Similar study is performed for all the three identified particles.
- Step 2 :** Min-bias ratio as a function of the applied cut, is studied. This is unlike the previous study which is more differential. For example, in Figure 67 right panel for DCA cut plotted is the raw ratio by varying the applied DCA cut from 0.1 to 0.5 is plotted. Again, this is studied independently for all the different identified particles. The purpose of the study is to understand the magnitude of the systematic uncertainties that may arise due to this experimental cut .

- **Step 3 :** The final systematic uncertainties on the ratios as a function of centrality for varying the applied cut is computed using a similar procedure similar to the previous step, but in bins of centrality. The spread of the distribution of the raw ratio, in a given centrality bin, is measured. This spread is considered to be the systematic error for the applied cut if the magnitude of the spread is more than that of the statistical spread in that bin.
- **Step 4 :** Essentially the same as the step 3, but in transverse momentum bins.
- All of the above four steps are repeated for each arm and bending direction independently.

In Table XII is given the summary of all systematic variation of all the studied variable. The mean value and maximum value of systematic variation obtained for different variables for different combinations of arm and bending direction for all the particles using Cu+Cu 200 GeV data is presented. Except for track fit probability, which is explained in detail in the next sub-section, the other variables did not show any anomalous behavior outside of statistical uncertainty. The over all systematic variation for backward bending data is more than that in the forward bending data. Results Cu+Cu 62.4 GeV, Au+Au 200 GeV and Au+Au 62.4 GeV show a similar behavior. Final systematic errors for all the different energies and colliding species are presented in table form in the results chapter.

TABLE XII

PRESENTED IN THE TABLE IS SUMMARY OF SYSTEMATIC STUDIES FOR CU+CU 200 GEV DATA. EACH SUB-TABLE CORRESPONDS TO A DIFFERENT VARIABLE FOR ALL THE THREE IDENTIFIED PARTICLES CORRESPONDING TO DIFFERENT ROWS. IN EACH SUB-TABLE DIFFERENT COLUMNS CORRESPOND TO DIFFERENT ARMS AND BENDING DIRECTION COMBINATIONS AS LABELED IN THE HEADER COLUMN.

	Arm-1				Arm-2			
	Backward B		Forward B		Backward B		Forward B	
	Mean	Max	Mean	Max	Mean	Max	Mean	Max
Beam-orbit								
Proton	0.010	0.024	0.007	0.017	0.010	0.023	0.008	0.019
Kaon	0.010	0.025	0.006	0.015	0.011	0.027	0.008	0.020
Pion	0.005	0.013	0.005	0.012	0.005	0.013	0.005	0.012
DCA to Beam-orbit								
Proton	0.005	0.015	0.007	0.013	0.006	0.016	0.010	0.016
Kaon	0.011	0.023	0.009	0.015	0.007	0.018	0.010	0.017
Pion	0.005	0.009	0.007	0.011	0.007	0.011	0.007	0.011
Paddel time difference								
Proton	0.004	0.014	0.004	0.011	0.014	0.023	0.007	0.014
Kaon	0.009	0.020	0.005	0.011	0.012	0.024	0.010	0.016
Pion	0.006	0.010	0.007	0.011	0.007	0.012	0.007	0.011
PID band-width								
Proton	0.004	0.004	0.011	0.011	0.001	0.001	0.002	0.002
Kaon	0.002	0.002	0.008	0.008	0.001	0.001	0.001	0.001
Pion	0.001	0.001	0.007	0.007	0.000	0.000	0.002	0.002
Track fit probability								
Proton	0.051	0.051	0.029	0.029	0.060	0.060	0.037	0.037
Kaon	0.062	0.062	0.037	0.037	0.064	0.064	0.029	0.029
Pion	0.037	0.037	0.006	0.006	0.048	0.048	0.015	0.015
Vertex cut								
Proton	0.005	0.018	0.008	0.017	0.007	0.020	0.012	0.019
Kaon	0.013	0.026	0.011	0.017	0.007	0.020	0.013	0.020
Pion	0.007	0.011	0.009	0.012	0.008	0.013	0.009	0.012
Summed systematic								
Proton	0.057	0.064	0.039	0.045	0.067	0.075	0.046	0.053
Kaon	0.072	0.081	0.045	0.050	0.071	0.078	0.042	0.050
Pion	0.041	0.044	0.020	0.027	0.052	0.055	0.024	0.030

### Track fit probability - systematic variation study

Raw ratio obtained in the bins of track fit probability is shown in Figure 68 for pions, kaons and protons in Cu+Cu 200 GeV data. The min-bias raw ratios for backward bending tracks shows a dependence on the track fit probability variable, more obvious from the pion distribution due to better statistics. Presented in Table XIII are the values of slopes and intercept, and their corresponding errors, to the straight line fits to the distributions presented in the Figure 68 for the pions, kaons and protons. Track fit probability is a function of the  $\chi^2$  and the number of degrees of freedom obtained from the final fit to the reconstructed track. Again, a similar behavior with same sign and order of magnitude is observed in the Cu+Cu 62 GeV, Au+Au 200 GeV and Au+Au 62.4 GeV in all the three species.

A further study performed for the simulated and reconstructed Monte-Carlo data did not show this behavior as a function of track fit probability variable. Due to this fact, a much conservative track fit probability systematic error estimation is used for the towards the summed systematic error for the final ratios. This systematic error due to track fit probability is obtained from the rms value of the y-axis projection of the raw ratio as a function of track fit probability. These rms values are also listed in the Table XIII. The same value is used for all the centrality bins and momentum bins.

This conservative estimation of the systematic error eliminates the need for including the systematics due to different bending directions with an argument that variation in the raw ratios due to track fit probability is directly correlated to the variation in raw ratios in different bending directions. There is a difference in track reconstruction efficiency due to asymmetry

of the spectrometer between the forward and back bending tracks and correspondingly the raw ratios obtained from them. The magnetic field is arguably the only other difference between forward bending and backward bending raw ratios. If this variation of raw ratio as a function of track fit probability is being caused by the magnetic field, then the forward bending raw ratios as a function of track fit probability should have a slope comparable in magnitude to that of the backward bending raw ratios but with an opposite sign to the slope. From the Table XIII, it can be concluded that the forward bending ratios have slope opposite in sign to that of the backward bending raw ratios but more consistent with zero magnitude. Hence, it can be inferred that there is a bias in backward bending raw ratios. This argument does invalidate previous claims about tracking efficiency canceling out in the formula for computing the raw ratios, because that argument is only valid for the a given and bending direction. Further, the intercept value of fit function reflects the difference in the (averaged over the track fit probability) forward bending and backward bending ratios. Thus, in the final accounting for the systematic error from the track fit probability additional contribution due to different bending directions is not considered.

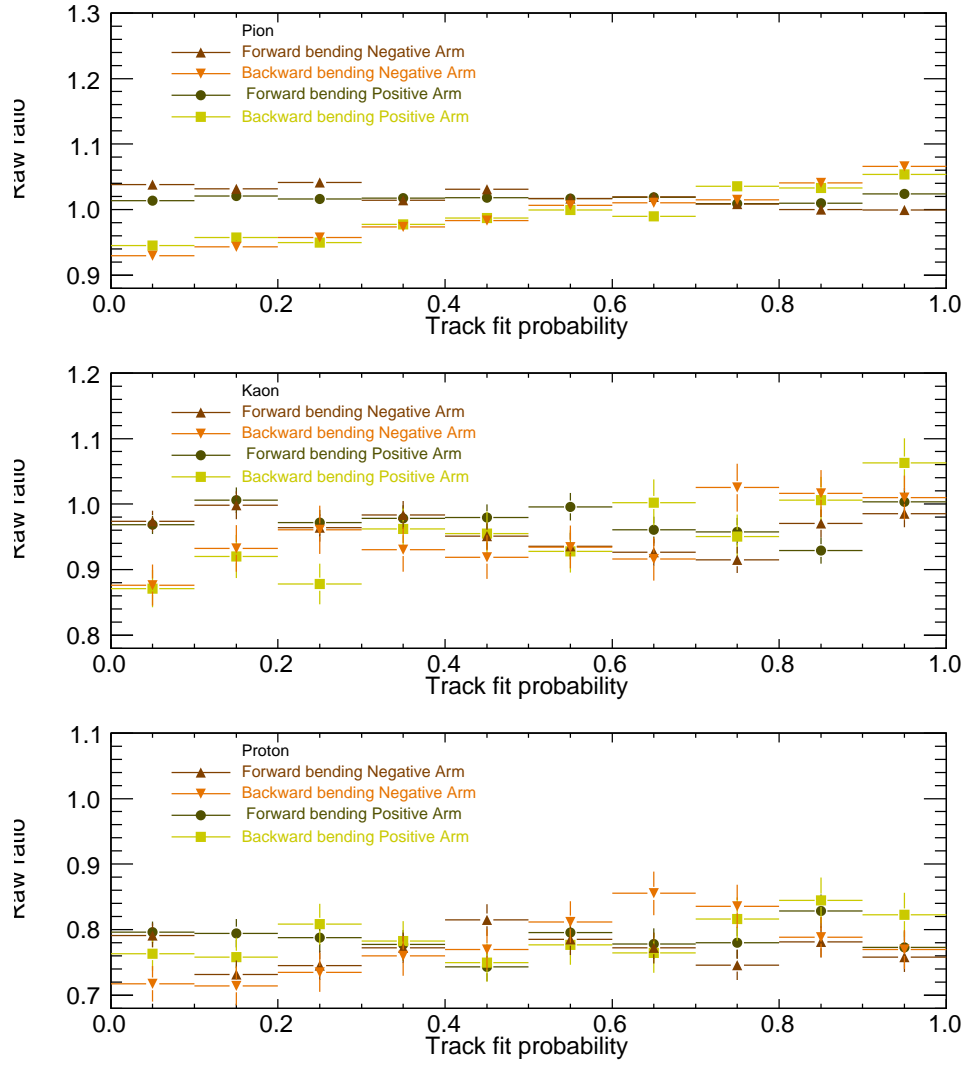
TABLE XIII

PRESENTED IN THIS TABLE ARE THE SLOPES, INTERCEPTS AND RMS VALUES FOR MIN-BIAS RAW RATIOS IN THE BINS OF TRACK FIT PROBABILITY FOR THE CU+CU 200 GEV DATA FOR ALL THE THREE IDENTIFIED PARTICLES. THE SLOPE AND THE INTERCEPT ARE OBTAINED USING A STRAIGHT LINE FIT FOR DISTRIBUTION AS SHOWN IN ?? FOR PIONS. THE RMS VALUE IS OBTAINED BY TAKING A Y-AXIS PROJECTION OF THE SAME DISTRIBUTION.

	Slope	Intercept	RMS
Pion			
Backward bending Positive Arm	$0.119 \pm 0.007$	$0.954 \pm 0.004$	0.037
Forward bending Positive Arm	$-0.001 \pm 0.003$	$1.004 \pm 0.001$	0.006
Backward bending Negative Arm	$0.159 \pm 0.007$	$0.930 \pm 0.004$	0.048
Forward bending Negative Arm	$-0.044 \pm 0.003$	$1.029 \pm 0.002$	0.015
Kaon			
Backward bending Positive Arm	$0.141 \pm 0.027$	$0.893 \pm 0.014$	0.062
Forward bending Positive Arm	$-0.030 \pm 0.013$	$0.959 \pm 0.007$	0.037
Backward bending Negative Arm	$0.172 \pm 0.026$	$0.871 \pm 0.015$	0.064
Forward bending Negative Arm	$-0.043 \pm 0.014$	$0.965 \pm 0.008$	0.029
Kaon			
Backward bending Positive Arm	$0.054 \pm 0.023$	$0.762 \pm 0.013$	0.051
Forward bending Positive Arm	$-0.005 \pm 0.015$	$0.77 \pm 0.008$	0.029
Backward bending Negative Arm	$0.116 \pm 0.023$	$0.719 \pm 0.013$	0.060
Forward bending Negative Arm	$-0.035 \pm 0.016$	$0.794 \pm 0.009$	0.036



Figure 68. Min-bias raw ratio as a function of track fit probability variable for Cu+Cu 200 GeV data. The different panels correspond to different identified particles.



The final systematic error due to cuts applied in the analysis is computed by summing quadratically the different above mentioned contributions. Shown in the Figure 69 is an example of the systematic study (represented using differently colored markers) and the final computed error (represented using black histogram) for protons in Cu+Cu 200 GeV data as function of centrality bin. The systematic variation due to the track fit probability study has the maximum weight in the final systematic error for all the three identified particles and all the collision energies and species. The description of obtaining the final systematic error, weighted summed over different arms and bending directions, is explained in the results chapter.

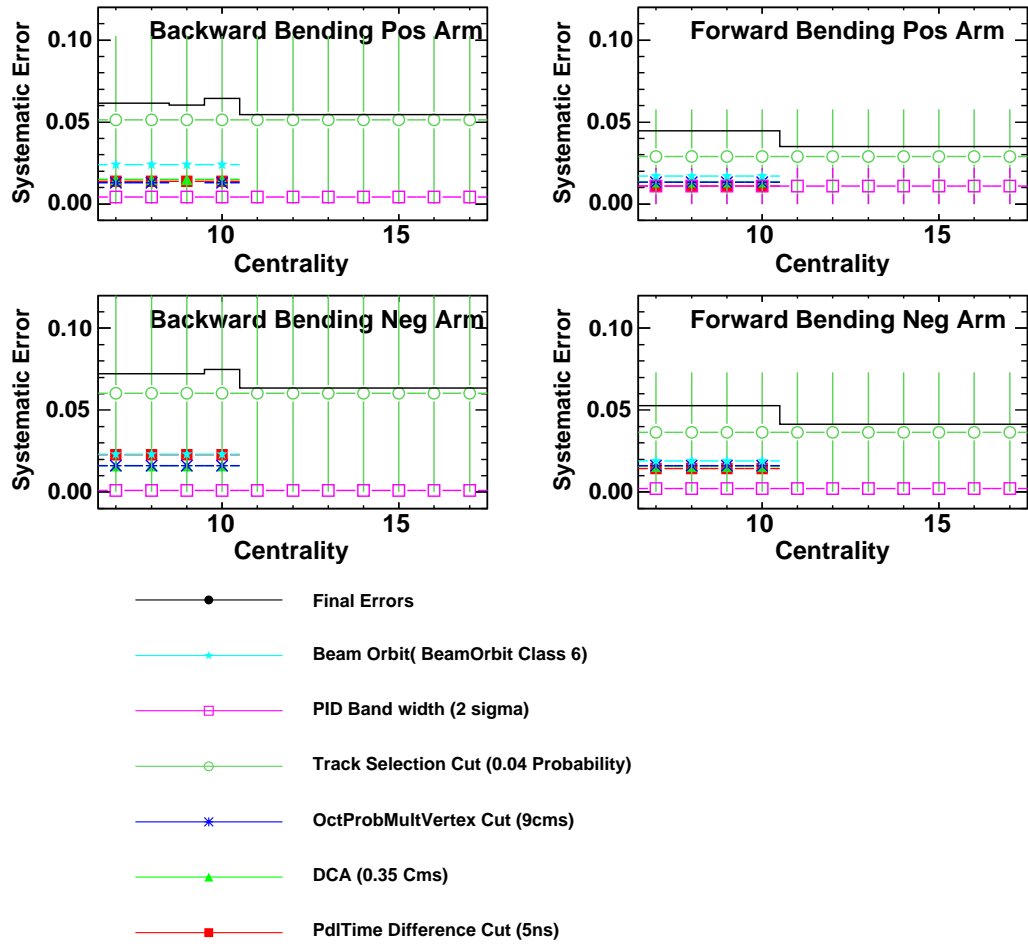


Figure 69. Systematic study for the different variable and final systematic error for proton ratios in Cu+Cu 200 GeV data. The study is presented in different arms and bending directions separately.

## CHAPTER 9

### RESULTS AND INTERPRETATION

#### 9.1 Results

To arrive at the the final results the corrections have to be applied, individual measurements obtained from different arms and bending directions have to be summed (properly with weights), and final systematics have to be determined.

#### **Combining ratio obtained using different arms and bending directions**

To combine the ratios obtained using different arms and bending directions Equation 9.1, the weights are obtained using the statistical and systematic errors. Ratios are studied as a function of centrality bin and the transverse momentum, hence statistical error is determined for every bin in centrality and transverse momentum separately, Chapter 6.2 Equation 6.6. As explained in chapter 8, even the systematic errors are determined separately for each bin in centrality and transverse momentum. Formula for combining the ratios is given by,

$$Final\ Ratios(centrality, p_T) = \sum_{B=B_2}^{B_1} \sum_{arm=arm_P}^{arm_N} W(arm, B, B') R(arm, B) C(arm, B) \quad (9.1)$$

$$R(arm, B) = RR(arm, B) C(arm, B)$$

$$RR(arm, B) = \frac{\overline{P_{pri}}(arm, B)}{P_{pri}(arm, B')}$$

$C(\text{arm}, B) = \text{correction to the ratio}$

$$\sum_{B=B_2}^{B_1} \sum_{\text{arm}=\text{arm}_P}^{\text{arm}_N} W(\text{arm}, B, B') = 1 \quad (9.2)$$

Where  $B$  and  $B'$  represent opposite magnetic field settings. That implies if  $B$  equals  $B_1$  then  $B'$  equals  $B_2$  and viceversa, where  $B_1$  and  $B_2$  are the two available field settings as explained previously in chapter 4.

Weight for a given centrality bin or the transverse momentum bin is given by the combined statistical and systematic error,

$$W(\text{arm}, B, B') = \frac{\left(\frac{1}{\sigma_{R(\text{arm}, B), \text{stat}}}\right)^2 + \left(\frac{1}{\sigma_{R(\text{arm}, B), \text{sys}}}\right)^2}{\sum_{B=B_2}^{B_1} \sum_{\text{arm}=\text{arm}_P}^{\text{arm}_N} \left(\frac{1}{\sigma_{R(\text{arm}, B), \text{stat}}}\right)^2 + \left(\frac{1}{\sigma_{R(\text{arm}, B), \text{sys}}}\right)^2} \quad (9.3)$$

### Obtaining the final systematic error

The final systematic error for a given centrality bin or transverse momentum bin is obtained by adding the systematic error for all the different arms and bending direction weighted by the statistical error.

$$\sigma_{\text{sys}}^2 = \sum_{B=B_2}^{B_1} \sum_{\text{arm}=\text{arm}_P}^{\text{arm}_N} \frac{(\sigma_{R(\text{arm}, B), \text{sys}})^2 \left(\frac{1}{\sigma_{R(\text{arm}, B), \text{stat}}}\right)^2}{\sum_{B=B_2}^{B_1} \sum_{\text{arm}=\text{arm}_P}^{\text{arm}_N} \left(\frac{1}{\sigma_{R(\text{arm}, B), \text{stat}}}\right)^2} \quad (9.4)$$

### Obtaining the final statistical error

The final statistical error for a given centrality bin or transverse momentum bin is obtained by adding quadratically adding the statistical error from different arms and bending directions

$$\frac{1}{\sigma_{stat}^2} = \sum_{B=B_2}^{B_1} \sum_{arm=arm_P}^{arm_N} \left( \frac{1}{\sigma_{R(arm,B),stat}} \right)^2 \quad (9.5)$$

### Final results

Presented in this section are the final results of antiparticle to particle ratios as a function of transverse momentum ( Figure 70 and Figure 71) and as function of centrality ( Figure 72). The statistical error are presented using the vertical error bars and the systematic errors using the error band. The corresponding data tables are present in Table XIV, Table XV and Table XVI. More discussion on these results follows in the next section.

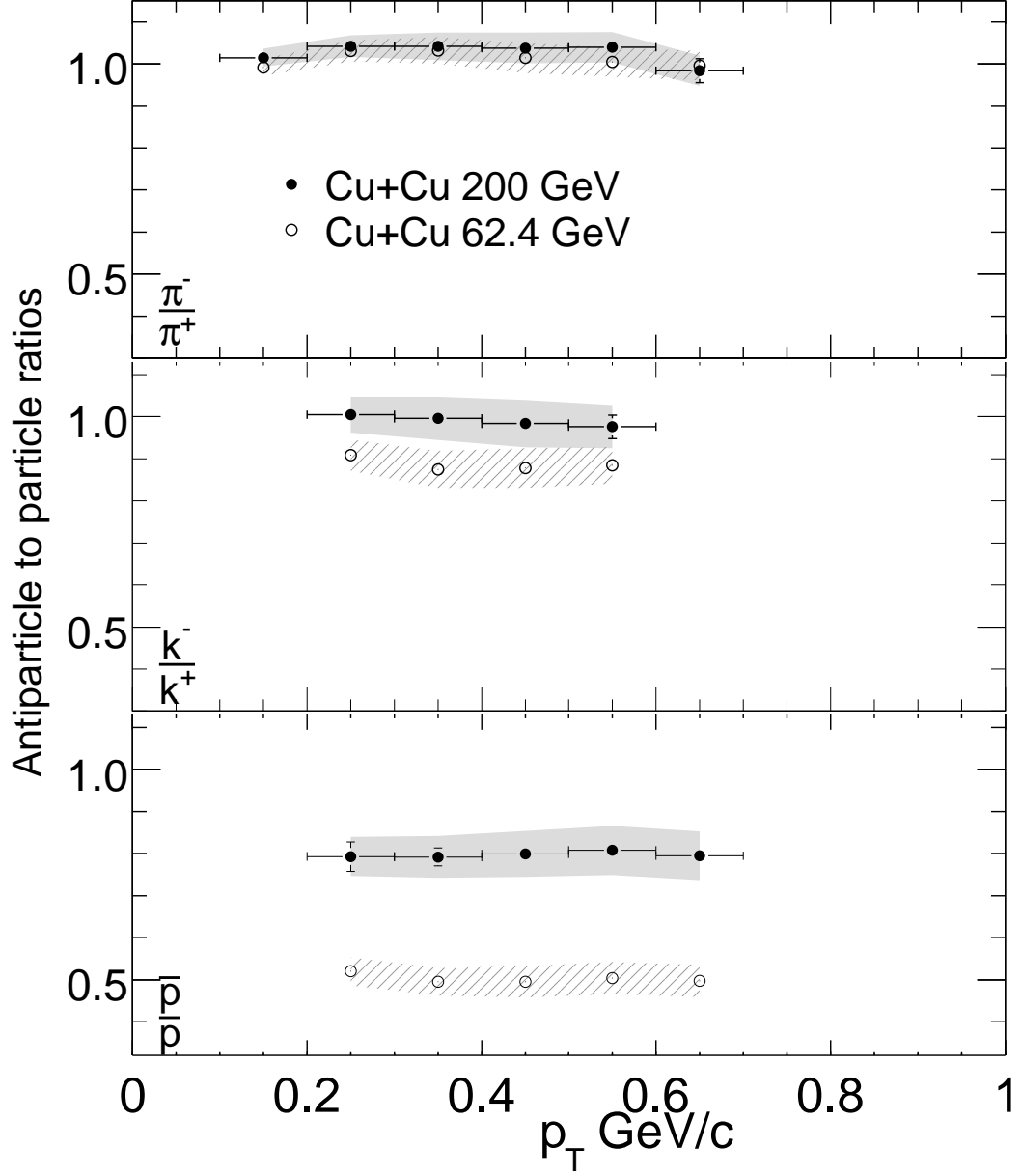


Figure 70. Antiparticle to particle ratios in (0-12% central) Cu+Cu collisions, as a function of the transverse momentum, for pions, kaons and protons. Open (closed) circles represent  $\sqrt{s_{NN}} = 62.4$  GeV (200 GeV) data. The vertical error bars represent the ( $1\sigma$ ) statistical and the band represents systematic uncertainties. The horizontal error bars represent the bin size.

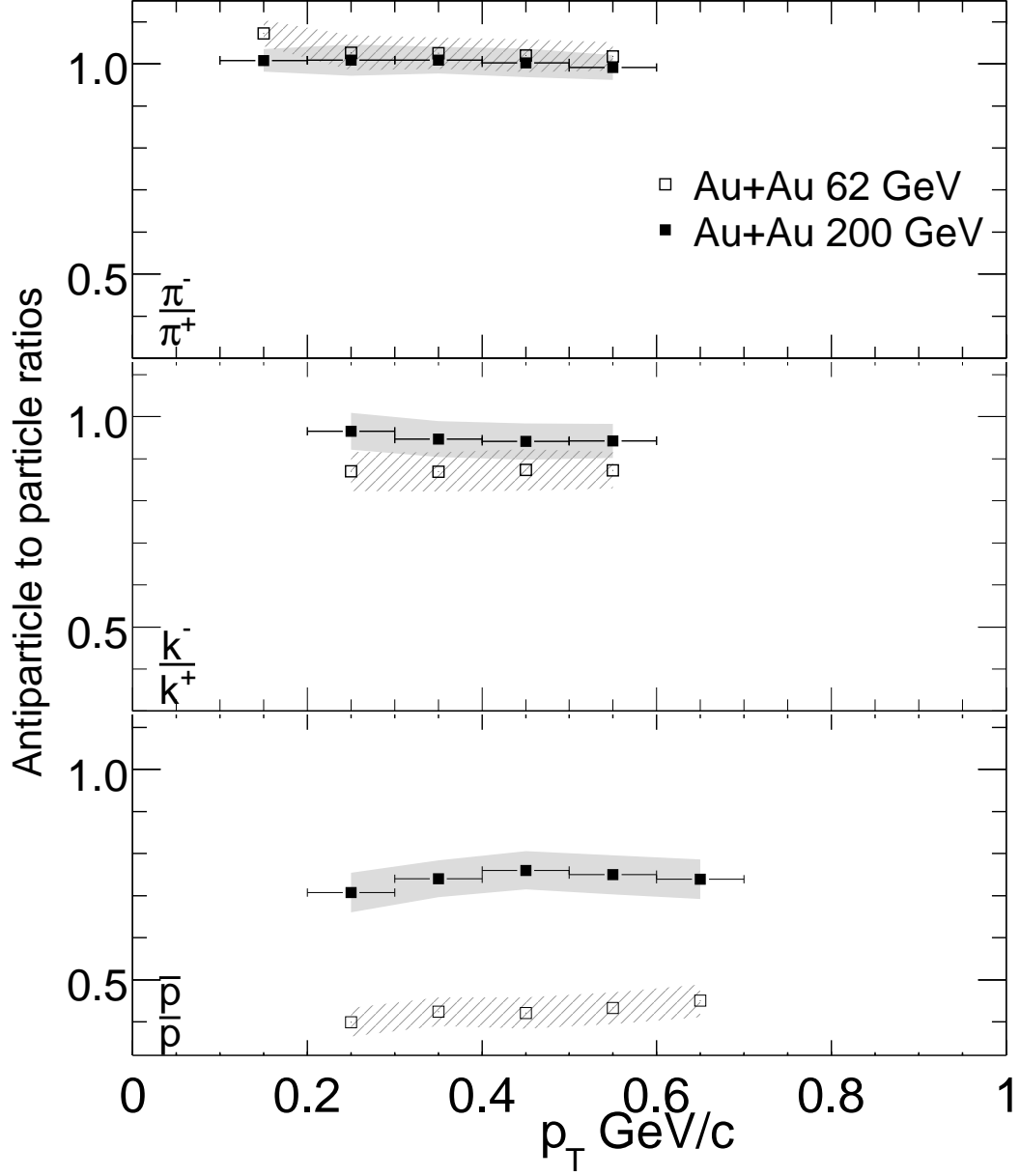


Figure 71. Antiparticle to particle ratios in (0-12% central) Au+Au collisions, as a function of the transverse momentum, for pions, kaons and protons. Open (closed) circles represent  $\sqrt{s_{NN}} = 62.4$  GeV (200 GeV) data. The vertical error bars represent the ( $1\sigma$ ) statistical and the band represents systematic uncertainties. The horizontal error bars represent the bin size.



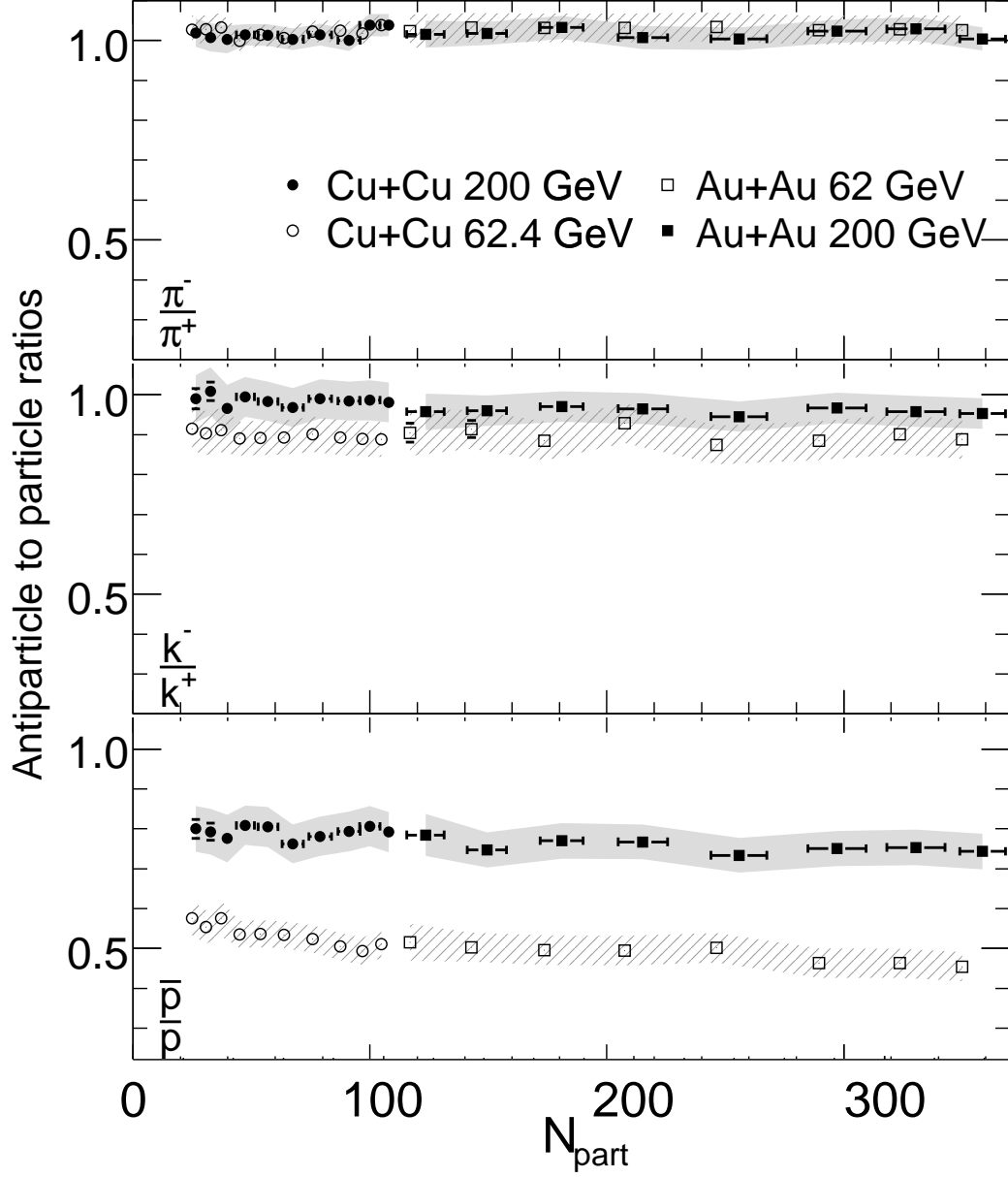


Figure 72. Antiparticle to particle ratios in Cu+Cu collisions, as a function of the number of participants, for pions, kaons and protons. The average transverse momenta of each result is  $\langle p_T \rangle \approx 0.31, 0.36$  and  $0.50$  GeV/c for pions, kaons and protons, respectively. Open (closed) circles represent  $\sqrt{s_{NN}} = 62.4$  GeV (200 GeV) data. The vertical error bars represent the combined ( $1\sigma$ ) statistical and the band represents systematic uncertainties. The horizontal error bars represent uncertainty in determining the number of participants.

TABLE XIV

MEASURED ANTIPARTICLE TO PARTICLE RATIOS AS FUNCTION OF TRANSVERSE MOMENTUM ARE PRESENTED. DATA IS PRESENTED FOR CU+CU 200 GEV, CU+CU 62.4 GEV, AU+AU 200 GEV AND AU+AU 62.4 GEV.

$p_T$ GeV/c	$\langle \bar{p} \rangle / \langle p \rangle$	$\langle K^- \rangle / \langle K^+ \rangle$	$\langle \pi^- \rangle / \langle \pi^+ \rangle$
Cu+Cu 200 GeV			
0.250	$0.79 \pm 0.03 \pm 0.05$	$1.00 \pm 0.01 \pm 0.04$	$1.04 \pm 0.00 \pm 0.03$
0.350	$0.79 \pm 0.02 \pm 0.05$	$1.00 \pm 0.01 \pm 0.05$	$1.04 \pm 0.00 \pm 0.03$
0.450	$0.80 \pm 0.02 \pm 0.05$	$0.98 \pm 0.01 \pm 0.06$	$1.04 \pm 0.00 \pm 0.04$
0.550	$0.81 \pm 0.02 \pm 0.06$	$0.98 \pm 0.03 \pm 0.05$	$1.04 \pm 0.01 \pm 0.04$
0.650	$0.80 \pm 0.02 \pm 0.06$		$0.98 \pm 0.03 \pm 0.04$
Cu+Cu 62 GeV			
0.250	$0.52 \pm 0.01 \pm 0.03$	$0.91 \pm 0.01 \pm 0.04$	$1.03 \pm 0.00 \pm 0.03$
0.350	$0.49 \pm 0.01 \pm 0.03$	$0.87 \pm 0.01 \pm 0.04$	$1.03 \pm 0.00 \pm 0.03$
0.450	$0.50 \pm 0.01 \pm 0.04$	$0.88 \pm 0.01 \pm 0.05$	$1.01 \pm 0.00 \pm 0.04$
0.550	$0.50 \pm 0.01 \pm 0.04$	$0.88 \pm 0.01 \pm 0.04$	$1.00 \pm 0.00 \pm 0.03$
0.650	$0.50 \pm 0.01 \pm 0.04$		$1.00 \pm 0.02 \pm 0.04$
Au+Au 200 GeV			
0.250	$0.71 \pm 0.02 \pm 0.05$	$0.97 \pm 0.01 \pm 0.04$	$1.01 \pm 0.00 \pm 0.04$
0.350	$0.74 \pm 0.01 \pm 0.04$	$0.95 \pm 0.01 \pm 0.04$	$1.01 \pm 0.00 \pm 0.03$
0.450	$0.76 \pm 0.01 \pm 0.05$	$0.94 \pm 0.01 \pm 0.04$	$1.00 \pm 0.00 \pm 0.03$
0.550	$0.75 \pm 0.01 \pm 0.05$	$0.94 \pm 0.01 \pm 0.04$	$0.99 \pm 0.00 \pm 0.03$
0.650	$0.74 \pm 0.01 \pm 0.05$		
Au+Au 62 GeV			
0.250	$0.40 \pm 0.01 \pm 0.03$	$0.87 \pm 0.01 \pm 0.05$	$1.03 \pm 0.00 \pm 0.04$
0.350	$0.42 \pm 0.01 \pm 0.03$	$0.87 \pm 0.01 \pm 0.05$	$1.03 \pm 0.00 \pm 0.04$
0.450	$0.42 \pm 0.01 \pm 0.04$	$0.87 \pm 0.01 \pm 0.05$	$1.02 \pm 0.00 \pm 0.04$
0.550	$0.43 \pm 0.01 \pm 0.04$	$0.87 \pm 0.02 \pm 0.04$	$1.02 \pm 0.01 \pm 0.03$
0.650	$0.45 \pm 0.01 \pm 0.04$		

TABLE XV

CU+CU 200 GEV AND 62.4 GEV RATIOS AS A FUNCTION CENTRALITY. THE UNCERTAINTIES ON  $\langle N_{PART} \rangle$  ARE 90% C.L. SYSTEMATIC AND ON THE RATIOS ARE STANDARD ( $1\sigma$ ) STATISTICAL AND SYSTEMATIC, RESPECTIVELY.

Centrality	$\langle N_{part} \rangle$	$\langle \bar{p} \rangle / \langle p \rangle$	$\langle K^- \rangle / \langle K^+ \rangle$	$\langle \pi^- \rangle / \langle \pi^+ \rangle$
Cu+Cu 200 GeV				
0 – 3%	$106.3 \pm 3.55$	$0.79 \pm 0.01 \pm 0.05$	$0.98 \pm 0.01 \pm 0.05$	$1.04 \pm 0.00 \pm 0.03$
3 – 6%	$100.3 \pm 4.30$	$0.81 \pm 0.01 \pm 0.05$	$0.99 \pm 0.01 \pm 0.05$	$1.04 \pm 0.00 \pm 0.03$
6 – 10%	$91.3 \pm 4.68$	$0.79 \pm 0.01 \pm 0.05$	$0.98 \pm 0.01 \pm 0.05$	$1.00 \pm 0.00 \pm 0.03$
10 – 15%	$79.3 \pm 4.76$	$0.78 \pm 0.01 \pm 0.05$	$0.99 \pm 0.01 \pm 0.05$	$1.01 \pm 0.00 \pm 0.03$
15 – 20%	$67.3 \pm 4.49$	$0.76 \pm 0.01 \pm 0.05$	$0.97 \pm 0.01 \pm 0.05$	$1.00 \pm 0.00 \pm 0.03$
20 – 25%	$57.3 \pm 4.18$	$0.80 \pm 0.02 \pm 0.05$	$0.98 \pm 0.02 \pm 0.05$	$1.01 \pm 0.00 \pm 0.03$
25 – 30%	$47.3 \pm 3.78$	$0.81 \pm 0.02 \pm 0.05$	$0.99 \pm 0.02 \pm 0.05$	$1.01 \pm 0.00 \pm 0.03$
30 – 35%	$30.3 \pm 3.43$	$0.78 \pm 0.02 \pm 0.06$	$0.97 \pm 0.02 \pm 0.06$	$1.00 \pm 0.00 \pm 0.03$
35 – 40%	$33.3 \pm 3.15$	$0.79 \pm 0.02 \pm 0.06$	$1.01 \pm 0.02 \pm 0.06$	$1.01 \pm 0.00 \pm 0.04$
40 – 45%	$27.3 \pm 2.87$	$0.80 \pm 0.02 \pm 0.06$	$0.99 \pm 0.03 \pm 0.06$	$1.02 \pm 0.01 \pm 0.04$
Cu+Cu 62 GeV				
0 – 3%	$102.3 \pm 3.62$	$0.51 \pm 0.01 \pm 0.03$	$0.89 \pm 0.01 \pm 0.04$	$1.04 \pm 0.00 \pm 0.03$
3 – 6%	$95.3 \pm 4.38$	$0.49 \pm 0.00 \pm 0.03$	$0.89 \pm 0.01 \pm 0.04$	$1.02 \pm 0.00 \pm 0.03$
6 – 10%	$88.3 \pm 4.78$	$0.50 \pm 0.00 \pm 0.03$	$0.89 \pm 0.01 \pm 0.04$	$1.02 \pm 0.00 \pm 0.03$
10 – 15%	$76.3 \pm 4.79$	$0.52 \pm 0.01 \pm 0.03$	$0.90 \pm 0.01 \pm 0.04$	$1.02 \pm 0.00 \pm 0.03$
15 – 20%	$65.3 \pm 4.38$	$0.53 \pm 0.01 \pm 0.03$	$0.89 \pm 0.01 \pm 0.04$	$1.01 \pm 0.00 \pm 0.03$
20 – 25%	$55.3 \pm 4.04$	$0.54 \pm 0.01 \pm 0.03$	$0.89 \pm 0.01 \pm 0.04$	$1.01 \pm 0.00 \pm 0.03$
25 – 30%	$47.3 \pm 3.74$	$0.53 \pm 0.01 \pm 0.03$	$0.89 \pm 0.01 \pm 0.04$	$1.00 \pm 0.00 \pm 0.03$
30 – 35%	$38.3 \pm 3.39$	$0.58 \pm 0.01 \pm 0.04$	$0.91 \pm 0.01 \pm 0.05$	$1.03 \pm 0.00 \pm 0.04$
35 – 40%	$32.3 \pm 3.08$	$0.55 \pm 0.01 \pm 0.04$	$0.90 \pm 0.01 \pm 0.05$	$1.03 \pm 0.00 \pm 0.04$
40 – 45%	$25.3 \pm 2.80$	$0.58 \pm 0.01 \pm 0.04$	$0.91 \pm 0.01 \pm 0.05$	$1.03 \pm 0.00 \pm 0.04$

TABLE XVI

AU+AU 200 GEV AND 62.4 GEV ANTIPARTICLE TO PARTICLE RATIOS AS A FUNCTION CENTRALITY. THE UNCERTAINTIES ON  $\langle N_{PART} \rangle$  ARE 90% C.L. SYSTEMATIC AND ON THE RATIOS ARE STANDARD ( $1\sigma$ ) STATISTICAL AND SYSTEMATIC, RESPECTIVELY.

Centrality	$\langle N_{part} \rangle$	$\langle \bar{p} \rangle / \langle p \rangle$	$\langle K^- \rangle / \langle K^+ \rangle$	$\langle \pi^- \rangle / \langle \pi^+ \rangle$
Au+Au 200 GeV				
0 – 3%	$361 \pm 11$	$0.74 \pm 0.01 \pm 0.04$	$0.95 \pm 0.01 \pm 0.04$	$1.00 \pm 0.00 \pm 0.03$
3 – 6%	$331 \pm 10$	$0.75 \pm 0.01 \pm 0.04$	$0.96 \pm 0.01 \pm 0.04$	$1.03 \pm 0.00 \pm 0.03$
6 – 10%	$297 \pm 9$	$0.75 \pm 0.01 \pm 0.04$	$0.97 \pm 0.01 \pm 0.04$	$1.02 \pm 0.00 \pm 0.03$
10 – 15%	$255 \pm 8$	$0.73 \pm 0.01 \pm 0.04$	$0.95 \pm 0.01 \pm 0.04$	$1.00 \pm 0.00 \pm 0.03$
15 – 20%	$215 \pm 7$	$0.77 \pm 0.01 \pm 0.04$	$0.97 \pm 0.01 \pm 0.04$	$1.01 \pm 0.00 \pm 0.03$
20 – 25%	$180 \pm 7$	$0.77 \pm 0.01 \pm 0.04$	$0.97 \pm 0.01 \pm 0.04$	$1.03 \pm 0.00 \pm 0.03$
25 – 30%	$150 \pm 6$	$0.75 \pm 0.01 \pm 0.04$	$0.96 \pm 0.01 \pm 0.04$	$1.02 \pm 0.00 \pm 0.03$
30 – 35%	$124 \pm 6$	$0.78 \pm 0.01 \pm 0.05$	$0.96 \pm 0.01 \pm 0.05$	$1.02 \pm 0.00 \pm 0.03$
Au+Au 62 GeV				
0 – 3%	$349 \pm 11$	$0.45 \pm 0.01 \pm 0.04$	$0.89 \pm 0.02 \pm 0.05$	$1.03 \pm 0.00 \pm 0.04$
3 – 6%	$325 \pm 10$	$0.46 \pm 0.01 \pm 0.04$	$0.90 \pm 0.02 \pm 0.05$	$1.03 \pm 0.00 \pm 0.04$
6 – 10%	$288 \pm 9$	$0.46 \pm 0.01 \pm 0.04$	$0.88 \pm 0.02 \pm 0.05$	$1.03 \pm 0.00 \pm 0.04$
10 – 15%	$248 \pm 8$	$0.50 \pm 0.01 \pm 0.04$	$0.87 \pm 0.02 \pm 0.05$	$1.03 \pm 0.00 \pm 0.04$
15 – 20%	$209 \pm 7$	$0.49 \pm 0.01 \pm 0.04$	$0.93 \pm 0.02 \pm 0.05$	$1.03 \pm 0.00 \pm 0.04$
20 – 25%	$174 \pm 13$	$0.50 \pm 0.01 \pm 0.04$	$0.88 \pm 0.02 \pm 0.05$	$1.03 \pm 0.00 \pm 0.04$
25 – 30%	$140 \pm 10$	$0.50 \pm 0.02 \pm 0.04$	$0.91 \pm 0.02 \pm 0.05$	$1.03 \pm 0.01 \pm 0.04$

TABLE XVII

STRAIGHT LINE FITS TO THE RATIOS AS A FUNCTION OF NUMBER OF PARTICIPANTS FOR 200 GEV AND 62.4 GEV DATA. THE FITS ARE OBTAINED BY COMBINING BOTH THE CU+CU DATA AND AU+AU DATA.

	200 GeV		62.4 GeV	
	Intercept	Slope	Intercept	Slope
pions	$1.015 \pm 0.0120$	$0.000008 \pm 0.000067$	$1.017 \pm 0.0122$	$0.000044 \pm 0.000080$
Kaons	$0.988 \pm 0.0208$	$-0.000105 \pm 0.000102$	$0.810 \pm 0.0194$	$-0.000026 \pm 0.000118$
Protons	$0.800 \pm 0.0215$	$-0.000173 \pm 0.000112$	$0.550 \pm 0.0150$	$-0.000282 \pm 0.000090$

## 9.2 Interpretation

### 9.2.1 Observation

#### Dependence of ratios on Transverse momentum

Antiparticle to particle ratios as a function of transverse momentum are presented in Figure 70 for Cu+Cu data and Figure 71 for Au+Au data at mid-rapidity for the top 12% central collisions. There is no strong dependence on the transverse momentum outside of the systematic error for the available kinematic region. For the protons ratio in Au+Au 200 GeV, there is a slight decrease in ratio for the 0.2 GeV transverse momentum bin, still within the systematic error.

#### Dependence of ratios on centrality

Antiparticle to particle ratios as a function of centrality are presented in Figure 72 for Cu+Cu data and Au+Au data at mid-rapidity. The number participants for Cu+Cu collisions

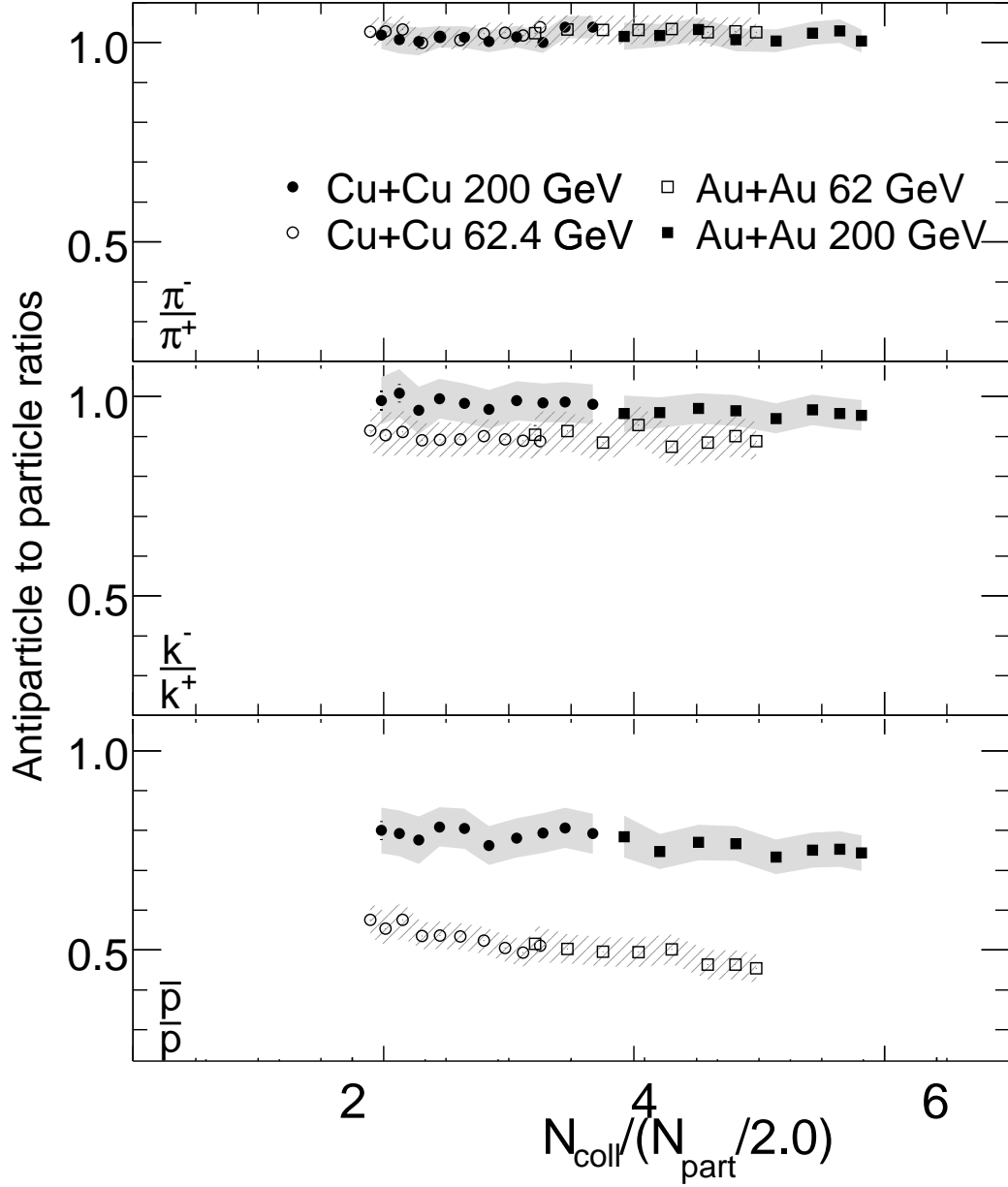


Figure 73. Antiparticle to particle ratios in Cu+Cu collisions, as a function of the number of collisions per participant pair, for pions, kaons and protons. Open (closed) circles represent  $\sqrt{s_{NN}} = 62.4$  GeV (200 GeV) data. The vertical error bars represent the combined ( $1\sigma$ ) statistical and the band represents systematic uncertainties.

varies from 25(peripheral) to 106(central), and for Au+Au data 124(peripheral) to 361(central). To quantify the effect of centrality of collision, straight line fits to the combined Cu+Cu and Au+Au data versus  $N_{part}$  are obtained. A quadratic sum of both the systematic error and the statistical error is considered for the fitting. Fits are obtained separately for 200 GeV data and 62.4 GeV data. The fit values are summarized in the Table XVII for pions, kaons and protons. From the fit values and the errors, the following conclusions can be made

- For pions, the slope value for both 200 GeV data and 62.4 GeV data is consistent with in the error to be equal to zero. Hence, there is no dependence pion ratios as a function of centrality within the current systematic uncertainties.
- For kaons, the slope for 200 GeV data has negligible but non-zero value which allows for a small variation of the kaon ratios as function of centrality. The slope for 62.4 GeV data is consistent with zero.
- For protons, both 200 GeV data and 62.4 GeV fits to the data have non-zero non-negligible slope. The change in the value of ratios from the fit going from 25 participants (peripheral Cu+Cu) to 361 participants (central Au+Au) with a slope of -0.000173 corresponds to a decrease in the ratio of -0.06 for 200 GeV data, which is larger than the average systematic error of 0.05 on data itself. Similarly for 62.4 GeV data, for a slope of -0.000282, the decrease in the ratio is 0.09 which is greater than the average systematic error of 0.04. This indicates there is a small dependence (decrease) of the ratios as function of centrality (i.e. number of participants).

- For fun, in Figure 73 is the ratios as a function of number of collisions per participant pair. The individual slopes of the curves obtained from Au+Au data and Cu+Cu data seems to be more in agreement than the individual slopes with the Figure 72. In so far this improved agreement indicates a more universal trend across both systems, this could be taken to imply that this quantity  $N_{coll}(N_{part}/2.0)$  is more relevant physical quantity in determining the ratios for heavy ion collisions.



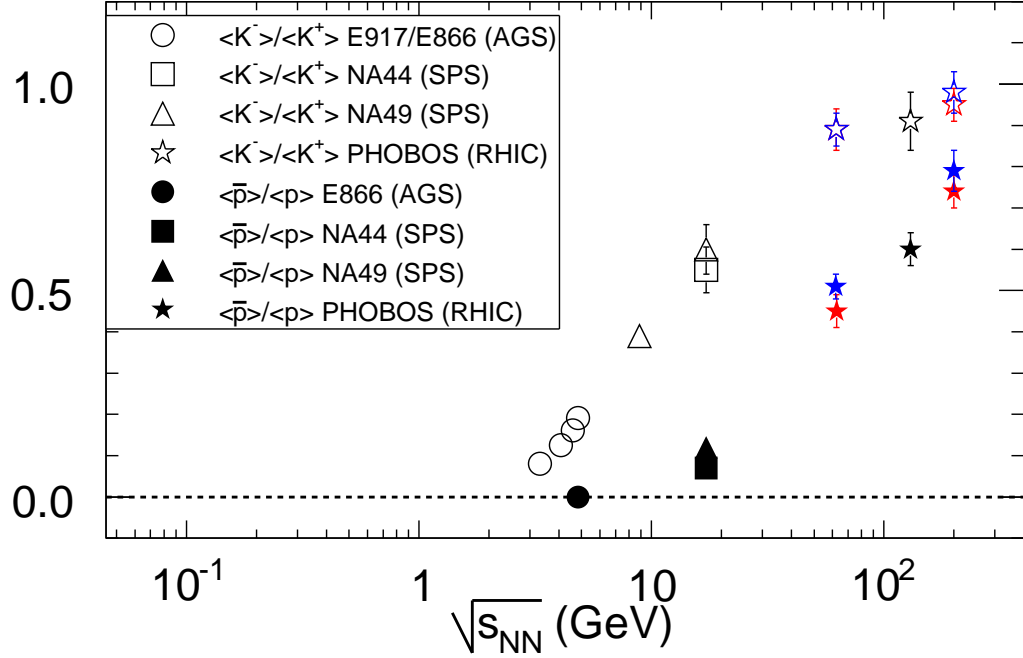


Figure 74.  $\langle \bar{p} \rangle / \langle p \rangle$  and  $\langle K^- \rangle / \langle K^+ \rangle$  ratios for central heavy ion collisions are shown as a function of par nucleon center-of-mass energy. The colored makers represent the data from this thesis, Au+Au in red and Cu+Cu in blue. A large increase in  $\langle \bar{p} \rangle / \langle p \rangle$  is seen between the lower energy AGS and SPS data and RHIC data suggesting a significant step towards producing collisions nearly free of baryons near mid-rapidity.

### Dependence of ratios on collision center-of-mass energy

In Figure 74 plotted is the Kaon and Proton ratios as function of center of mass energy for various experiments( (25), (26), (27), (28), (29)), heavy ion collisions. Kaon and proton ratio increases strongly with the center of mass energy at mid-rapidity. The red and blue markers are the results obtained in this thesis. They continue the trend towards unity observed in the measurements at lower energy. The previously measured single PHOBOS Au+Au 130 GeV

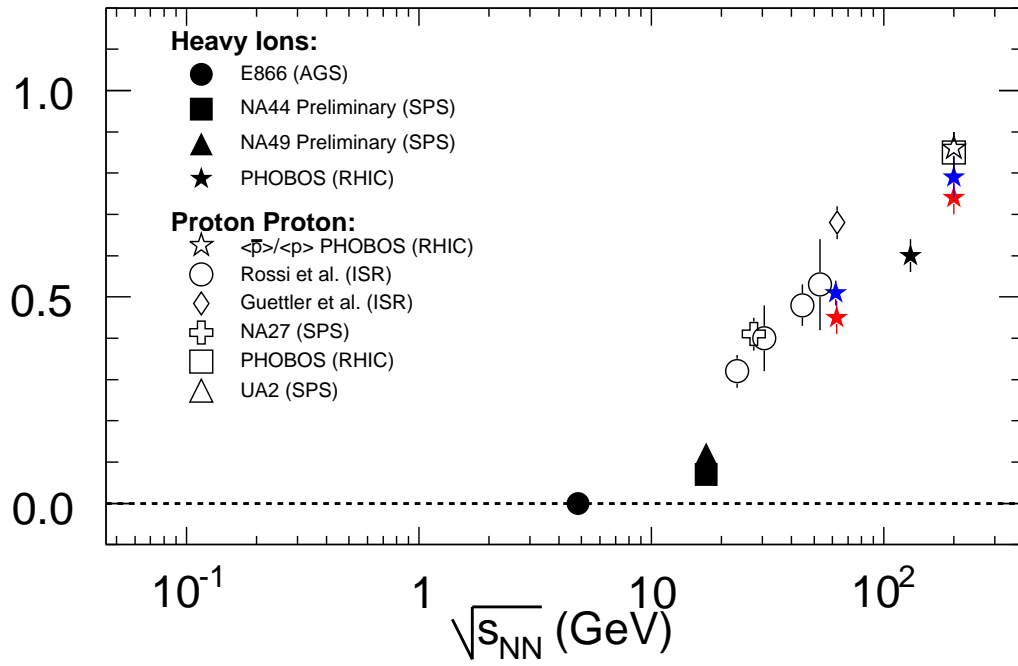


Figure 75.  $\langle \bar{p} \rangle / \langle p \rangle$  are shown as a function of center of mass energy. The colored markers represent the data from this thesis, Au+Au in red and Cu+Cu in blue. The black markers represent p+p data from various experiments in (open symbols), central Pb+Pb (solid star and triangle).

data points, in particular the kaons, appear to be slightly lower in value as compared to the trend seen from the neighboring points, but still well within the systematics. It is interesting to note that the kaon ratios are observed to have essentially reached unity over this energy range. In Figure 75 plotted is the proton ratios as a function of center of mass energy, for both proton collisions and the heavy ion collisions. Proton ratios in heavy ion collisions are consistently lower when compared to proton-proton collisions.

### Systematic comparison with other experiments at RHIC

	$\bar{p}/p$	$K^-/K^+$	$\pi^-/\pi^+$
PHENIX (Au+Au)	$0.73 \pm 0.01 \pm 0.06$	$0.93 \pm 0.01 \pm 0.05$	$0.98 \pm 0.00 \pm 0.06$
PHOBOS (Au+Au)	$0.73 \pm 0.02 \pm 0.03$	$0.93 \pm 0.05 \pm 0.03$	$0.99 \pm 0.14$
BRAHMS (Au+Au)	$0.75 \pm 0.04 \pm 0.03$	$0.94 \pm 0.08$	<b><math>0.99 \pm 0.00 \pm 0.03</math></b>
STAR (Au+Au)	$0.77 \pm 0.05 \pm 0.08$	$0.95 \pm 0.03 \pm 0.03$	$1.00 \pm 0.01 \pm 0.02$
<b>PHOBOS (Cu+Cu)</b>	<b><math>0.77 \pm 0.01 \pm 0.05</math></b>	$0.95 \pm 0.05 \pm 0.04$	$1.01 \pm 0.01 \pm 0.04$
BRAHMS (p+p)	$0.78 \pm 0.03 \pm 0.06$	$0.97 \pm 0.05 \pm 0.07$	$1.02 \pm 0.01 \pm 0.07$
STAR (p+p)	$0.83 \pm 0.01 \pm 0.08$	$0.97 \pm 0.03 \pm 0.10$	$1.02 \pm 0.00 \pm 0.01$
PHOBOS (p+p)	$0.85 \pm 0.04 \pm 0.03$	<b><math>0.98 \pm 0.01 \pm 0.03</math></b>	$1.03 \pm 0.01 \pm 0.02$

Figure 76. Antiparticle to particle ratios for protons, kaons and pions in  $\sqrt{s_{NN}} = 200$  GeV p+p and central Au+Au collisions from RHIC, compared to the result for central Cu+Cu collisions (bold). When available, errors are reported as statistical and systematic, respectively. Values rounded to the shown (reasonable) precision, where a zero value of the statistical uncertainty indicates the actual value is less than 0.004. The central bin for heavy ion data varies from 0-5% to 0-12%, depends on the specific experiment and data set. Lines between the columns connect the specific data points to their associated experiment. See text for more detailed discussion.

To understand the global systematics of a measurement, its important to compare any new result with all recent published data by other experiments. Presented in this section is such a comparison with other published results from all experiments at RHIC. This thesis contains the only available results for Cu+Cu, as no other data has been published. Therefore a comparison between the new results are made to p+p and Au=Au collisions at 200 GeV, (30), (31), (32), (33), (34), (35), (36). This compilation is shown in Figure 76, where the graphic is designed to clearly and precisely illustrate the current state of the data. In particular the data in each particle ratios column is arranged from the smallest to largest values, with the associated available errors, to enable quantitative relative comparisons. Lines between columns connect each result to its associated experiment, the slopes of which also allow for an immediate comparison of how and where each measurement falls within the current “world” average. We find that our particle ratios result for central Cu+Cu collisions at 200 GeV is consistent within uncertainties to that found in 200 GeV p+p and central Au+Au collisions near mid-rapidity. It is interesting to note as an aside that the Cu+Cu result for protons is also in reasonable agreement with the PHOBOS results for d+Au collisions at 200 GeV, which found values of  $\langle \bar{p} \rangle / \langle p \rangle$  in the range of 0.80-0.84 (with similar systematics) that were independent of centrality, or more precisely the number of collisions per deuteron participant (?). Thus, within the current level of systematics and all available data, we find that the colliding system size appears to play a minor role in determining the final particle ratios of low  $\langle p_T \rangle$  pions, kaons and protons, and hence also in many of the thermal properties of the collision zone. As mentioned earlier, when looking solely at PHOBOS results, slight centrality dependence of the proton ratios is

observed indicating that there may be a small systematic shift to lower values as the system size increases<sup>1</sup>.

### 9.2.2 Discussion

At RHIC energies, the  $\langle\pi^- \rangle / \langle\pi^+ \rangle$  ratio is independent of transverse momentum, collision centrality, collision center of mass energy or collision species, within the precision of the measurement. Pions are the lightest of the mesons (formed by combination of light quarks) and are produced in abundance in heavy ion collisions. They form the bulk of the soft particles produced.

The  $\langle\bar{p}\rangle/\langle p\rangle$  and  $\langle K^- \rangle/\langle K^+ \rangle$  ratios depend on the collision energy as shown in Figure 74 and Figure 75. Unlike pions, the kaon and proton ratios values are measurably affected by the initial baryon density. As the center-of-mass energy increases, the mid-rapidity region of the collisions tend to be more baryon free. The contribution for the final baryons can be thought of as coming from the transported baryons  $Y_{trans}$  and pair production  $Y_{pair-prod}$  via pair production in the created medium. Since there are no net anti-baryon to begin with, anti-baryons should be entirely produced. From the deviation of the particle ratios from unity, a relative measure of the fraction of initial baryons to pair production can be estimated.

$$Ratio = \frac{\overline{Y_{pairprod}}}{Y_{pair-prod} + Y_{trans}} \quad (9.6)$$

---

<sup>1</sup>The advantage of performing more detailed comparison with a same detector has a reduced sensitivity to additional systematic uncertainties that often arise between different experiments.

$$\frac{Y_{trans}}{Y_{pair-prod}} = \frac{1.0}{Ratio} - 1.0 \quad (9.7)$$

For 200 GeV collisions, the relative fraction of the transported baryons to pair produced baryons changes from 0.36 for the most central Au+Au collisions ( $N_{part} = 361$ ) to 0.23 for most peripheral Cu+Cu collisions ( $N_{part} = 327$ ). For 62.4 GeV collisions the relative fraction of transported baryons changes from 1.2 for central Au+Au collisions ( $N_{part} = 349$ ) to 0.72 for peripheral Cu+Cu collisions ( $N_{part} = 25$ ). For 62.4 GeV data, the change from a larger transported baryon contribution to a larger pair produced baryon contribution occurs at around 214 participants (calculated from the fits). From the plot, Figure 72, this change appears to occur smoothly for 62.4 GeV, as no sudden deviation in the ratios is observed as a function of  $N_{part}$ . For 200 GeV data, the relative fraction of transported baryon is always less than unity and also changes significantly less across the same centrality ( $N_{part}$ ) range. For a given center-of-mass energy, more participants in a given collision increases the probability that the initial baryons will be transported to the final state.

Kaon production also depends on the initial baryon density. For example in associated production mechanism  $K^+(u\bar{s})$  and  $\Lambda(uus)$  are produced from a proton ( $uud$ ) and a ( $s\bar{s}$ ) pair. As a result in a region of non-zero baryon density, the probability of producing a  $K^+$  is larger than the probability of producing  $K^-$ . A likely explanation for why the kaon ratios reaches unity much faster as with collisions energy than the proton ratios, as not all the transported baryons are available for kaon production.

TABLE XVIII

SUMMARY OF THE MEASURED BARYOCHEMICAL POTENTIAL FOR CU+CU 200 GEV, CU+CU 62.4 GEV, AU+AU 200 GEV AND AU+AU 62.4 GEV IS TABULATED. REFER TO TEXT FOR MORE DISCUSSION.

System	$N_{Part}$	$T_{ch}(GeV/c)$	$\mu_B/T$ (MeV/c)
Cu+Cu 200 GeV	106	153	18
Au+Au 200 GeV	361	157	23
Cu+Cu 62.4 GeV	102	151	50
Au+Au 62.4 GeV	349	155	61

Thermal models, as explained in section 2, typically have six free parameters. To determine all the parameters, a measurement of unlike charged particle ratios is also needed. The data for unlike charged particle ratios is available for Au+Au (from other experiments) but not for Cu+Cu data which is the focus of this thesis. None the less the data of this thesis allows for a first estimate of the parameter  $\mu_B/T$  by considering the particle production using the fermi-dirac statistics and neglecting strangeness,

$$\frac{\langle \bar{Y} \rangle}{\langle Y \rangle} = \frac{\int_0^\infty \frac{p^2 dp}{e^{(\sqrt{p^2+m^2}+\mu_B)/T} + 1}}{\int_0^\infty \frac{p^2 dp}{e^{(\sqrt{p^2+m^2}-\mu_B)/T} + 1}} \simeq \frac{e^{-\mu_B/T} \int_0^\infty p^2 e^{-\sqrt{p^2+m^2}/T} dp}{e^{\mu_B/T} \int_0^\infty p^2 e^{-\sqrt{p^2+m^2}/T} dp} = e^{-2\mu_B/T} \quad (9.8)$$

$$\mu_B/T = -0.5 \ln(\langle \bar{Y} \rangle / \langle Y \rangle) \quad (9.9)$$

Using the proton ratios from this thesis,  $\mu_B/T$  is 0.11 for central Cu+Cu 200 GeV collisions and 0.25 for central Cu+Cu 62.4 GeV collision. Using the preliminary chemical freeze-out temperature  $T_{ch}$  estimates of ??, presented in Table XVIII, is the tabulation of the measured  $\mu_B$  values from the above equation. As the baryochemical potential is also measure of the initial baryon density, the argument from the previous baryon transport results also applies here.

### 9.3 Conclusion

Antiparticle to particle ratios of protons, kaons and pions in Cu+Cu and Au+Au collisions at 200 GeV and 62.4 GeV data are presented in this thesis. The results of the Cu+Cu data are the first published data at RHIC[needs reference]. A careful measurement of the dependence of particle ratios as a function of centrality is made. Pion ratios are consistent with unity for both collision energies and independent of centrality within the given precision of the measurement. This is as expected from previous measurement. Kaon ratios and proton ratios are different for different collision energies. This is in agreement with expectation, because at higher energy collisions the mid-rapidity region should be increasingly baryon free. This is also consistent with the previous experimental results found in Au+Au collisions from similar energy ranges.

The kaon and proton particle ratios in Cu+Cu collisions vary slightly outside of systematic error as function of increasing number of participants. The study of the ratios in Cu+Cu is extended to higher participants from a new, detailed, analysis of the Au+Au collisions. A similar systematic dependence of the ratios as a function of participants is observed even in Au+Au. For given energy, a study of the ratios with combined Cu+Cu and Au+Au data set shows that peripheral collisions tend to be more baryon free than the central collisions. In



addition, detailed comparison between Cu+Cu and Au+Au indicates a more unified description of this centrality dependence is possible when using the number of collisions per participant pair as the “measure” of centrality.

A study of baryochemical potential is also presented. A preliminary value of (STAR data)  $T_{ch}$  is used to obtain the baryochemical potential by neglecting the strangeness sector. A lower value of baryochemical is obtained for Cu+Cu 200 GeV data compared to Cu+Cu 62.4 GeV data. These estimates of the baryochemical potential agrees with the expectations for Cu+Cu data and published Au+Au data.

The Large Hadron Collider is expected to deliver Pb+Pb collisions at 5500 GeV center-of-mass energy in late 2009. Extrapolation can be made from lower energy experiments at AGS, SPS and now RHIC, which are backed by the theoretical models that have been tested in each respective energy region. These extrapolations suggest we will be exploring a low baryochemical potential and higher temperature phase space than ever before.

## APPENDICES

## CHAPTER 10

### PHOBOS COLLABORATION

B.Alver<sup>4</sup>, B.B.Back<sup>1</sup>, M.D.Baker<sup>2</sup>, M.Ballintijn<sup>4</sup>, D.S.Barton<sup>2</sup>, R.R.Betts<sup>6</sup>, R.Bindel<sup>7</sup>, W.Busza<sup>4</sup>,  
Z.Chai<sup>2</sup>, V.Chetluru<sup>6</sup>, E.García<sup>6</sup>, T.Gburek<sup>3</sup>, K.Gulbrandsen<sup>4</sup>, J.Hamblen<sup>8</sup>, I.Harnarine<sup>6</sup>, C.Henderson<sup>4</sup>,  
D.J.Hofman<sup>6</sup>, R.S.Hollis<sup>6</sup>, R.Hołyński<sup>3</sup>, B.Holzman<sup>2</sup>, A.Iordanova<sup>6</sup>, J.L.Kane<sup>4</sup>, P.Kulinich<sup>4</sup>,  
C.M.Kuo<sup>5</sup>, W.Li<sup>4</sup>, W.T.Lin<sup>5</sup>, C.Loizides<sup>4</sup>, S.Manly<sup>8</sup>, A.C.Mignerey<sup>7</sup>, R.Nouicer<sup>2</sup>, A.Olszewski<sup>3</sup>,  
R.Pak<sup>2</sup>, C.Reed<sup>4</sup>, E.Richardson<sup>7</sup>, C.Roland<sup>4</sup>, G.Roland<sup>4</sup>, J.Sagerer<sup>6</sup>, I.Sedykh<sup>2</sup>, C.E.Smith<sup>6</sup>,  
M.A.Stankiewicz<sup>2</sup>, P.Steinberg<sup>2</sup>, G.S.F.Stephans<sup>4</sup>, A.Sukhanov<sup>2</sup>, A.Szostak<sup>2</sup>, M.B.Tonjes<sup>7</sup>, A.Trzupek<sup>3</sup>,  
G.J.van Nieuwenhuizen<sup>4</sup>, S.S.Vaurynovich<sup>4</sup>, R.Verdier<sup>4</sup>, G.I.Veres<sup>4</sup>, P.Walters<sup>8</sup>, E.Wenger<sup>4</sup>,  
D.Willhelm<sup>7</sup>, F.L.H.Wolfs<sup>8</sup>, B.Wosiek<sup>3</sup>, K.Woźniak<sup>3</sup>, S.Wyngaardt<sup>2</sup>, B.Wysłouch<sup>4</sup>

## CHAPTER 11

### DEFINITIONS

Collisions vertex :

Min-bias data :

Minimum Ionizing Particle (MIP):

Distance of closest approach (DCA):

## CHAPTER 12

### DATA TAGS

#### Data Tags

##### **Cu+Cu 200GeV**

16590-16831 (Ants,PASS00\_ONLV\_6\_0\_9)

##### **Cu+Cu 62GeV**

18480-18744 (Ants,PASS00\_ONLV\_6\_0\_9)

##### **Au+Au 200GeV**

13739-14216 (Ants,PASS00\_ONLV\_5\_0\_16)

##### **Au+Au 62GeV**

14472-14598 (Ants,PASS01\_ONLV\_5\_1\_0)

#### **12.1 Centrality selection**

##### **Cu+Cu 200GeV**

- TrgCuts.PR05\_200CuCu\_BP\_DCMEOct
- TrgCuts.PR05\_200CuCu\_BM\_DCMEOct

##### **Cu+Cu 62GeV**

- TrgCuts.PR05\_62CuCu\_BP\_DCMEOct\_0pt750
- TrgCuts.PR05\_62CuCu\_BM\_DCMEOct\_0pt750

**Au+Au 200GeV**

- TrgCuts\_PR04\_200\_BP
- TrgCuts\_PR04\_200\_BM

**Au+Au 200GeV**

- TrgCuts\_PR04\_63\_BP
- TrgCuts\_PR04\_63\_BM

## CHAPTER 13

### PARTICLE IDENTIFICATION AND RAW RATIOS - ADDITIONAL PLOTS

Fit functions for improved statistical technique

Raw ratios using method-I

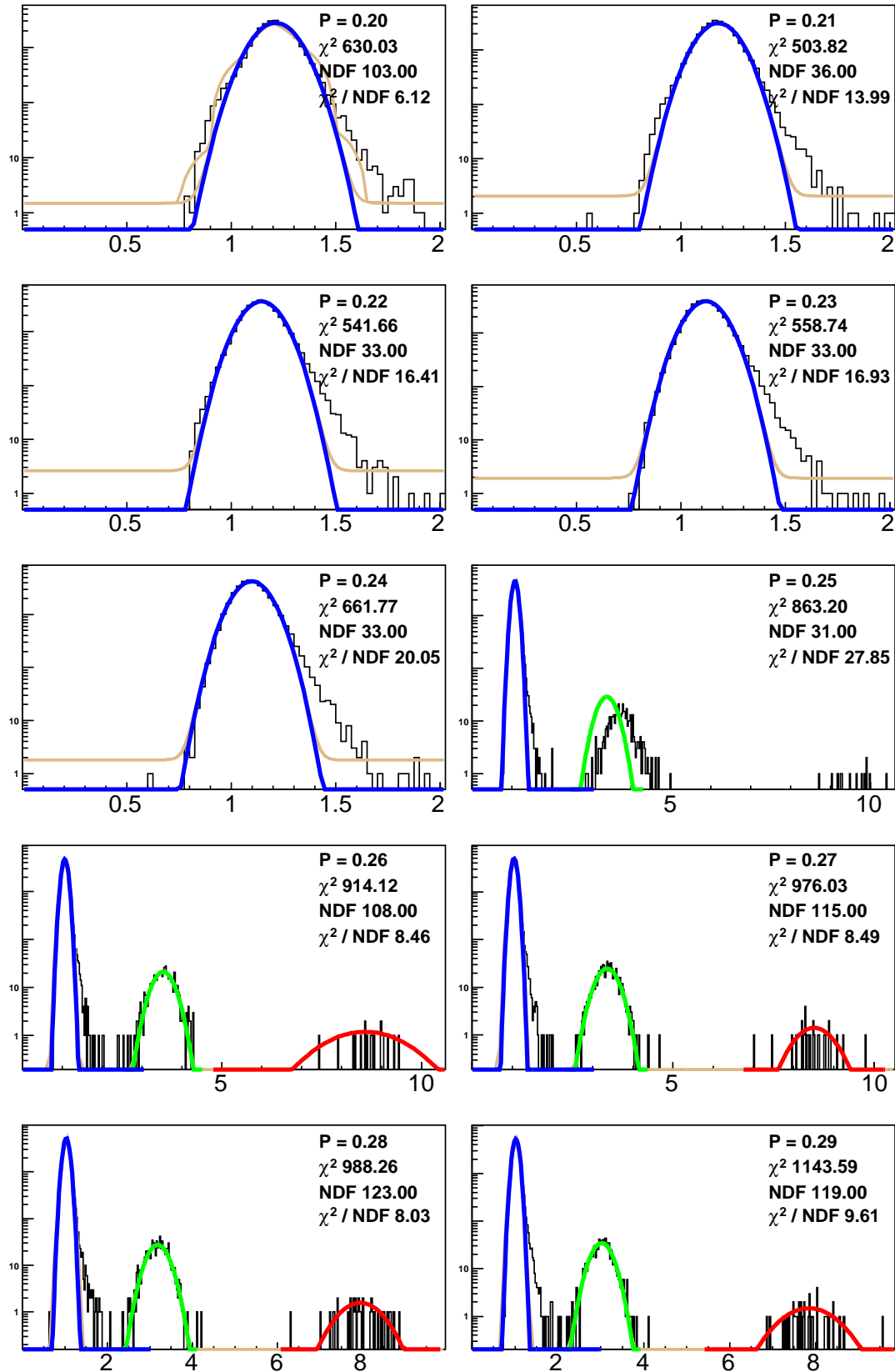


Figure 77.



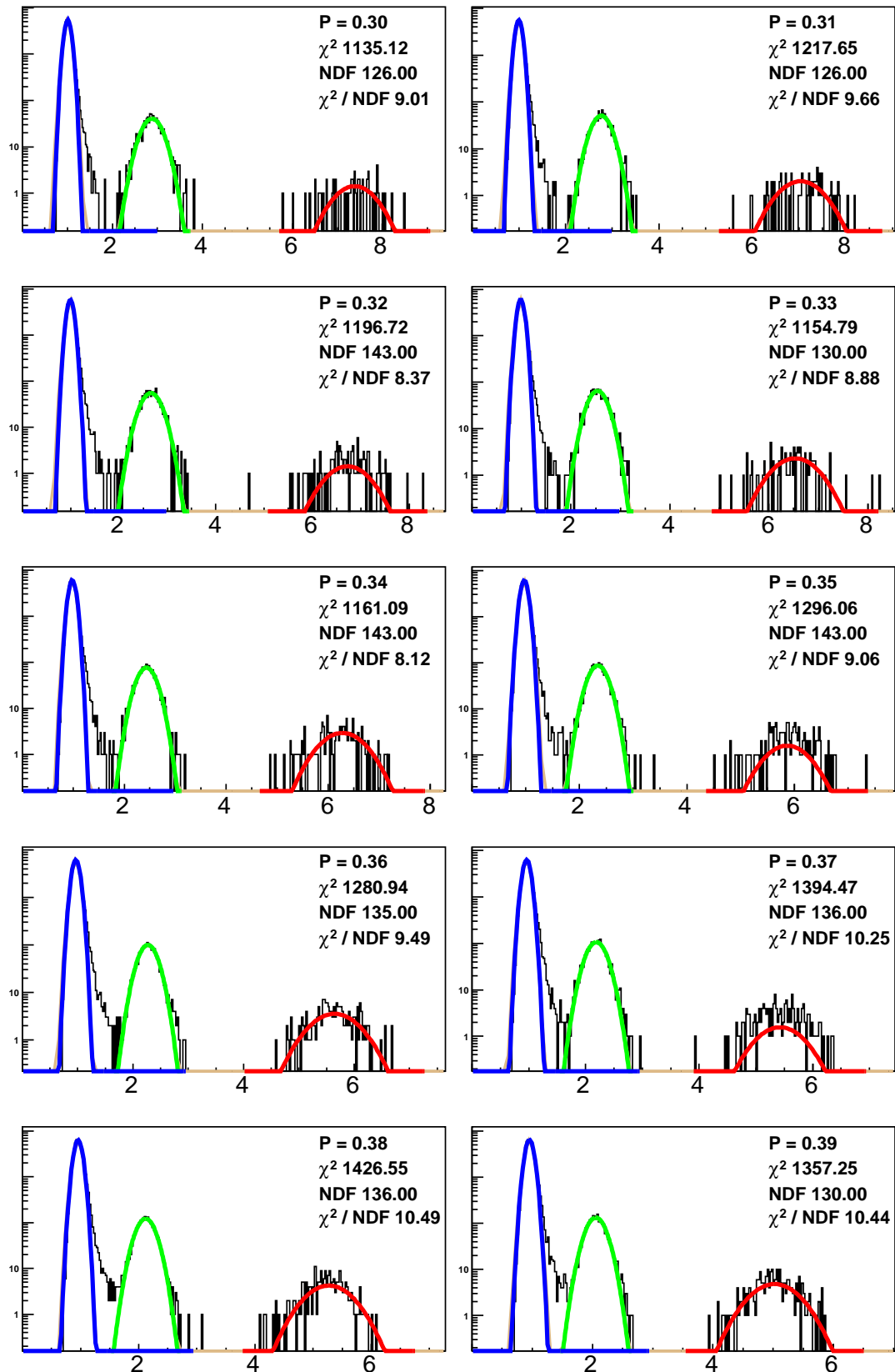


Figure 78.

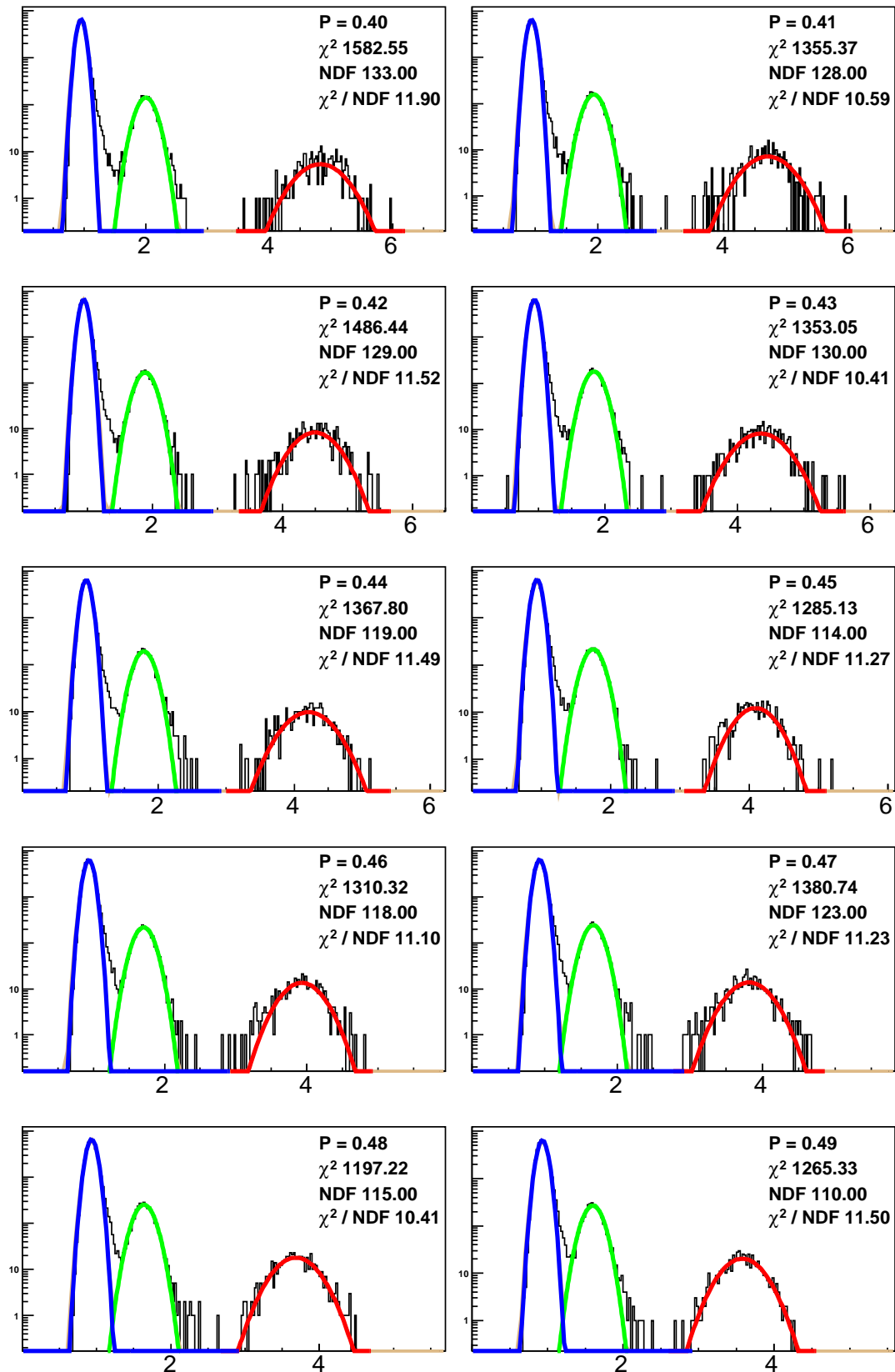


Figure 79.

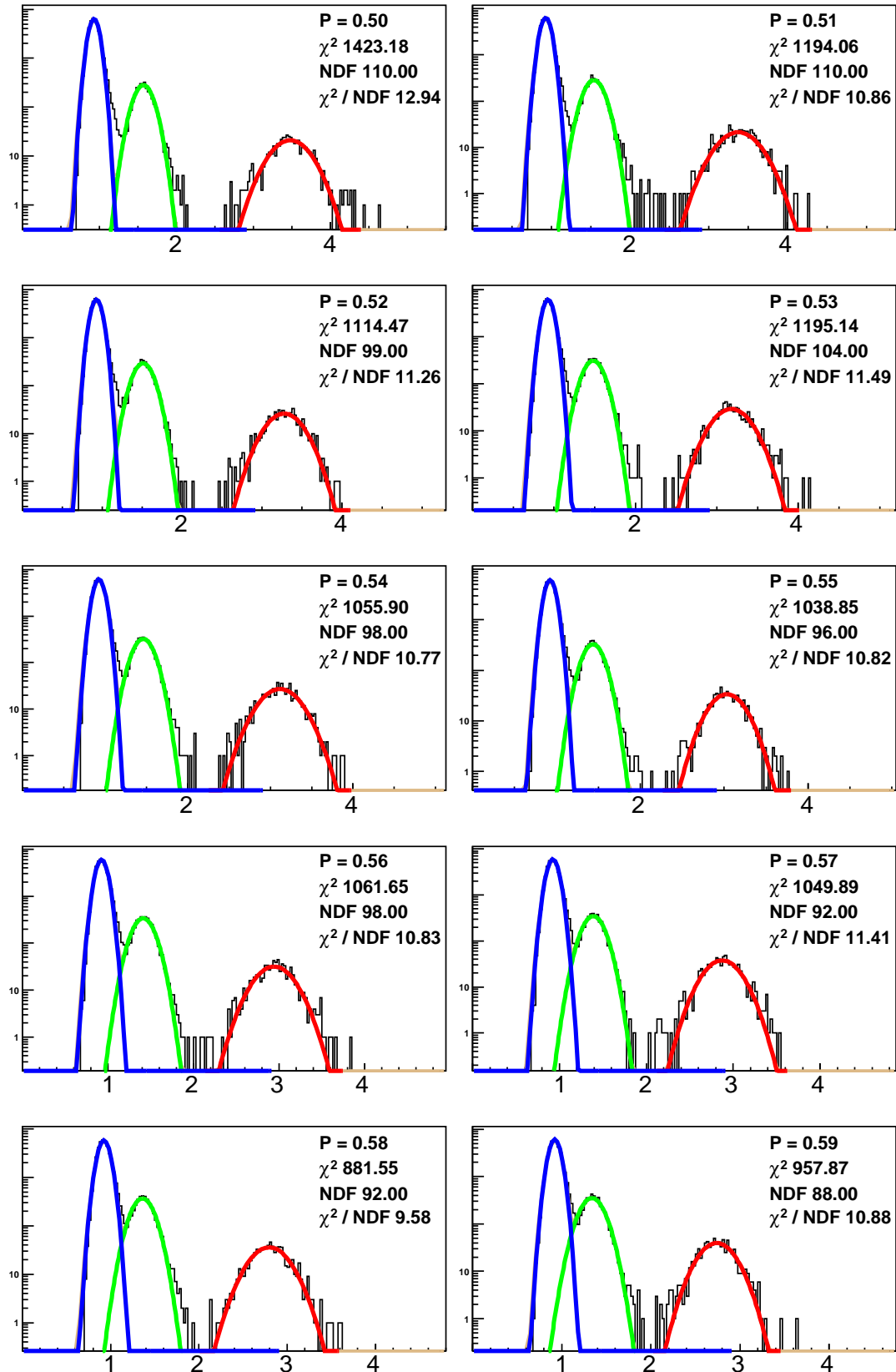


Figure 80.

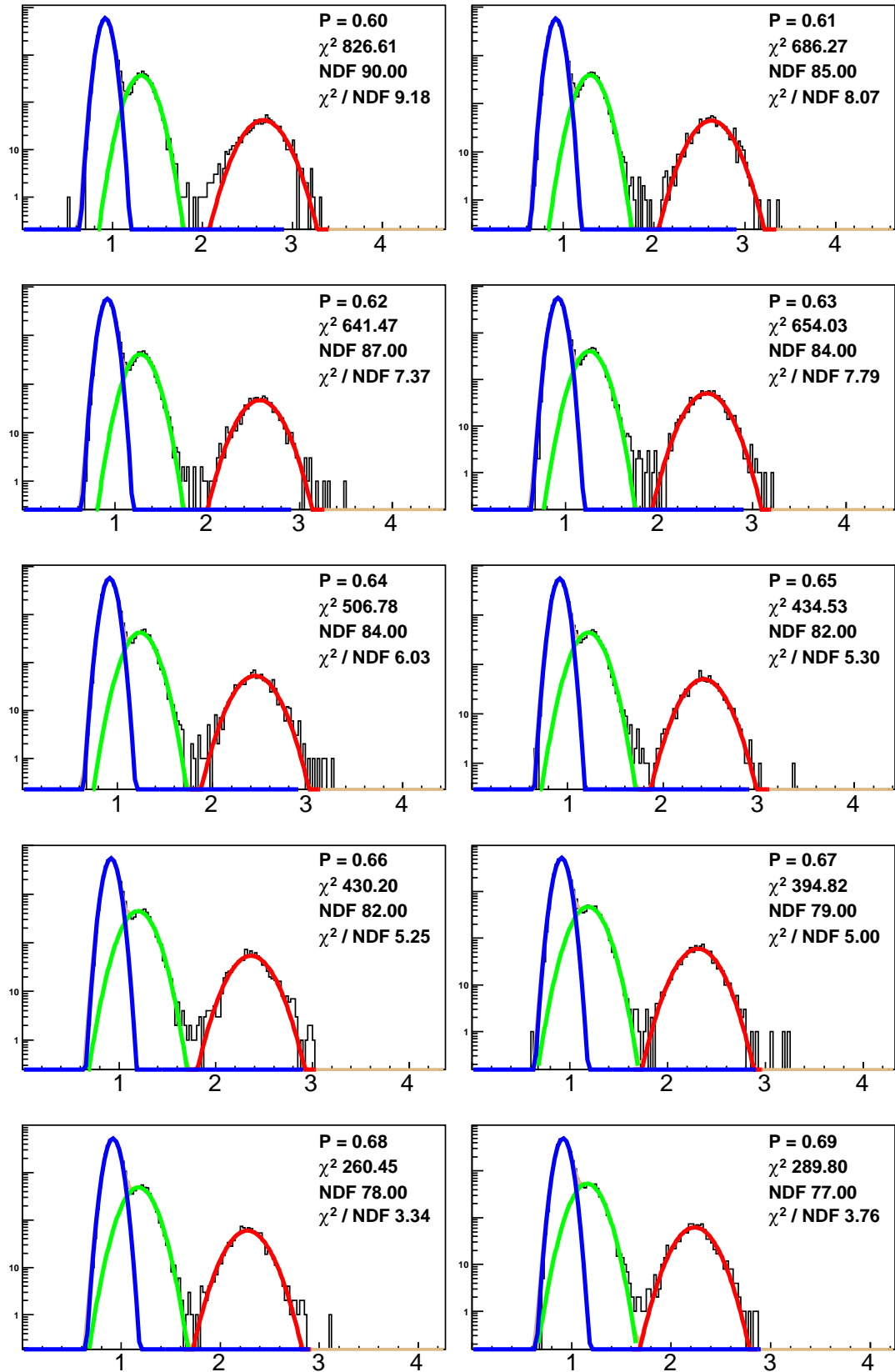


Figure 81.

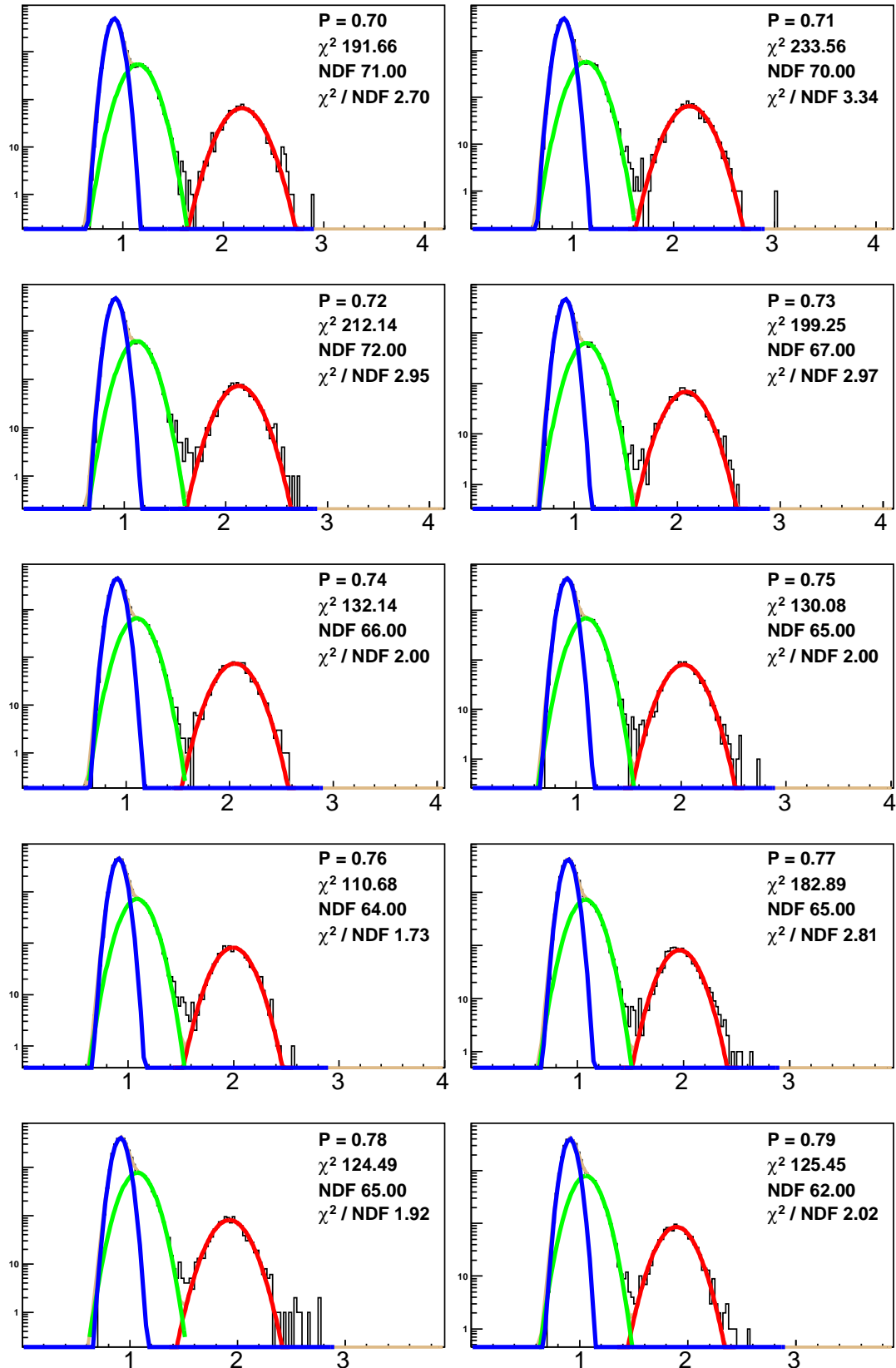


Figure 82.

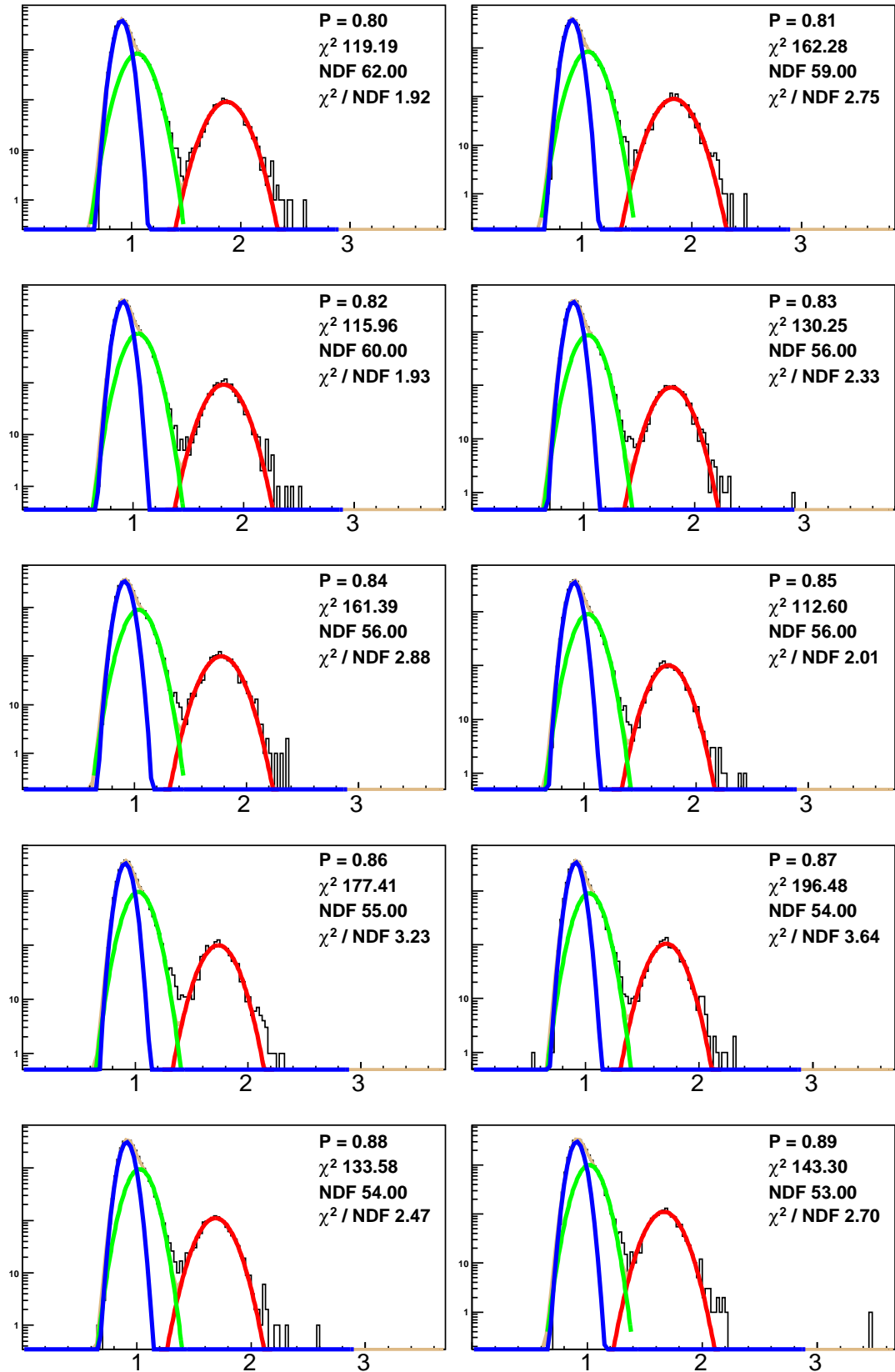


Figure 83.

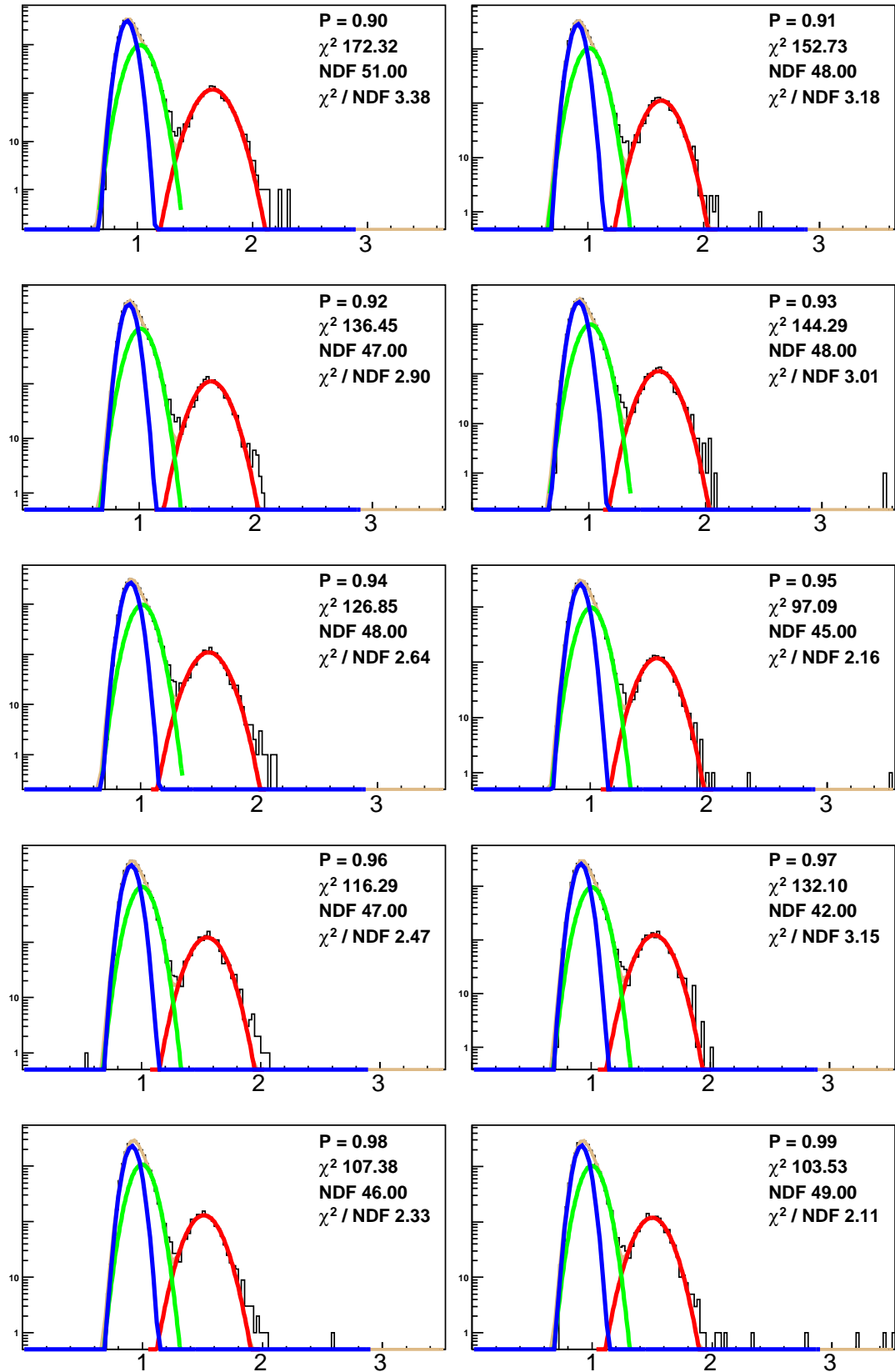


Figure 84.

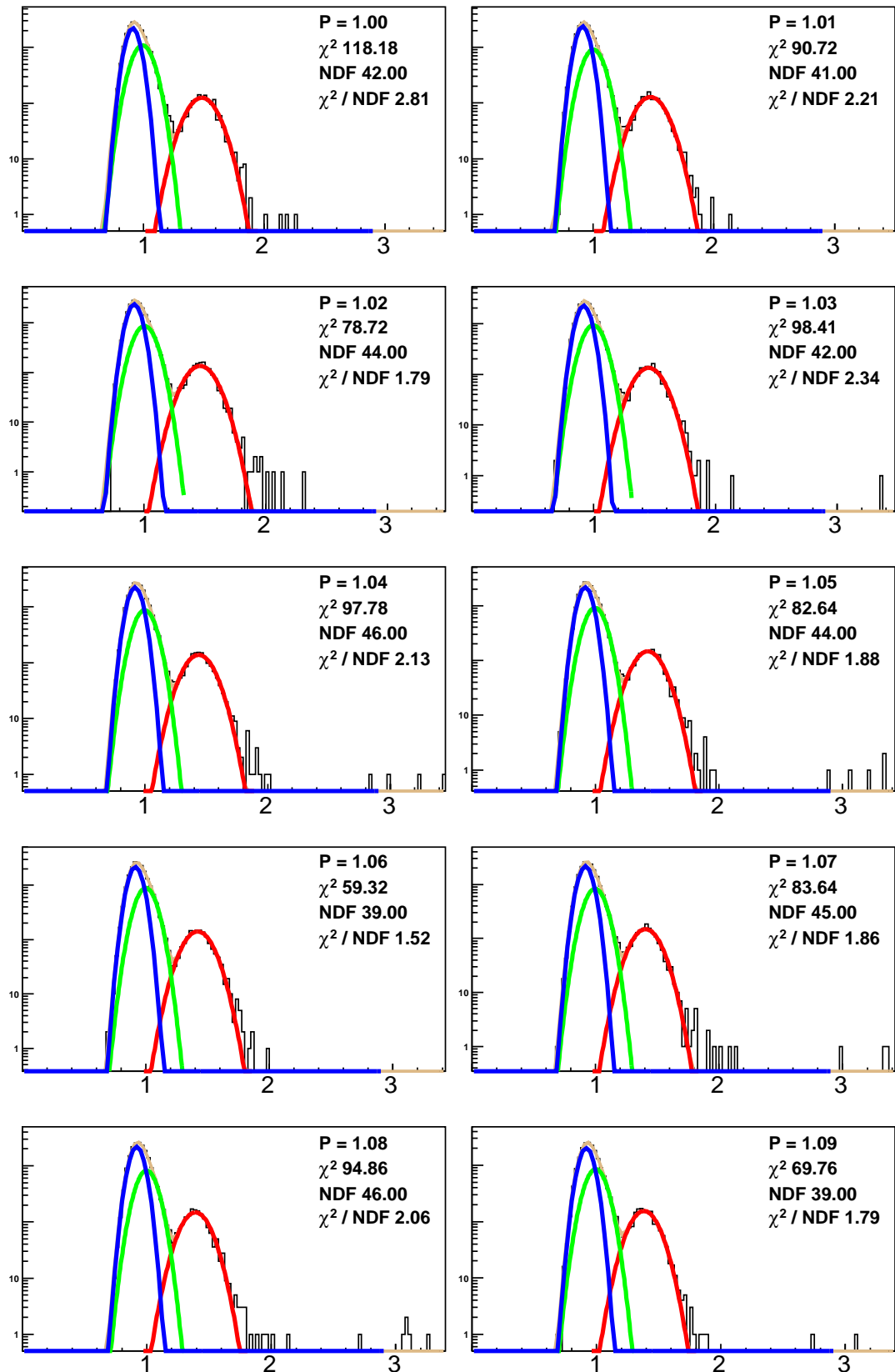


Figure 85.



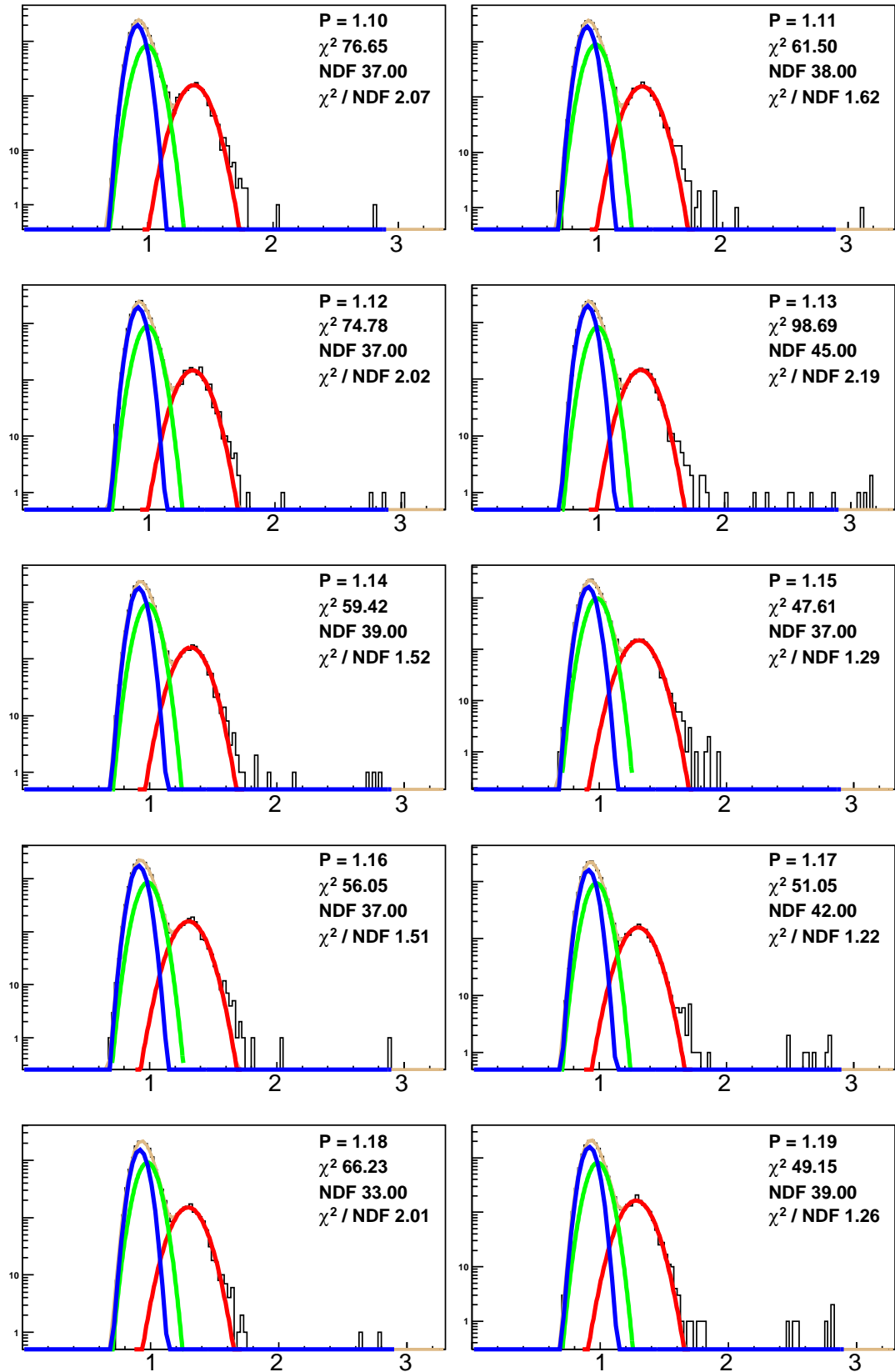


Figure 86.

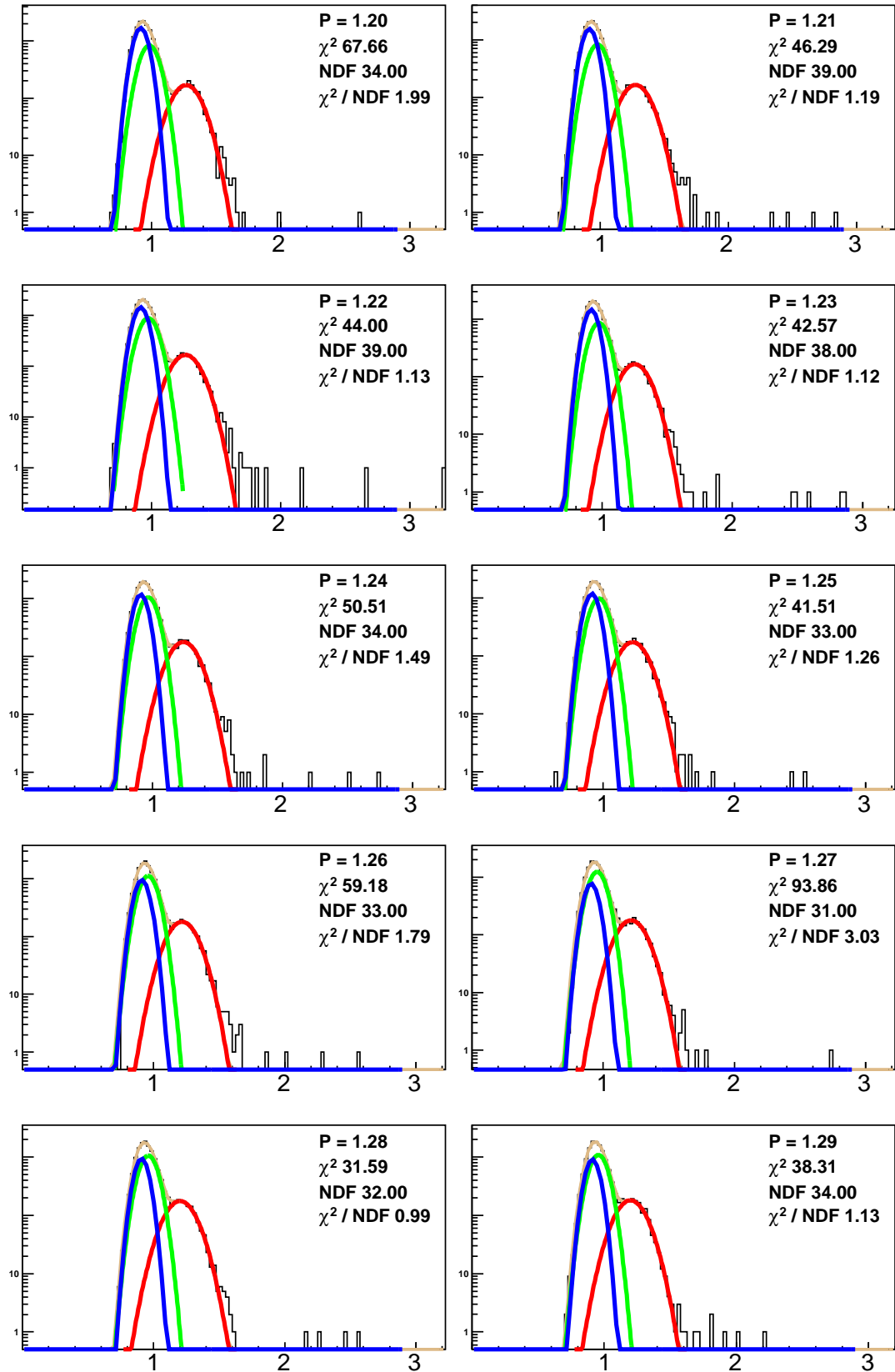


Figure 87.

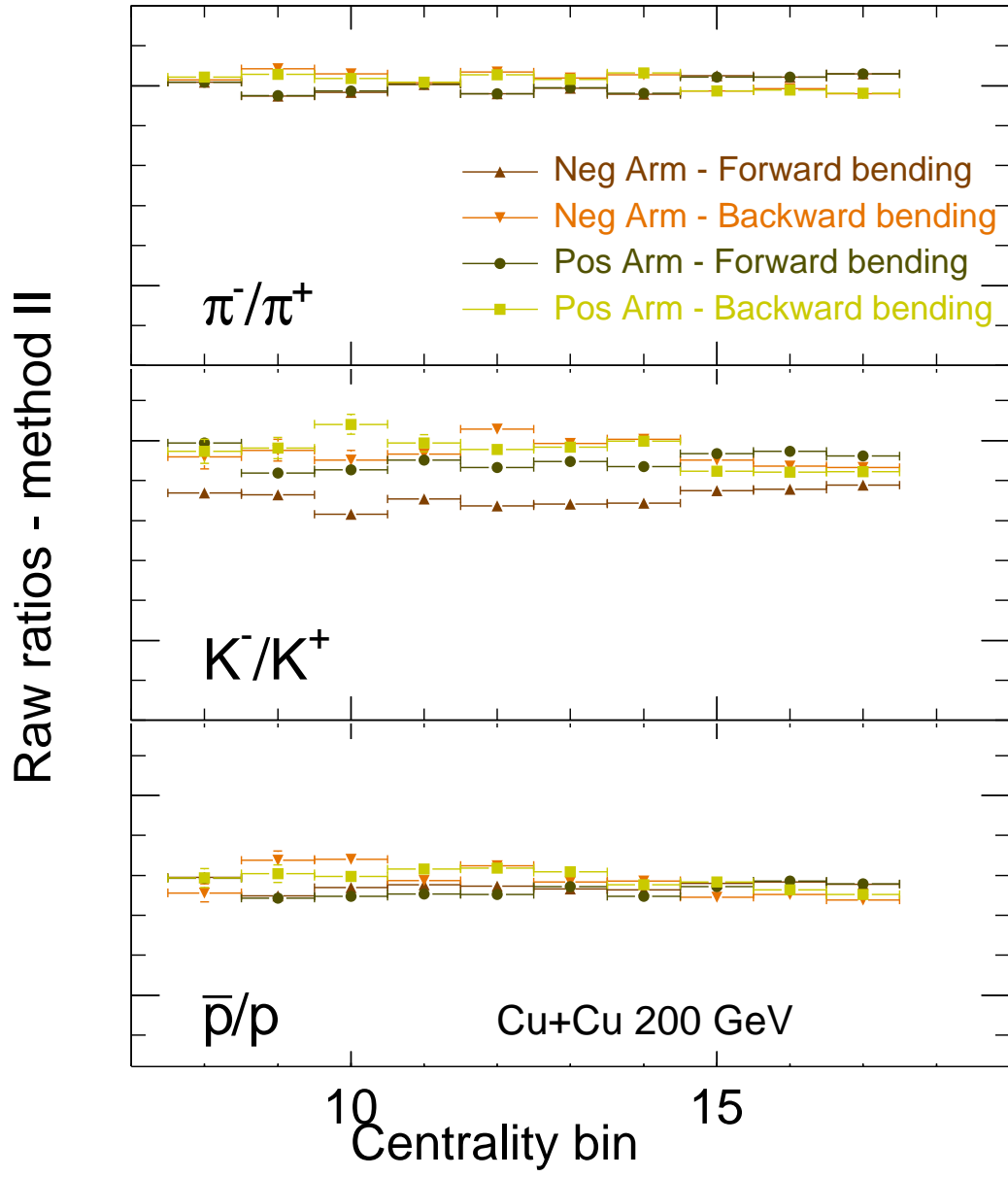


Figure 88.

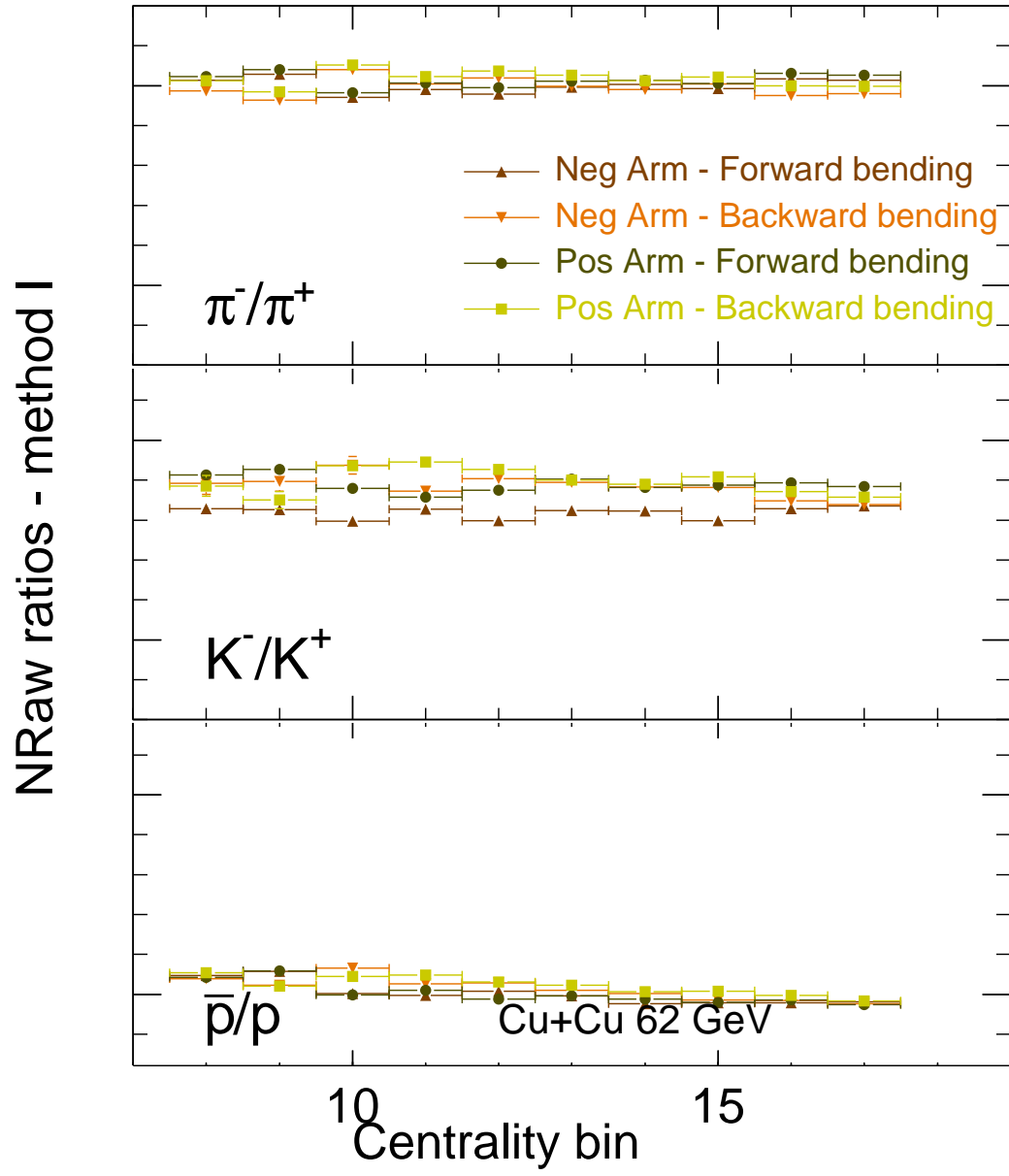


Figure 89.

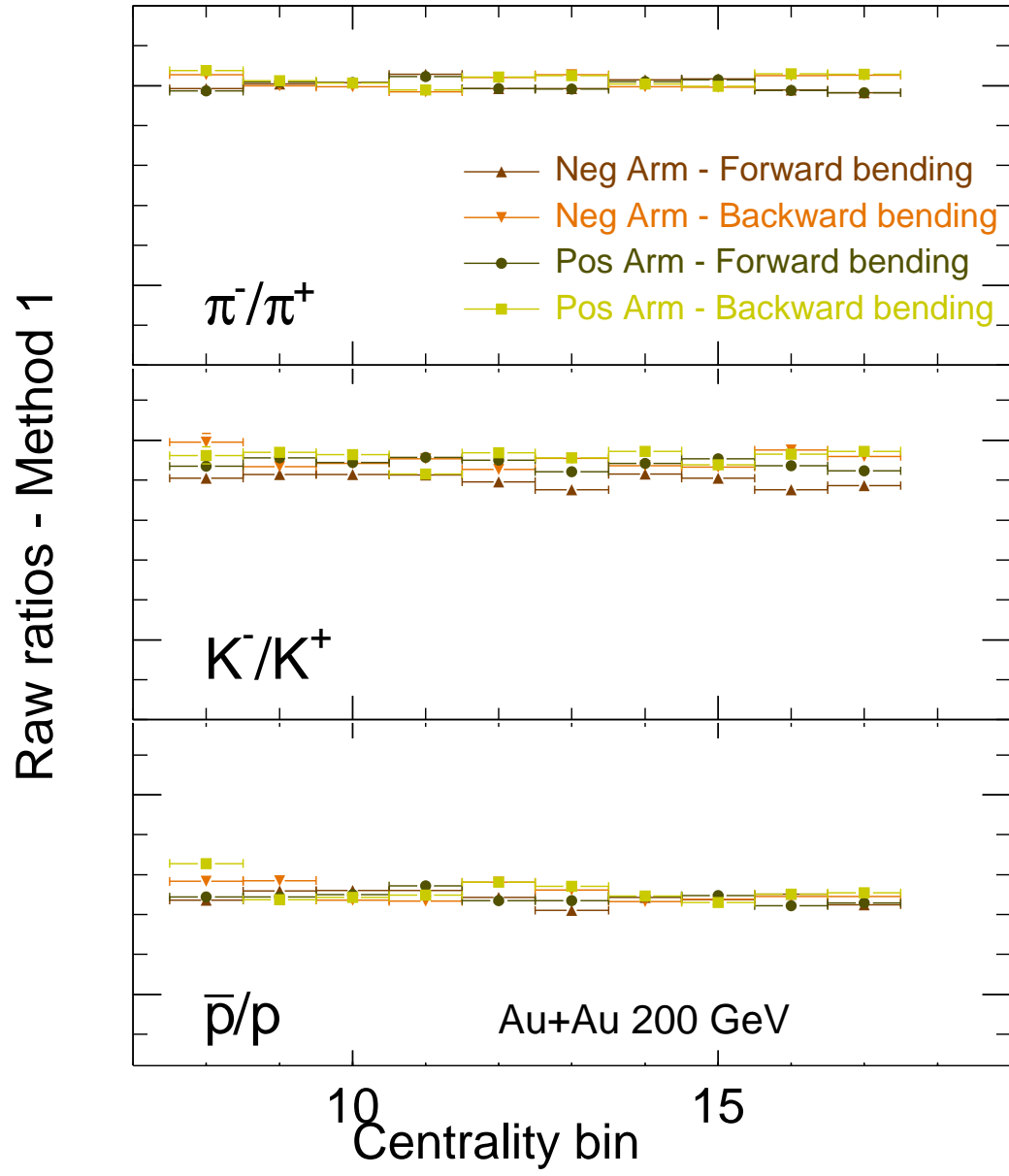


Figure 90.

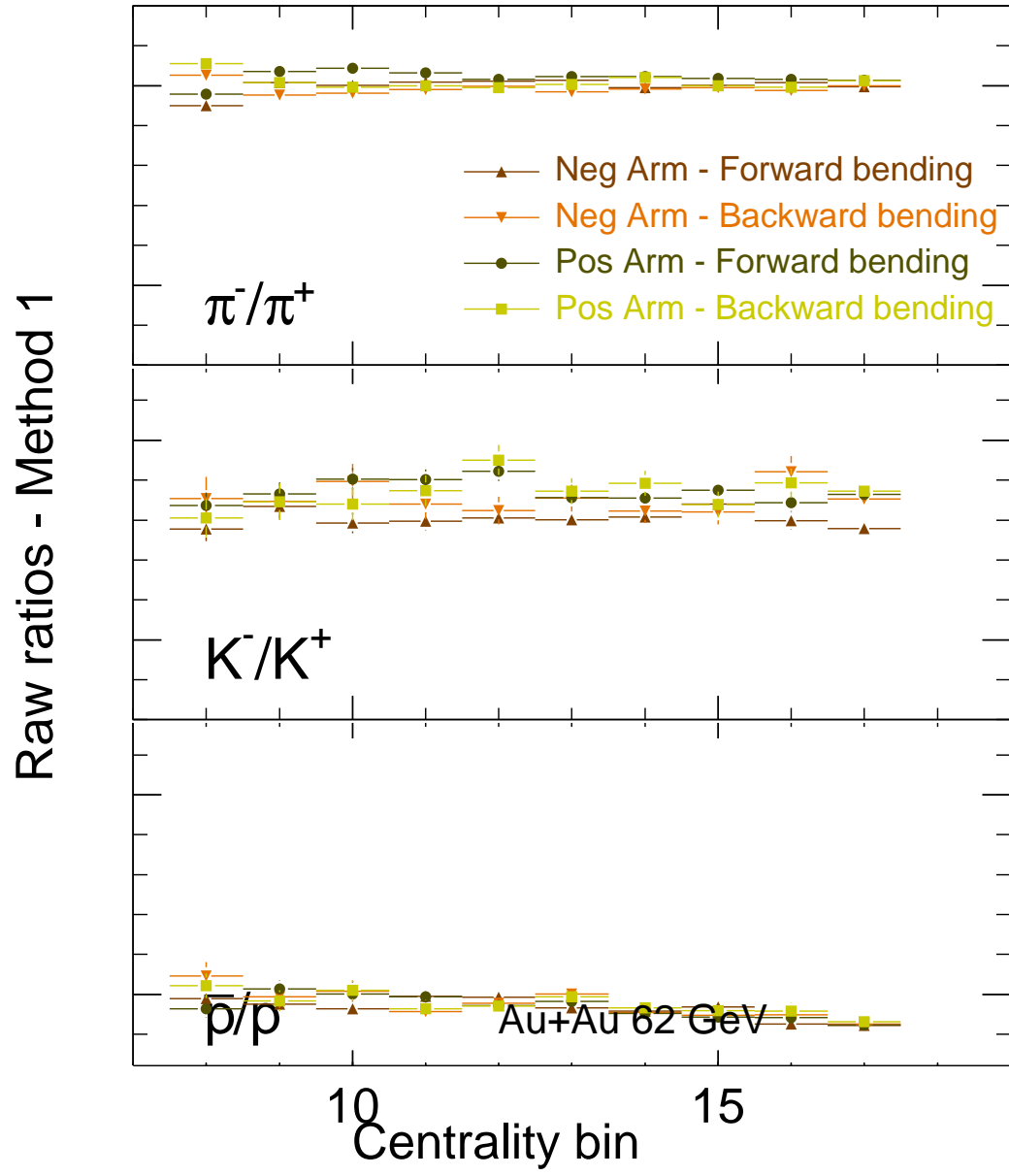


Figure 91.

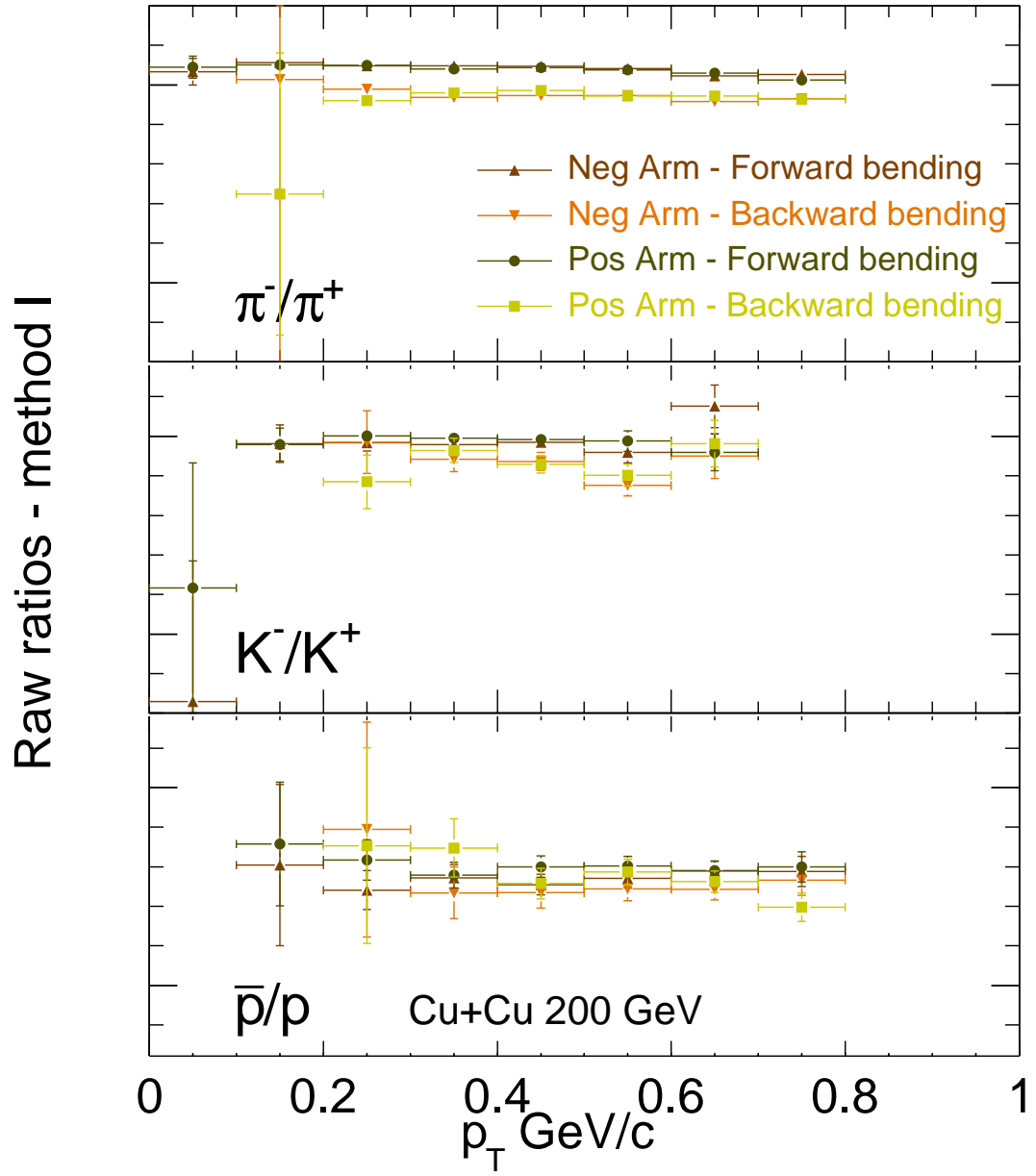


Figure 92.

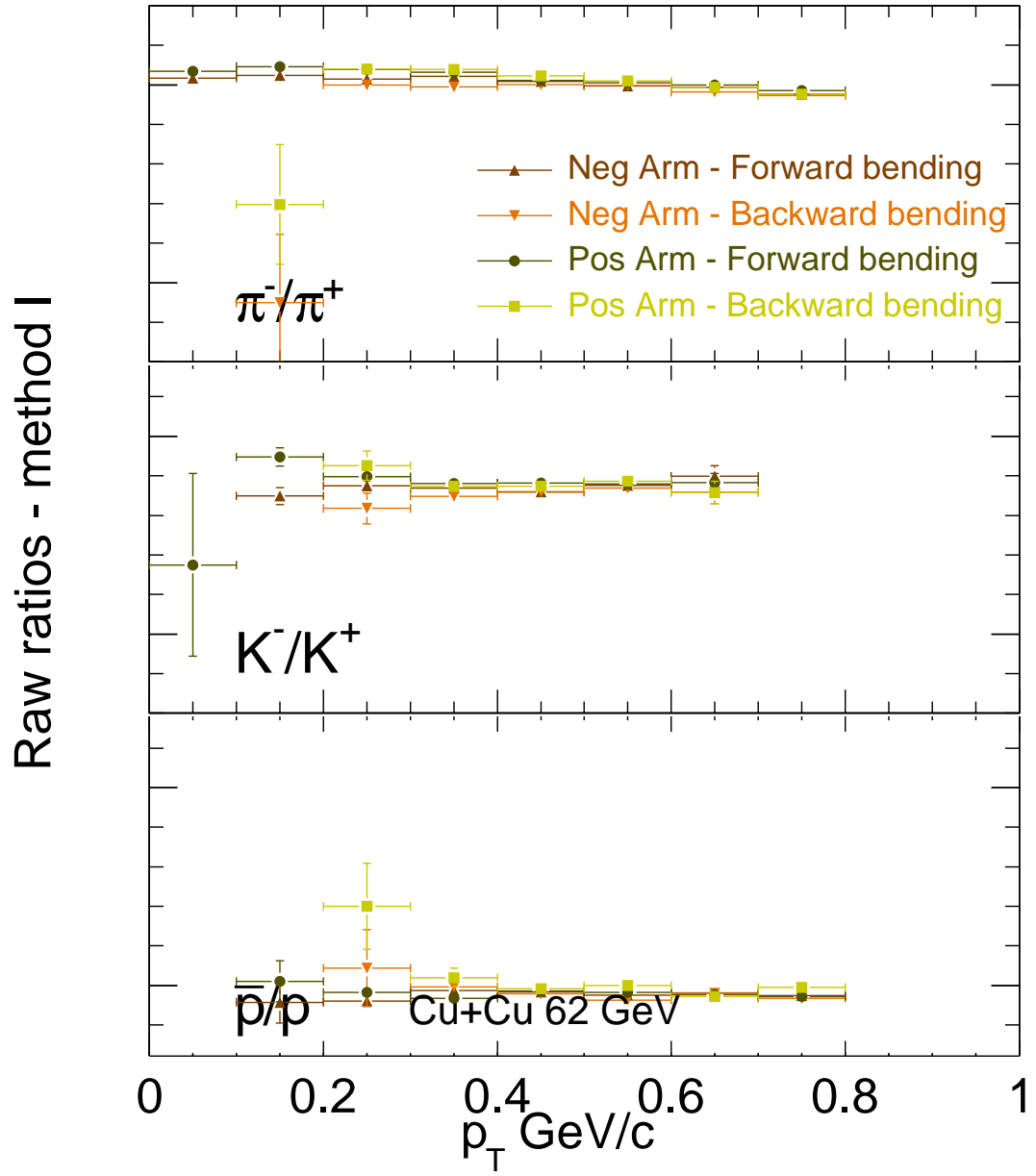


Figure 93.



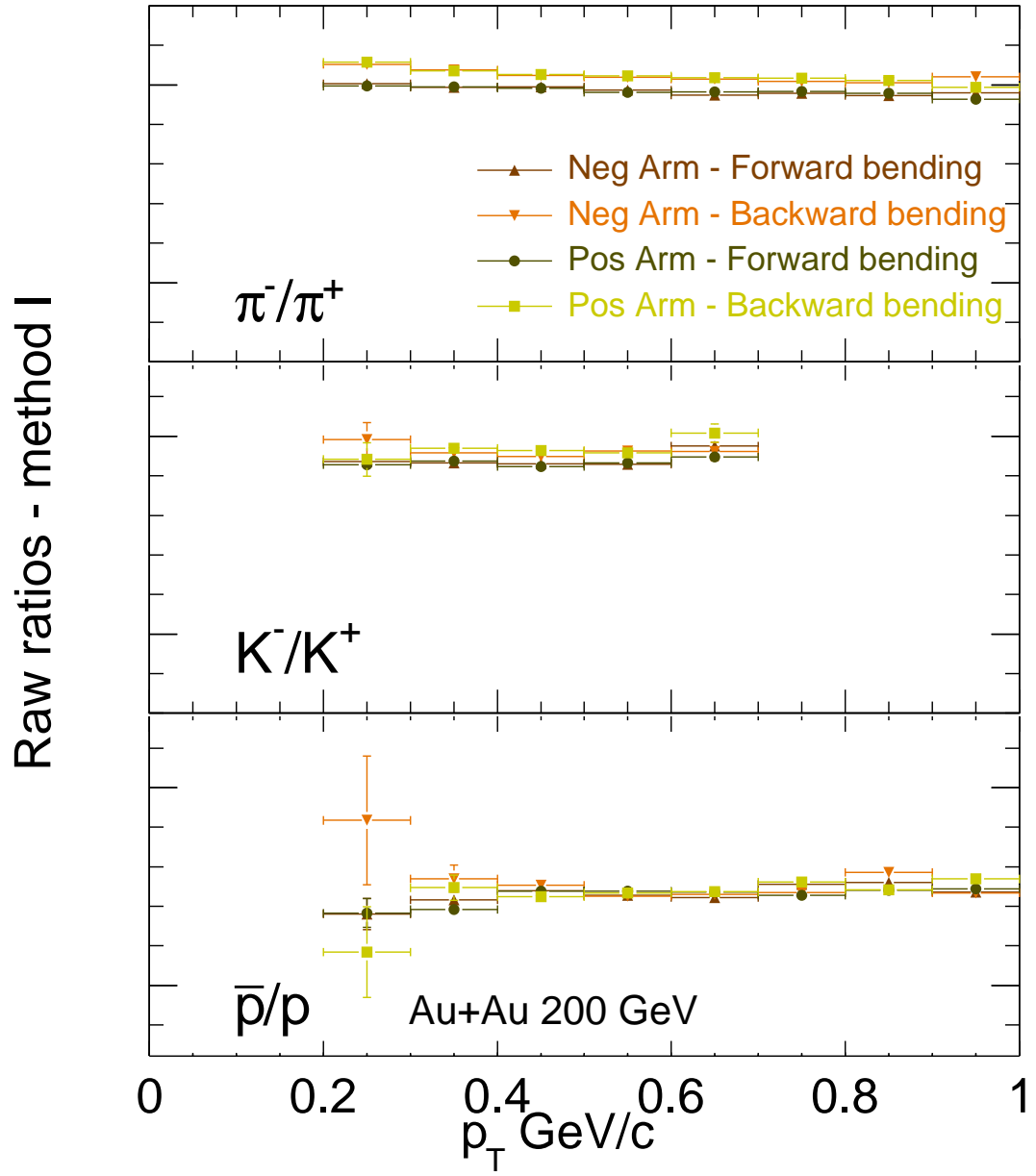


Figure 94.

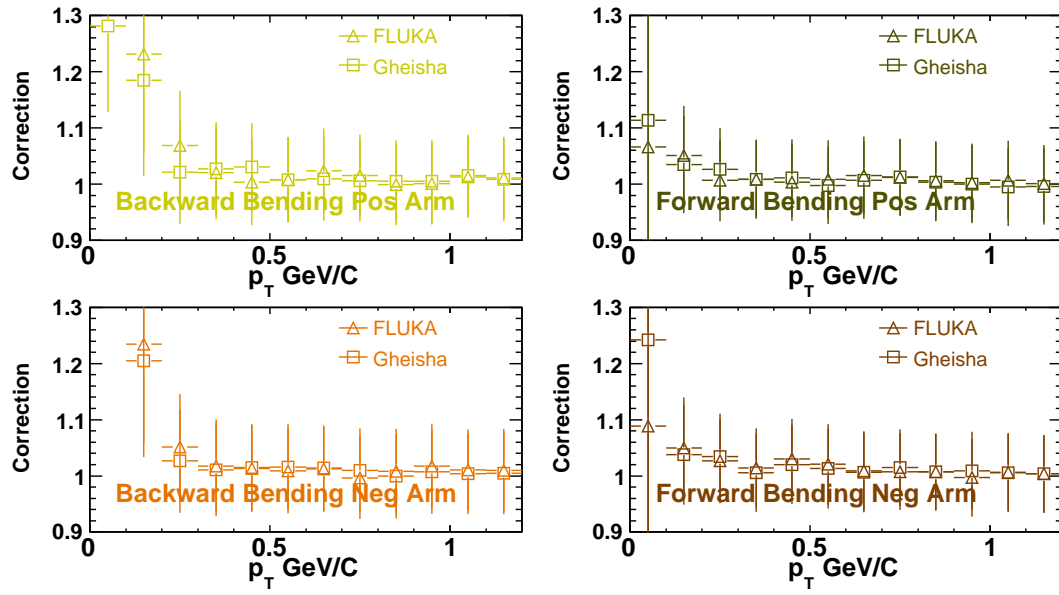


Figure 95.

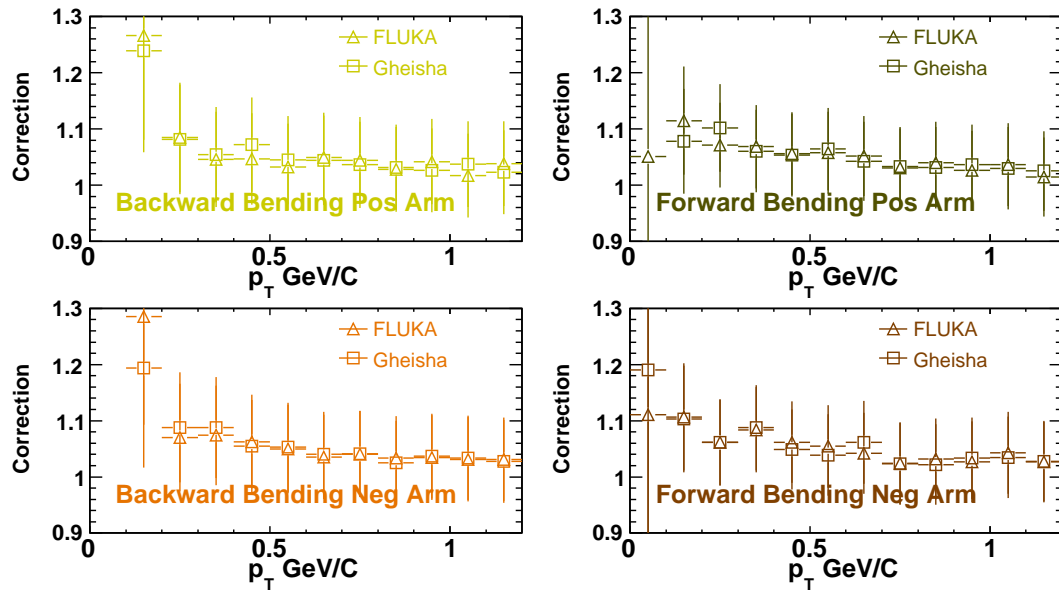


Figure 96.

## CHAPTER 14

### SYSTEMATIC ERROR STUDY - ADDITIONAL PLOTS

## CITED LITERATURE

1. P. Braun-Munzinger, J. Stachel, J. P. W. and Xu, N.: Thermal equilibration and expansion in nucleus-nucleus collisions at the ags. Phys. Lett. B, 344:43, 1995.
2. P. Braun-Munzinger, J. Stachel, J. P. W. and Xu, N.: Thermal and hadrochemical equilibration in nucleus-nucleus collisions at the sps. Phys. Lett. B, 365:1, 1996.
3. Cleymans, J. and Redlich, K.: Chemical and thermal freeze-out parameters from 1 to 200 a.gev. Phys. Rev. C, 60:054908, 1999.
4. Becattini, F., Cleymans, J., Keranen, A., Suhonen, E., and Redlich, K.: Features of particle multiplicities and strangeness production in central heavy ion collisions between 1.7-a- gev/c and 158-a-gev/c, 2001.
5. Becattini, F. and Passaleva, G.: Statistical hadronisation model and transverse momentum spectra of hadrons in high energy collisions. Eur. Phys. J. C, 23:551, 2002.
6. Harrison, M. and et al: Rhic project overview. Nucl. Instrum. Meth., A 499:235–244, 2003.
7. Hahn, H. and et al: The rhic design overview. Nucl. Instrum. Meth., A 499:245–263, 2003.
8. Thieberger, P. and et al: Tests for pulsed high current heavy ion synchrotron injection with an mp-tandem van de graaff. EEE Trans. Nucl. Sci. NS-30., 30:2746–2748, 1983.
9. Zarcone, M. and et al: Further development with heavy ion sources at brookhaven nationallaboratory; tandem van de graaff facility. Instr. and Meth., 4:3178–3180, 1993.
10. Adamczyk, M. and et al: The brahms experiment at rhic. Nucl. Instrum. Meth., A 499:437–468, 2003.
11. Arsene, I. and et al: Quark-gluon plasma and color glass condensate at rhic? the perspective from the brahms experiment. Nucl. Phys., A 757:1–27, 2005.
12. Ackermann, K. and et al: Star detector overview. Nucl. Instrum. Meth., A 499:624–632, 2003.
13. Adams, J. and et al: Experimental and theoretical challenges in the search for the quark-gluon plasma: The star collaboration’s critical assessment of the evidence from rhic collisions. Nucl. Phys., A 757:102–183, 2005.
14. Adcox, K. and et al: Phenix detector overview. Nucl. Instrum. Meth., A 499:469–479, 2003.

15. Adcox, K. and et al: Formation of dense partonic matter in relativistic nucleus-nucleus collisions at rhic: Experimental evaluation by the phenix collaboration. Nucl. Phys., A 757:184–283, 2005.
16. Back, B. and et al: The phobos detector at rhic. Nucl. Instrum. Meth., A 499:603–623, 2003.
17. Back, B. and et al: The phobos perspective on discoveries at rhic. Nucl. Phys., A 757:28–101, 2005.
18. Decowski, M. P.: Energy and Centrality Dependence of Mid-Rapidity Charged Particle Multiplicity in Relativistic Heavy-Ion Collisions. Doctoral dissertation, Massachusetts Institute of Technology, 2001.
19. Leo, W. R.: Techniques for Nuclear and Particle Physics Experiments, chapter 2, pages 21–50. Springer-Verlag, 1987.
20. Jackson: Electrodynamics, chapter 2, pages 21–50. Springer-Verlag, 1987.
21. Amsler, C. and et al: Review of particle physics. Physics Letters B., 667:1, 2008.
22. Fesefeldt, H. C.: The simulation of hadronic showers: Physics and applications. Technical report, 1985. PITHA-85-02.
23. Aarnio, P. A.: Fluka user’s guide, 1987. TIS-RP-190.
24. Zimányi, J.: Quark coalescence, 1999.
25. Ahle, L. et al.: An excitation function of  $k^-$  and  $k^+$  production in  $au + au$  reactions at the ags, 2000.
26. Ahle, L. et al.: Proton and deuteron production in  $au + au$  reactions at 11.6/a-gev/c, 1999.
27. Ahle, L. et al.: Antiproton production in  $au + au$  collisions at 11.7-a- gev/c, 1998.
28. Bearden, I. G. et al.: Mid-rapidity protons in 158-a-gev pb + pb collisions, 1996.
29. Bachler, J. et al.: Hadron production in nuclear collisions from the na49 experiment at 158-gev/c/a, 1999.
30. et al., B. I. A.: , , 2007.
31. et al., I. G. B.: , , 2005.
32. et al., B. B. B.: , , 2005.

33. et al., S. S. A.: , , 2004.
34. van Buren et al., G.: , , 2003.
35. et al., I. G. B.: , , 2005.
36. et al., B. B. B.: , , 2003.
37. Stachel, J. and Braun-Munzinger, P.: Thermal equilibration and expansion in nucleus-nucleus collisions at the ags. Phys. Lett. B, 216:1, 1989.
38. Gibbard, B. and et al: The rhic computing facility. Nucl. Instrum. Meth., A 499:814–818, 2003.
39. Baym, G. and et al: Report of task force for relativistic heavy ion physics. Nucl. Phys., A 418:657–668, 1983.
40. R., B. and et al: Array of scintillator counters for phobos at rhic. Nucl. Instrum. Meth., A 474:38–45, 2001.
41. Adler, C. and et al: The rhic zero-degree calorimeters. Nucl. Instrum. Meth., A 499:433–436, 2003.
42. Back, B. and et al: Charged-particle pseudorapidity density distributions from au+au collisions at  $\sqrt{s_{NN}}=130$  gev. Phys. Rev. Lett., 87:102303, 2001.
43. Gulbrandsen, K. H.: Relative Yields of Antiparticles to Particles in Au+Au Collisions at 130 and 200 GeV per Nucleon Pair. Doctoral dissertation, Massachusetts Institute of Technology, 2004.
44. Bickley, A.: Charged Antiparticle to Particle Ratios Near Midrapidity in d+Au and p+p Collisions at  $\sqrt{s_{NN}} = 200$  GeV. Doctoral dissertation, University of Maryland, 2004.
45. EdwardWenger: Studies of High TransverseMomentum Phenomena in Heavy Ion Collisions Using the PHOBOS Detector. Doctoral dissertation, Massachusetts Institute of Technology, 2008.
46. Brun, R. et al.: Geant detector description and simulation tool. Technical report, 1994. CERN Program Library, W5013. The GEANT manual can be found at [http://wwwasdoc.web.cern.ch/wwwasdoc/geant\\_html3/geantall.html](http://wwwasdoc.web.cern.ch/wwwasdoc/geant_html3/geantall.html).
47. et al., C. A.: , , 2001.
48. et al., B. B. B.: , , 2007.
49. Ioradanova, A.: Particle production at rhic.

## VITA

This is where the vita goes. Its organization is left as an exercise.